Reliability Prediction of Single Crystal Silicon MEMS using Dynamic Raman Spectroscopy

A thesis submitted to the Faculty of Science, Agriculture and Engineering for the Degree of Doctor of Philosophy

by
Raden Sanggar Dewanto

School of Mechanical and Systems Engineering
Newcastle University

June 2014

Abstract

The work investigates an extension and improvement to reliability prediction in single crystal silicon MEMS by utilising dynamic Raman spectroscopy to allow fracture test data collected directly from devices thereby taking account of actual geometrical tolerances, dynamic load conditions and effects from the microfabrication process.

Micro-cantilever beam MEMS devices microfabricated from (100) crystalline silicon wafers having [110] beam direction were used in this experiment. A piezo actuator was used to vibrate the devices. The fracture data was taken by increasing the supply voltage to bring each device to rupture whilst a continuous beam HeNe laser was directed from the [100] direction to particular positions on the sample allowing for capture of the LO_z photons. The resulting Raman profile, broadened by the vibration of the device, was fit using a Voigt profile and compared to the no load condition. A calibration step was used to convert the Raman signal to volumetric μstrain.

The reliability prediction methodology used in this work was developed under the Weibull distribution function that is based on the concept of weakest link theory describing distribution of flaws in brittle material. As each device was fabricated from semiconductor grade single crystalline silicon, it can be considered to have no mechanical defects with the flaws on the device only existing as surface flaws induced from the microfabrication process during manufacturing. Differently processed surfaces each have their own Weibull parameters. The failure prediction of a particular MEMS device is calculated from these parameters with the simulated structure responses due to applied load being predicted from the finite element package ANSYS.

The failure prediction method shows a good agreement with the experimental results with accuracy of 10%. However, visual observations were necessary as a number of ruptured specimens started to fail from the bottom side of the clamped end and propagated through [111] direction so from the upper side the failure looks like it started from a distance from the clamped end.

The experimental work was carried out utilising [100] Raman scattering. This limits the ability of the system to only capture the strain condition in one direction; the other strain directions were approximated using silicon orthotropic material properties and assuming that the load is a uniaxial load. This limitation forces the failure prediction distribution function to treat silicon as an isotropic material with the strength

characteristic scale parameter in the Weibull distribution being the same value for all directions. This limitation together with extending the work towards implementing an “off-axis” Raman characterisation able to characterise all the strain directions is discussed for future work.

Acknowledgement

Firstly I would like to thanks my supervisors Dr John Hedley, Dr Barry Gallacher and Dr Zhongxu Hu for their continued help and support throughout my Ph.D. Particular thanks go to Dr Hedley for the advice, guidance given on a daily basis and great patience at all times. I wish to thanks Dr Carl Dale for his help in the laboratory and I would extend thanks to all the staff in the mechanical workshops for their assistance. Thank you also to Dr Ali Daraji for providing me 'around the clock' discussion about the Finite Element. I would like to extend a general thank you to all of my colleagues within the School of Mechanics and Systems Engineering and Medical School, as I have found everyone to be extremely helpful. Finally thank you to my wife, my daughter and all my family for supporting me throughout this Ph.D.

Contents

Chapter 1. Introduction **1**

1.1. Background 1

1.2. Motivation 2

1.3. Aims and objectives 2

1.4. Reliability prediction of MEMS device 3

1.4.1. Weibull weakest link theory 4

1.4.2. Flaw population due to micfabrication processes 4

1.4.3. Surface roughness and fracture strength relation 5

1.4.4. The size effect 5

1.4.5. Characteristic area variation due to different mode shape of vibration 6

1.4.6. Fracture surface 6

1.5. Raman spectroscopy 6

1.5.1. Basic physics of Raman Spectroscopy 7

1.5.2. Micro Raman spectroscopy 8

1.5.3. Strain-dependent Raman spectrum on single crystal silicon 9

1.5.4. Dynamic micro-Raman spectroscopy 10

1.6. Previous work 10

1.6.1. Reliability study of silicon MEMS devices under brittle fracture 10

1.6.2. Optical Techniques in MEMS Characterisation 12

1.6.3. Raman spectroscopy 12

1.7. Thesis overview 13

Chapter 2. Reliability Prediction **15**

2.1. Introduction 15

2.2. Assumption 15

2.3. Single crystal silicon properties 16

2.3.1. Anisotropic elasticity 17

2.4. Fracture probability 20

2.4.1. Review of Weibull Weakest Link Failure Theory 20

2.4.2. Differential probability of failure of a non-uniform stress distribution device 23

2.4.3. Dynamic model of the structure 25

2.4.4. Volumetric probability of failure of the structure: model 28

2.4.5. Surface area probability of failure of the structure: model 29

2.4.6. Location probability of failure of the structure: model 30

2.5. Weibull Parameters Determination 33

Chapter 3. Equipment and fabrication 35

3.1. Devices fabrication 35

3.1.1. Material consideration: Silicon wafers 35

3.1.2. Microfabrication processes 36

3.1.3. Microfabricated devices 39

3.1.4. Mechanically cut silicon beams 42

3.2. Equipment and characterisation procedure 42

3.2.1. Four point bending 42

3.2.2. Vacuum chamber 43

3.2.3. Piezo-actuator and die mounting 44

3.2.4. Surface profiler 45

3.2.5. Laser Vibrometer 48

3.2.6. Visual observation 51

3.2.7. Raman spectroscopy 52

3.2.8. Scanning Electron Microscopy imaging 54

Chapter 4. Raman Spectroscopy 56

4.1. Introduction 56

4.2. Raman Spectra 57

4.2.1. Raman Spectra of Single Crystalline Silicon *57*

4.2.2. Voigt fitting for Raman spectra fitting *58*

4.2.3. Data density and spectral resolution *60*

4.3. Peak position calibration 61

4.4. Raman shift and stress relation calibration 62

4.4.1. Raman-strain dependency *63*

4.4.2. Four point-bending *65*

4.4.3. Raman Shift due to Applied Load *67*

4.4.4. Off-axis Raman spectroscopy *69*

4.5. Dynamic Raman Characterisation 70

4.5.1. Modulated Raman Spectroscopy *70*

4.5.2. Raman Profile Broadening *71*

4.5.3. Comparison based on beam deflection *72*

4.5.4. Concentration factor, spot size and penetration depth of the laser beam *74*

Chapter 5. Weibull parameters determination 76

5.1. Data type 76

5.1.1. Experiment procedure *76*

5.2. Failure modes and surface roughness consideration 77

5.3. Resonance frequencies 78

5.3.1. ANSYS resonance frequencies computation *78*

5.3.2. Outlying observation due to unusual resonance frequency *79*

5.4. Weibull fit of fracture data 79

5.4.1. Mechanically polished surface *81*

5.4.2. DRIE surface *83*

Chapter 6. Failure Prediction and method validation 88

6.1. Device model 88

6.2. Failure model 89

6.2.1. Failure prediction procedure using ANSYS 90

6.2.2. Failure Predictions of the Structures 91

6.3. Validation of the prediction method 93

6.3.1. Approach 94

6.3.2. Fracture strength 94

6.3.3. Rupture position 97

Chapter 7. Discussion of Results 101

7.1. The usefulness of the method 101

7.1.1. The failure predictions related to the size 101

7.1.2. The failure predictions due to surface type 103

7.1.3. Data scatter prediction due to surface type 104

7.1.4. Failure location distribution 104

7.1.5. Analysis of prediction and test results discrepancy 105

7.2. Contributing errors 106

7.2.1. Assumptions and mathematical models 106

7.2.2. Measurement methods and equipment 107

Chapter 8. Conclusion 108

8.1. Conclusion of the work 108

8.2. Future Work 108

Nomenclature

K_{IC}	Fracture toughness
λ	Wavelength
υ	Frequency
ω	Wavenumber
h	Planck constant
E	Energy
c	Speed of light
ω_I	Wavenumber of incident radiation
ω_M	Wavenumber of vibration level
ω_0	Wavenumber of scattered radiation (unstrained)
ω_i	Strained wavenumber
λ_i	Eigenvalues of Raman characteristic equation
σ	Stress
ε	Strain
C	Stiffness
S	Compliance
f	Failure probability
δf	Infinitesimal failure probability
$\psi(\sigma)$	Failure function with respect to internal stress
V	Volume

V_0	Characteristic volume
δV	Infinitesimal volume
r	Probability to withstand (or alternatively, the reliability)
δr	Infinitesimal probability to withstand
σ_θ	Weibull characteristic strength – specimen geometry dependent
σ_0	Weibull characteristic strength – material specific
m	Weibull modulus
E	Young's modulus
κ	Curvature
y_0	Distance to neutral axis
H	Height/depth of beam
w	Width of beam
L	Length of beam
ϑ	Deflection
ϑ_L	Maximum deflection at the free end of cantilever
λ_s	Scaling factor
X	Mode shape
$\sigma_{xx}(x,y)$	Axial stress distribution over the beam
σ_m	Maximum stress
ψ_U	Failure function of upper/lower beam surface (polished)
ψ_S	Failure function of side beam surface (DRIE process)

A_U	Area of upper/lower beam surface (polished)
A_S	Area of side beam surface (DRIE process)
q	Probability of failure location density
s	Sag
d	Diameter
$\tilde{x}$	Displacement amplitude
V_R	Velocity range
f_d	Driving frequency
I	Relative intensity
p_I	Polarisation vector of incident radiation
p_S	Polarisation vector of scattered radiation
R_i	Polarisability tensor
f_V	Voigt profile
f_L	Lorentzian profile
f_G	Gaussian profile
α_L	Half-width of the Lorentzian profile
α_G	Half-width of the Gaussian profile
p_D, q_D, r_D	3 dimensional phonon deformation potentials
ρ	Radius of curvature
ρ_s	Radius of curvature of sample surface
R_0	Raman profile in static condition

R_B	Broadened Raman profile
$f_V(u_0)$	Voigt profile at no load
$f_V(u(t))$	Voigt profile as a function of Raman peak position at time t
$A_{\max}$	Maximum Raman peak shift during vibration

List of figures

Figure 1—1: Diagram of the Rayleigh and Stokes-Raman scattering processes. 8

Figure 1—2: Schematic illustration of Raman geometry... 9

Figure 2—2: Silicon crystal structure. 17

Figure 2—3: Cantilever beam diagram. 25

Figure 2—4: Failure location probability density 32

Figure 3—1: An illustration of a microcantilever beam 35

Figure 3—2: SOI wafer layers 37

Figure 3—4: Device dimensions (see table 3—2 for a particular device) 41

Figure 3—5: A silicon bar loaded under four-point bending 42

Figure 3—6: Four-point bending machine with a silicon bar loaded. 43

Figure 3—7: The piezoelectric actuator glued between two pieces of metal holder 44

Figure 3—8: Dies fixed on glass slide. 45

Figure 3—9: Four-point bending machine under the Zygo® profiler 46

Figure 3—10: Radius of curvature measured using the Zygo® surface profiler...... 47

Figure 3—11: Radius of curvature determination 47

Figure 3—12: Schematic of laser vibrometer system 48

Figure 3—13: HP 3562A signal analyser. 49

Figure 3—14: FRF from signal analyser working in linear resolution mode. 49

Figure 3—15: Maximum displacement measurements of in-plane motions. 52

Figure 3—16: Schematic of Raman system 53

Figure 4—1: Typical fitting of Raman profile data to a Voigt profile. 59

Figure 4—3: Peak position correction using Ne line wavenumber as a reference. .. 62

Figure 4—4: Static Raman shift and stress calibration 68

Figure 4—5: Anastassakis, Chandrasekhar and measured comparison 69

Figure 4—6: Simulation of Raman profile broadening 72

Figure 4—7: Comparison between analytical stress and measured stress. 73

Figure 4—8: Stress distribution across the beam surface....................................... 74

Figure 4—9: Stress distribution in the vicinity of the clamped end. 75

Figure 5—1: Mechanically polished surface profile.. 77

Figure 5—2: DRIE surface profile.. 78

Figure 5—4: Cumulative distribution plot of H13/J13 o fracture strength. 81

Figure 5—5: Probability plot of H13/J13 out-plane fracture strength..................... 82

Figure 5—6: Histogram plot of H13/J13 out-plane fracture strength...................... 82

Figure 5—7: Distribution analysis plot of H13/J13 in-plane fracture strength. 83

Figure 5—8: Probability plot of H13/J13 in-plane fracture strength. 84

Figure 5—9: Histogram plot of H13/J13 in-plane fracture strength........................ 84

Figure 5—10: Cumulative distribution plot of polished and DRIE surfaces 85

Figure 6—1: The device model. 89

Figure 6—2: An area Au in association with node u on the device surface............ 90

Figure 6—3: Typical predicted Weibull cumulative density of failure 91

Figure 6—4: Failure prediction of J02, J03 and J13 under out of plane mode 92

Figure 6—5: Failure prediction of J02, J03, H13 and J12 in plane mode............... 93

Figure 6—6: Predicted and tests results of J02 and J03 in in-plane mode.............. 95

Figure 6—7: Predicted and test results of J12 in in-plane mode 96

Figure 6—8: Predicted and tests results of J02 and J03 in out of plane mode 97

Figure 6—9: Scattered failure locations along the beam. 98

Figure 6—11: SEM image shows root rupture and propagated through [111] 99

Figure 6—12: SEM image shows root ruptured and propagated through [111] 99

Figure 7—1: Predicted failure strength characteristic.. 102

Figure 7—2: Relation of characteristic failure strength and surface type.............. 103

Figure 7—3: Fracture data scatter of the devices 104

Figure 7—4: Discrepancies of the predicted failure strength and test results. 105

Chapter 1. Introduction

1.1. Background

Microelectromechanical systems (MEMS) is a term that is widely used for small integrated devices that are made up of mechanical elements and electronics components having a size range between sub-micron level to millimetre level. MEMS extend the semiconductor device fabrication technologies normally used for the integrated circuit industry to add mechanical elements such as beams, combs, gears, diaphragms, and springs to devices.

MEMS technology has grown rapidly and together with increasing commercialization has created diverse developments in a wide range of fields, including automotive, aerospace, biotechnology and bioengineering, medicine and pharmaceutical, telecommunications and manufacturing. Studies in the field of microelectromechanical systems (MEMS) are interdisciplinary activities. Researchers from different backgrounds, including physics, engineering, mechanical, electrical, biology, materials science, and many others, have made significant contributions.

One of the primary goals of a MEMS device development is to design structures that not only operate as expected, but are also safe and reliable. The reliability of such devices becomes important due to their working environment and operating conditions. Most of these devices are employed in safety-critical fields such as automotive, aerospace and medical applications where failure of these structures can cause critical danger [1]. This makes the reliability studies of MEMS devices an importance issue [2-4].

MEMS devices are typically made from brittle material such as silicon, which is known as a brittle material having significant scattered value of fracture strength. It leads to the utilisation of statistical considerations to describe the probabilistic nature of material strength using Weibull cumulative distribution function rather than using deterministic terms [5-7]. The material strength is estimated under the weakest link theory (WLT) and has dependencies on the component size (size effect) and geometry/loading configuration [8, 9].

Furthermore, appropriate methods, tools, and techniques either in device performance tests, reliability assessments, and fabrication problem or failure mode identifications can assist to faster designs and development times of such devices. Due to the size of MEMS devices, optical techniques for characterization of static and dynamic properties of

MEMS are the most suitable methods [10]. Included in these techniques are laser vibrometry and optical profilometry which are as commercially available MEMS workstations for MEMS metrology. However, the techniques are limited to less than 30 MHz, and so are unsuitable for ultrahigh frequency MEMS resonators, and either need to be applied along the line of motion or by making use of a surface feature like an edge [11]. Raman spectroscopy is a technique offering additional advantages in the field of MEMS characterisation by its capability to give a measure of strain within the lattice in silicon from its shift of Raman profile peak position [12]. Extension to the conventional Raman spectroscopy method is dynamic Raman spectroscopy. The term 'dynamic' refers to Raman characterisation implemented to measure a dynamically loaded microstructure [11, 13, 14] allowing for an improvement in MEMS reliability prediction.

1.2. Motivation

This research work is intended to develop a reliability prediction method of single crystal silicon MEMS utilising dynamic Raman spectroscopy. Utilisation of dynamic Raman spectroscopy allows the gathering process of Weibull fracture test statistical data to be done directly on a device during its operation condition thereby taking account of actual geometrical tolerances, effects from the microfabrication process and dynamic load conditions. The ability of Raman spectroscopy to directly measure strain on a single crystal silicon device surface by capturing the shifting of the Raman spectra peak during static loading [12] and calculating the Raman spectra broadening during dynamic loading [11, 14] can eliminate inaccuracy of a finite element (FE) strain estimation because of inaccurate micromachined structures dimensional input to the FE model [15]. Acquiring this fracture data on devices will improve reliability prediction accuracy. Furthermore, the key advantage of using dynamic Raman spectroscopy is that a standard Raman system without any modification may be used and allows for simple sample preparation. This methodology is readily implementable by industry.

1.3. Aims and objectives

This work predominantly focused on reliability prediction of MEMS devices. A prediction technique exploiting the advantages and taking account of limitations of dynamic Raman spectroscopy was developed. The reliability prediction was made by predicting the failure of the structure. This failure prediction of MEMS structures was computed using ANSYS based on Weibull parameters of microstructures having same microfabrication processes with such structures. The parameters were investigated from a series of fracture test data of microcantilever beams under excessive harmonic loading

at their resonance frequency using dynamic Raman spectroscopy characterisation. Further, the prediction was compared with a series of fracture tests with varying geometry to evaluate the accuracy.

The specific objectives of the research can be summarised as follows:

- Establish a representative reliability/failure prediction equation for a harmonically displaced microcantilever beam.
- Calibrate peak position of silicon Raman profile on the Raman system.
- Determine the phonon deformation potential (PDP) to calibrate the relation between the Raman peak shifts with strain in silicon under static load.
- Determine the relation between Raman profile broadening with maximum strain induced from harmonic loading.
- Generate Weibull parameters for particular microfabricated processes of MEMS from a series of rupture tests.
- Make a failure prediction of a series of different MEMS geometries from the first in-plane and out-of-plane mode shapes by incorporating the Weibull parameters into the FE model.
- Analyse the experimental data to evaluate and validate the prediction method.
- Make a conclusion of the work and identify opportunities for future work

1.4. Reliability prediction of MEMS device

There is much interest on failure mode studies in the reliability prediction of MEMS to ensure the correct functioning of MEMS devices from just after fabrication until an extended period of time. These studies include material mismatches, fracture and fatigue, adhesion and stiction, friction and wear, electrostatic interference, radiation damage and thermal effects [16]. Mechanical failure of microstructures is a limiting factor for reliability of MEMS devices and has been the focus of considerable work.

Reliability prediction of a MEMS device predicts the failure based on its empirical material fracture data. For failure mode caused by a rupture of a MEMS microstructure, the reliability prediction of a MEMS device is made by predicting the fracture probability of such a structure. Most of the predictions are made by incorporating finite element analysis to simulate the response of operation conditions and loads. The utilisation of a finite element analysis is essential due to the complexity of the geometry of a MEMS device that precludes an analytical solution.

The reliability prediction developed in this research work is intended to be applicable to single-crystalline MEMS devices and considers the nature of the material, fabrication processes and its working conditions. Implementation of this method will allow more accurate and efficient evaluation of such devices. MEMS structures are usually made from single-crystalline silicon wafer, which is known as a brittle material. One can expect that wafer-grade single-crystalline silicon with mechanically polished surface has a very low lattice defect density that will make the whole volume of the material mechanically prefect in terms of defective flaws. In spite of the nature of the wafer perfection, MEMS microfabrication processes will change the surface roughness which affects the fracture strength of the structure and in turn will change its reliability [7]. A brittle material such as silicon with a lack of ductility can also be considered as having a lack of fracture toughness and exhibiting a low strain tolerance. These properties result in a considerably scattered in fracture strength. Without the presence of plastic deformation during a loading condition, a large stress concentration on the tip of a surface micro crack will be induced from which the failure of the structure is initiated. Therefore the combination of the nature of mechanical properties of this material and fabrication processes together may lead to a significant scatter in fracture even wider than predicted by a probabilistic approach.

1.4.1. Weibull weakest link theory

Single crystalline silicon is the predominant material being in used for MEMS devices due to its material properties advantages and its microfabrication techniques maturity inherited from microelectronic fabrication [15]. It is also well known as a brittle material having a widely scattered fracture strength data [7]. Thus, due to such scattered fracture strength data, Weibull fracture probability has become one of the best ways to describe its fracture behaviour to date [6, 17-19]. The Weibull fracture probability is also known as Weibull weakest link theory. The theory assumes that the structure is analogous to a chain with many links which may have a different fracture strength for each link. Thus, if such a weakest link within the chain is fails due to an applied load, then the structure fails [8, 20].

1.4.2. Flaw population due to micfabrication processes

The Weibull weakest link theory includes an assumption that the fracture strength depends mostly on the flaw population of the surface area/volume under stress [20, 21] due to the fact that the strength of a brittle material from experiment usually about two order weaker compared to its ideal strength [22].

In our case, the material is a semiconductor-grade single crystal silicon (SCS) having an extremely low lattice defect density that it can be said the material volume effectively has no mechanical defect, the flaw population will only be induced from the microfabrication processes. However, significant surface flaws are induced during the microfabrication processes of the device having a characteristics of which are specific to the microfabrication process type [7, 21, 23, 24].

This indicates that it is important to acquire the fracture data, which will be used for the prediction reference to be taken from a set of structures having the same microfabrication processes with the devices under development (or alternatively the device being predicted). It is expected that devices having the same microfabrication processes will have a similar flaw population thus will gives a same fracture strength characteristic.

1.4.3. Surface roughness and fracture strength relation

Surface flaws due to microfabrication processes may be quantified under roughness scales. The R_{max} values are common to be used to quantify roughness. A rougher surface is represented by a larger R_{max} value. However, there is no quantitative relation between the roughness value and the fracture strength. The roughness scale is used to distinguish the surface characteristic that the rougher the surface, the fracture strength will decrease [22].

Different fabrication processes introduces different surface roughness. This dissimilarity is attributed to the significantly different fracture strength. Explanation to this behaviour is that a rough surface is composed of craters and spikes intersecting at sharp peaks. During the loading, crack will initiates at one of the peaks inducing the failure. There is an abundance of these peaks lying on a rougher surface that a failure is more likely to occur. Thus, rougher surface decreases the fracture strength. One has shown the fracture strength of silicon microcantilever beam fabricated on (100) SOI wafer in <110> direction gives a significantly different fracture strength of 3.3 GPa average for reactive ion etching (RIE) process and of 1.0 GPa average for anisotropic etching (KOH) surface process [25].

1.4.4. The size effect

The Weibull statistical method is sensitive to the size effect, which is the volume or the area on which the stress is induced, also known as volume or area characteristic, the

different volume or area will change the appearance of the Weibull fracture strength so that the smaller the size the stronger the structure [8, 26-29].

Therefore, it is worth having the area characteristic of the prediction data close to the size of the device being predicted to minimise an unknown nonlinear relation between the real fracture strength with the flaw population over the surface.

1.4.5. Characteristic area variation due to different mode shape of vibration

For our experiment that incorporates vibrating cantilever beams, the size effect is not only induced from the different size of geometry but also induced by the different modes of motion. Different mode shape of motion of the beam results on a different strain/stress distribution over the beam. Thus, different stress/strain distribution over the beam have to be considered as it may results a different failure probability.

1.4.6. Fracture surface

There are two common fracture surface in single crystal silicon having a diamond cubic crystal structure, the (111) plane and the (110) plane. The (111) fracture mechanism is more expected because it has the lowest surface energy to overcome the crack propagation. However, along with this fracture mechanism, the (110) fracture mechanism usually is also occurred even it has a higher surface energy. Thus, the activation of the (110) cleavage planes requires more energy than that of the (111) planes with the fracture toughness K_{IC} (111) cleavage = 0.83 MN/m$^{3/2}$ and K_{IC} (110) cleavage = 0.94 MN/m$^{3/2}$. Loading geometry and boundary conditions can bring the secondary cleavage planes to be activated [30].

One mentioned there was a considerable variation in fracture strength due to the fracture surface on silicon crystal orientation. Specimens having fractured planes on (110) had an average strength of 3 GPa whilst those having fractured on (111) planes had strengths of less than 1 GPa [31].

1.5. Raman spectroscopy

As mentioned earlier, this work used Raman spectroscopy to characterise the single crystal silicon MEMS structure strain during its vibrational motion directly from the device to predict the reliability (or alternatively to predict the failure). Static and dynamic Raman spectroscopy were used. Calibration for both static strain and dynamic strain relation with the Raman spectrum shifting and broadening were also done during this work to ensure the reliability of the measurement results.

1.5.1. Basic physics of Raman Spectroscopy

A Raman spectrum is generated by exciting the sample MEMS device to a virtual state with a monochromatic light source, typically a laser. In our experiment we use an incident light of 632.8 nm HeNe laser beam. Most of the light will scattered with no change in its wavelength which is referred as elastic scattering and also known as Rayleigh scattering. However, there are very small amount of only one in 10^6-10^8 photons incident on the sample undergoes inelastic scatter which is referred as Raman scatter. In Raman scatter, the scattered radiation is shifted in energy that the shift is commensurate with the energy difference between the initial and final vibrational state. If the scattered photons have a lower energy level, it is considered to as Stokes scattering. In contrary, when the scattered photons have a higher energy level being compared to the incident photons energy, it will be referred to as anti-Stokes scattering [32, 33].

Generally, radiation is characterised by its wavelength(λ). Though, in spectroscopy, is often discussed in term of energy because the interest is in the interaction of radiation with states of the molecule. Thus, it is useful to use frequency (υ) or wavenumber (ω) scales, which are linearly related with energy term. The relationship between these terms are given [34]:

$$\lambda = \frac{c}{\upsilon} \tag{1—1}$$

$$\upsilon = \frac{\Delta \mathrm{E}}{h} \tag{1—2}$$

$$\omega = \frac{\upsilon}{c} = \frac{1}{\lambda} \tag{1—3}$$

where h is the Planck constant, E is the energy and c is the speed of light. The symbol ω will be used throughout this work to represent the reciprocal of the wavelength λ. The unit for wavenumber ω is the reciprocal centimeter (cm^{-1}) since it represents the number of waves per centimeter.

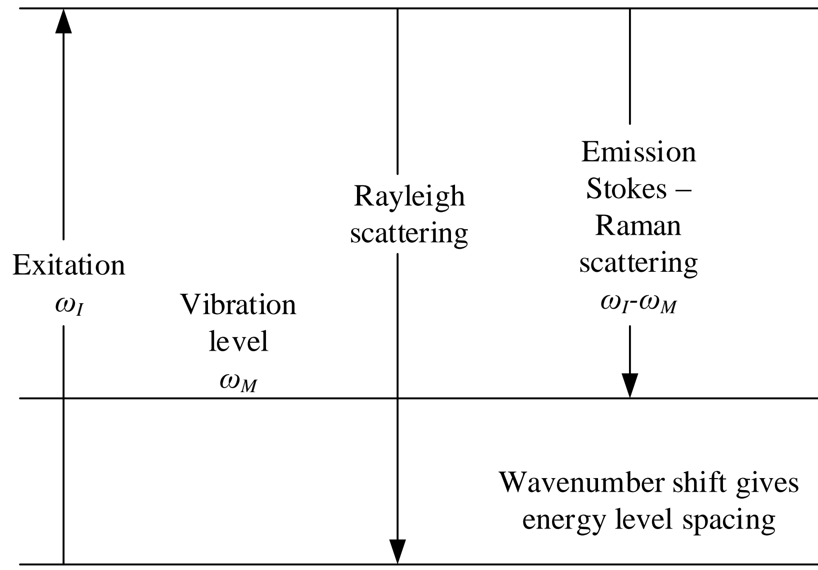

Figure 1—1: Diagram of the Rayleigh and Stokes-Raman scattering processes.

When the monochromatic light having a wavenumber of ω_I is incident on a system, this being either transparent gases, transparent liquids or optically transparent solids, most of the incident light will be transmitted without any change but some of the light will also be scattered. When such scattered light is analysed, rather than only ω_I being observed, there are also pairs of radiation light having wavenumbers of $\omega_0 = \omega_I \pm \omega_M$. These new wavenumbers are named after the Indian scientist C.V. Raman with K.S. Krishnan who first observed the phenomenon in liquid in 1928. These are two types of Raman bands, also called Raman shifts, the first one is those having wavenumbers less than the incident light of $\omega_I - \omega_M$ and is known as the Stokes band whilst the other one having wavenumbers higher than the incident light of $\omega_I + \omega_M$ is called the anti-Stokes band. The scattering light without change of the wavenumber is known as Rayleigh scattering. Usually, Raman scattering is recorded only on the low-energy side to give Stokes scattering. The schematic diagram of this Rayleigh and Stokes-Raman scattering phenomenon can be seen from Figure 1—1.

The Raman spectrum is plotted from the intensities or the number of Raman photons counted against the shifted energies. The x-axis usually labelled “Raman shift (cm^{-1})” or “Wavenumber (cm^{-1})”. The Raman shift represents the difference in the absolute wavenumber of the peak and the laser wavenumber.

1.5.2. Micro Raman spectroscopy

Application of Raman spectroscopy in MEMS reliability studies is also known as micro-Raman spectroscopy (MRS) since it is used to observe an area of the order of a few microns on the MEMS structure surface. The most common procedure of the MRS

application is to record the Raman peak shift due to a load applied to a test sample and compare it with the estimated strain [35].

1.5.3. Strain-dependent Raman spectrum on single crystal silicon

In this work, Raman spectroscopy is used due to its Raman shift dependency to the strain level in single crystal silicon. Strain caused by mechanical stress can affect the frequencies of the Raman mode. In the absence of strain, the triply degenerated phonons lead to a same peak at $\omega_0 = 520$ cm^{-1}. Strain changes the phonon vibrations and therefore can lift the degeneracy of the Raman frequencies. The Raman spectrum splits to a singlet and a doublet, and shifts linearly with the strain [36-38]. This phenomenon contains complete information to interpret the tensor nature of stress that destroys the degeneracy. However, to obtain all the Raman peaks is experimentally difficult and a polarised off-axis Raman spectroscopy setup is necessary [39, 40].

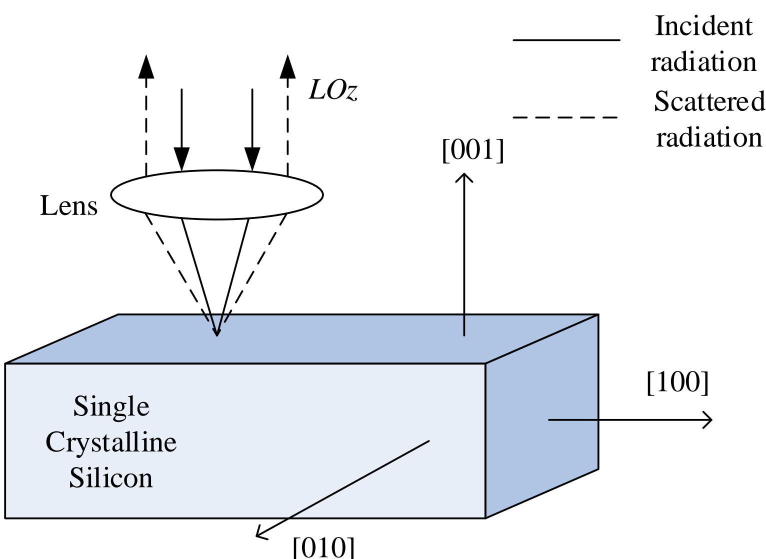

Figure 1—2: Schematic illustration of Raman geometry using [001] direction of incident and scattered radiation.

Due to this reason the [100] Raman geometry is selected to be used in this work to observe the load condition in MEMS characterisation with the drawback being that only partial information of the stress is determined. MEMS device samples for this experiment were fabricated on (100) single crystalline silicon wafers. The Raman spectroscopy characterisation was implemented on [001] Raman geometry. Both incident and collected scattered light are parallel to the [001] direction of the silicon crystal. Under this geometry the doublet transverse modes are polarised along [100] and [010] and the singlet longitudinal mode is polarised along [001]. For such a Raman geometry with crystal

coordinate system $x = [100]$, $y = [010]$, and $z = [001]$, only the longitudinal LO_Z can be observed [41, 42]. The schematic illustration of such Raman geometry can be seen in figure 1—2.

1.5.4. Dynamic micro-Raman spectroscopy

In this experiment, reliability tests (or failure tests of the samples) were done under dynamic load, hence a dynamic Raman spectroscopy is used to measure the strain in the sample structure under such a load. This measurement method continuously collects the scattered photons during a number of cycles of the MEMS structure motion. Thus, the MEMS structure undergoes cyclic tension and compression loads that the Raman spectrum shifted to the lower and higher wavelength repeatedly. Sum of a spread of those shifted Raman spectra gives overall profile that is broadened if compared to a single Raman spectrum [11, 14].

Having such a characterisation method during experiments, enables us to characterise the device down to the size order of the structure being predicted and observe it during its motion. This characterisation procedure distinguishes our reliability prediction to other published work as the stress/strain data is directly acquired from the sample surface during the operation condition.

1.6. Previous work

1.6.1. Reliability study of silicon MEMS devices under brittle fracture

Studies on failure analysis of brittle materials were usually derived using one of two perspectives. The first one is by relating the stress/strain in a material induced from loading to the material strength for example using Coulomb-Mohr failure criterion [43]. The other approach is based on fracture mechanics that relates the stress intensity factor of a particular crack to the fracture toughness of the material and considers it as a material property [22, 44, 45].

The mechanical failure of the microstructure in a microsystem is one of the problems that limits its utilisation for critical operations. Efforts have been made by researchers to characterise the fracture behaviour and predict the failure by using empirical test data combined with analysis. A number of materials typically used for MEMS devices are polycrystalline silicon [7, 46], single crystalline silicon [47, 48], and single crystal silicon carbide [28, 49, 50]. Various procedures including uniaxial specimens [29, 51-53], biaxial plate specimens [21], three-point bending [52], four-point bending [15] or cantilever beam bending [25] were used by the researchers for gathering the empirical test data. A

non-conventional procedure incorporating a wrapped micro cantilever beam over a curved sidewall was also proposed [54]. However, sample preparation on a micron scale is cumbersome for example impractical loading arrangements and problematic specimen alignment.

It was found that the materials exhibited brittle fracture behaviour with large scatter of fracture strength. The study on dealing with the strength distribution of brittle material was published by Wallodi Weibull [8, 20]. The theory was named after him. Although he was not the first person that worked on the problem, he was instrumental in promoting the technique. The Weibull distribution is widely used to date and most studies agree that the theory is appropriate to in utilisation for fracture strength prediction in MEMS devices.

FE modelling is also incorporated to take advantage of computer computation capability, i.e. NASA Ceramics Analysis and Reliability Evaluation of Structures (CARES/Life) software describes the material strength scattering behaviour by utilising the Weibull cumulative distribution function. This software combines the capability of fracture analysis, probabilistic modelling, and brittle structure design to make a failure prediction of monolithic ceramic components [7, 51, 55]. ANSYS Multiphysics was also in use to predict the reliability of single crystal silicon MEMS devices by informing the statistical fracture data to its postprocessing algorithm [15, 56].

Due to the common utilisation of semiconductor standard SOI (silicon on insulator) wafer that considered to have an extremely low lattice defect density [7, 23], researchers also take account on microfabrication processes to predict the failure. Microfabrication processes induce a flaw population across the affected device surface leading to failure. Assuming that the reliability of MEMS micro devices depends only on the device surface areas, the key factors are the surfaces characteristics, affected by etching types, and the stresses acting on these areas for a given fabrication process. Weibull probability function describing the flaw population incorporated with FE analysis computation is used in these procedures [6, 7, 57].

Furthermore from the significant scatter of failure strength, the location prediction of rupture is also of interest. As suggested from the nature of failure strength scatter, the rupture location is also distributed along the test specimens and was also described under the Weibull distribution [58].

1.6.2. Optical Techniques in MEMS Characterisation

The importance of suitable optical techniques for characterization of static and dynamic properties of MEMS/NEMS is acknowledged. Appropriate techniques either in device performance tests, reliability assessments or fabrication problem identifications can assist to faster designs and development times of such devices. General requirements for an optical MEMS characterization system are mentioned by Bosseboeuf and Petitgrand [10]; these include abilities to perform both static and dynamic measurements as well as out-of-plane and in-plane measurements with a high sensitivity and a large dynamic measurement range.

For the last decade, there has been much effort dedicated on MEMS characterization techniques. Particular advantages of those characterization techniques for dynamic micro and nanoscale devices have been reported by researchers, such as high sensitivity [59], fast and simple characterization [60], direct on wafer testing with a number of single elements in parallel [61], wide measurements range [61-63], and related limitations. Examples include laser Doppler vibrometer [59], stroboscopic phase-shifting interferometer [62], electronic speckle pattern interferometry [61], laser TV holography [63] and blur synthesis [60].

Problems with these techniques are that they are either limited in frequency to less than 30 MHz, require the measurement to be performed along the line of motion, need to utilize a surface feature or are generally not straightforward. In addition, in reliability studies of MEMS/NEMS, these techniques can only give an indication of the mechanism of device failure once it has occurred or are of limited applicability only to a device designed to fail at a certain point [64].

1.6.3. Raman spectroscopy

Raman spectroscopy, which is being increasingly used to date for MEMS/NEMS characterization, has capabilities to determine material properties, indicate crystallinity and measure strain within the lattice. Since its linear relation behavior to strain in silicon was published [65], the characterization method has been utilized to measure local mechanical stresses [66-70] and to produce a submicron stress map of a plastically deformed area of a silicon wafer [71]. Recently, dynamic stress quantification [13], motion and strain levels measurement [72], and mode shape [64] using dynamic Raman spectroscopy in dynamic micromechanical structures has been shown. There are two different procedures in dynamic Raman characterisation. The first procedure is implemented by strobing the light synchronised with a particular phase position during

the motion so that the movement of the vibrating beam is “frozen” in such a position [13, 14]. The second procedure is executed by collecting all of the Raman profile during the motion so that the total profile looks broaden. The strain then can be interpreted from the profile broadening [11].

Most procedures were implemented under [100] Raman geometry and assumed as a uniaxial stress system, which limits the capability to characterise the nature of the stress tensor. Tensor-resolved techniques are also proposed to overcome the limitations. Either polarised [35, 40, 73, 74] or off-axis [39, 75] Raman spectroscopy which selectively observes a Raman-active optical phonon mode has the capability to characterise the stress tensor in silicon. These techniques are performed either by polarising the light beam and incorporating an improved analysis procedure or by utilizing a tilted incident light setup. The Raman-active optical phonon mode is to refer that the elementary vibrational motion in which a lattice of atoms or molecules uniformly oscillates at a single frequency will induces a Raman scattering when the sample is illuminated with a laser beam [76].

Recent advances in instrument technology have simplified the equipment and reduced the problems substantially. These advances, together with the ability of Raman spectroscopy to examine dynamic structures of MEMS/NEMS, have led to a rapid growth in the application of the technique. In addition, modern Raman spectroscopy is simple, variable instrument parameters are few, spectral manipulation is minimal and a simple interpretation of the data may be sufficient. However, utilizing Raman spectroscopy in this field is an underdeveloped technique, with much important information is often still not used or recognized [77].

1.7. Thesis overview

The thesis consists of eight chapters.

Chapter 1 introduces the background and motivation that relates to the aims and objectives of this thesis. A concise discussion of MEMS, reliability predictions and Raman characterisation was given. A review of previous work that relates to this thesis was also included.

Chapter 2, introduces the reliability prediction method in used in this work. The discussion details on the development of the fracture model incorporating the Weibull distribution. Probability of failure considering a non-uniform stress distribution is composed together with the prediction of rupture position along the cantilever beam.

Weibull parameter determination and its conversion between characteristic parameter to material scale parameter are also discussed.

Chapter 3, describes the equipment and procedures used during the experiment. Utilisations of the surface profiler, laser vibrometer, four-point bending machine, Raman setup and sample preparation were discussed. Device fabrication and device geometry were considered in this chapter.

Chapter 4, this chapter only discusses the Raman spectroscopy. It starts with an introduction of the system and technology available and continues with a calibration of static and dynamic Raman spectroscopy. The reliability of such a Raman method is also discussed.

Chapter 5, focuses on the Weibull parameter determination. Statistical work is discussed and the results presented

Chapter 6, implementation of the prediction method is done in this chapter. The method is coded into the APDL (Ansys Parametric Design Language) and executed to obtain the failure prediction of every device in interest. Validations of the method by comparing it with the result of fracture test of such devices are made. Discrepancy between the prediction and the test results are presented.

Chapter 7, in this chapter, a discussion to evaluate the failure prediction and its comparison to the test result are presented. The possible causes of the discrepancy are also discussed.

Chapter 8, concludes the work and discusses the technology available to overcome the discrepancy issue and to improve the capability and the reliability of the reliability prediction method of MEMS devices.

Chapter 2. Reliability Prediction

2.1. Introduction

Methodology and procedures of the reliability prediction of a structure manufactured from a brittle material such as MEMS structures from single-crystal silicon utilising Weibull fracture distribution have been briefly reviewed in the previous chapter. In this chapter, those procedures are extended to take account of a harmonic load applied to the structure and incorporated with the implementation of the Raman dynamic characterisation.

As in the nature of Weibull fracture distribution utilisation, statistical size effect occurs for a broad class of brittle structures that follow the weakest-link model. The application of such harmonic loading will affecting the characteristic area A_0 of the Weibull formula and eventually will affect the appearance of the Weibull strength [26-29]. In the static load, the characteristic area is only affected by the magnitude of applied load whilst in harmonic load the characteristic area is affected by both the magnitude of the load and its mode shape. In applying such a load, the structure also has a possibility of being affected by fatigue [46, 78, 79]. Furthermore, as there is a significantly scattered fracture strength, the rupture position distribution is also of interest.

2.2. Assumption

As the fracture algorithm in this work is developed under a statistical analysis procedure, i.e. a two-parameter Weibull distribution with size-effect consideration, its applicability and accuracy in a given condition will depend heavily on any basic assumptions included into the algorithm. For this reason, it is important to state and evaluate all the assumptions made.

It is assumed that the material fracture strength depends critically on the flaw population. This assumption comes from Griffith. In his memorable paper “The Phenomena of Rupture and Flow in Solids”, he concluded that the typical brittle solid must include a large amount of submicron flaws as a source of weakness due to the fact that the real material ruptured usually by two orders of magnitude lower compared to an ideal solid of such a material [22]. As semiconductor-grade single crystal silicon, which is usually used in MEMS devices, has an extremely low lattice defect density within the volume and effectively has no mechanical defects, the flaws induced from the microfabrication process, which are specific to the process type [21], may only be considered on the surface. Thus, the failure prediction can be made as a function of a

flaws population on the surface instead of the volume. In single-crystalline silicon MEMS manufacturing, it is distinguished that the fracture strength of the given device having such microfabrication processes is not highly reproducible and significantly scattered. Therefore, it is indicated that flaw statistic is the main consideration to determine the strength variability of the device. The most common distribution used is the Weibull distribution with its consideration of a weakest link model to describe the behaviour of the failure strength of such a device structure that heavily reflects an empirical tradition instead of analytical calculations [5-7].

The weakest link model assumes that macro-fracture initiation from one material element, or more precisely one representative volume element (RVE), causes the whole structure to fail, like the failure of one link in a chain [8]. The RVE term is defined as the smallest material volume whose failure is sufficient to bring the whole structure to fail.

Quasi-static fracture analysis is used in this work by assuming that even the applied load to the structure is a dynamic load, it can be considered as a steady-vibratory state. The advantage of this analysis is that it allows for a static analysis instead of evaluating the problem as a dynamic fracture with an elastodynamic consideration. It is also assumed that the failure of the structure is mainly due to the applied load i.e. the structure response due to vibratory load. Other effects such as creep, strain rate dependence, stress gradient dependence, static fatigue and cyclic fatigue are considered to be insignificant or entirely absent. Furthermore, the mechanical loading is assumed as known deterministically from measurement and calculation. Also, in the stress analysis of the brittle structure, it is assumed that the material is homogeneous, at uniform temperature, isotropic and linearly elastic.

2.3. Single crystal silicon properties

The most widely used material that is used in MEMS structure is single crystalline silicon (SCS). Single crystalline silicon has a lattice cubic symmetry in which all directions and planes perpendicular from each other are equivalent.

Figure 2—1 shows the silicon crystal structure with Miller index crystallographic notation. The direction is designated with respect to crystal basis using Miller indexes. For cubic crystal silicon, the direction of [100], [010] and [001] can be chosen to coincide with x, y and z axes, as shown in Figure 2—2.

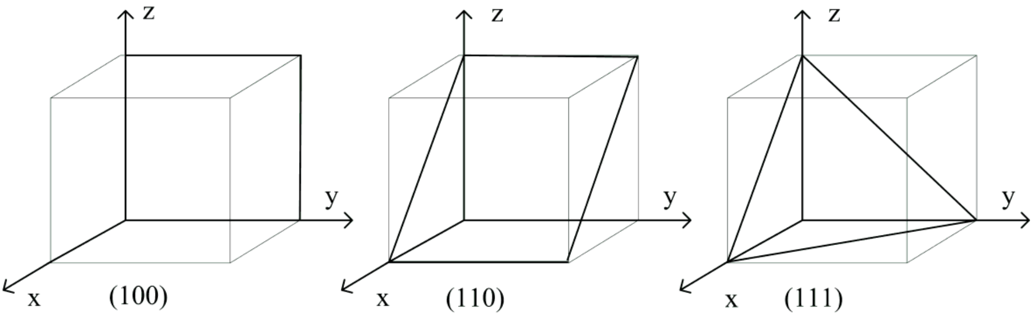

Figure 2—1: The principal planes of single crystalline silicon.

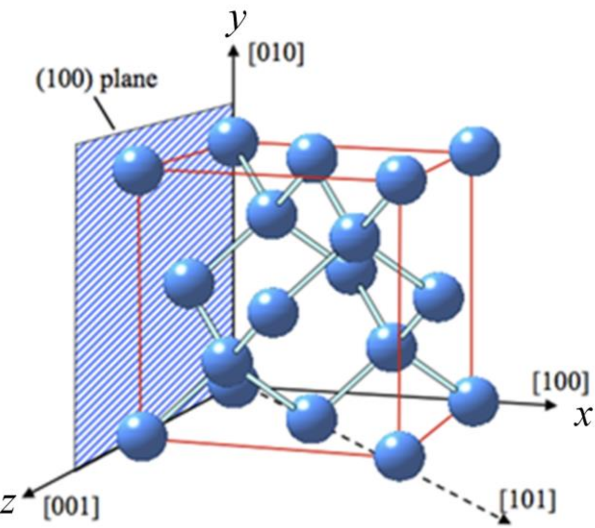

Figure 2—2: Silicon crystal structure. Picture was taken from: /www.kaajakari.net

2.3.1. Anisotropic elasticity

Hooke's law describes the elasticity as the relation between stress (σ) and strain (ε) in terms of stiffness C and compliance S given by:

$$\sigma = C\varepsilon \;;\; \varepsilon = S\sigma \tag{2—1}$$

For the special case of an isotropic material, the stiffness matrix C may be considered as a single value of $\mathbb{E}$ that is known as Young's modulus. In its general terms the anisotropic behaviour is described with a 4th rank elastic constants tensor C_{ijkl} to relate the stress and strain 2nd rank tensors such that the equation 2—1 can be rewritten in the general form of Hooke's law as given by:

$$\sigma_{ij} = C_{ijkl}\varepsilon_{kl} \;\;;\;\; \varepsilon_{ij} = S_{ijkl}\sigma_{kl} \tag{2—2}$$

It is convenient to adopt the convention that for the subscripts appears twice in the same term; the summation over those subscripts from one to three is implied. The equation 2—2 then becomes as:

$$\sigma_{ij} = \sum_{k=1}^{3}\sum_{l=1}^{3} C_{ijkl}\varepsilon_{kl} \tag{2—3}$$

That to calculate σ_{ij}, we should begin like so:

$$\sigma_{11} = C_{1111}\varepsilon_{11} + C_{1112}\varepsilon_{12} + C_{1113}\varepsilon_{13} + C_{1121}\varepsilon_{21} + C_{1122}\varepsilon_{22} + C_{1123}\varepsilon_{23} + C_{1131}\varepsilon_{31} + C_{1132}\varepsilon_{32} + C_{1133}\varepsilon_{33} \tag{2—4}$$

thus the expansion of equation 2—3 by continuing the equation 2—4 for all σ_{ij} will produce 9 equations, each with 9 terms, leading to 81 elastic C constants in all. The fourth-order elasticity tensor C_{ijkl} contains all of the elastic stiffness moduli yet may be simplified due to the existence of the symmetry that comes from the symmetry of the stress and strain tensors $C_{ijkl} = C_{jikl} = C_{ijlk}$ and comes from arguments based on the existence of the strain energy function $C_{ijkl} = C_{klij}$. Thus the symmetries together $C_{ijkl} = C_{jikl} = C_{ijlk} = C_{klij}$ can reduce the 81 elastic terms within C_{ijkl} to a set of 21 elastic moduli for the general case. A homogeneous material should be assumed that the elastic moduli are spatially independent.

Symmetric tensor means that the off-diagonal components are equal as shown in the second term of equation 2—5. The third term shows the contracted notation of six different components on the stress tensor as follows:

$$\begin{pmatrix} \sigma_{11} & \sigma_{12} & \sigma_{13} \\ \sigma_{21} & \sigma_{22} & \sigma_{23} \\ \sigma_{31} & \sigma_{32} & \sigma_{33} \end{pmatrix} = \begin{pmatrix} \sigma_{11} & \sigma_{12} & \sigma_{13} \\ \sigma_{12} & \sigma_{22} & \sigma_{23} \\ \sigma_{13} & \sigma_{23} & \sigma_{33} \end{pmatrix} = \begin{pmatrix} \sigma_{1} & \sigma_{6} & \sigma_{5} \\ \sigma_{6} & \sigma_{2} & \sigma_{4} \\ \sigma_{5} & \sigma_{4} & \sigma_{3} \end{pmatrix} \tag{2—5}$$

Similarly, the strain tensor can also be written in the stress tensor fashion. Further, it is common that one represents the six different components of stress-strain tensor relation using 36 (6x6) independent components of stiffness matrix format as:

$$\begin{pmatrix} \sigma_1 \\ \sigma_2 \\ \sigma_3 \\ \sigma_4 \\ \sigma_5 \\ \sigma_6 \end{pmatrix} = \begin{pmatrix} C_{11} & C_{12} & C_{13} & C_{14} & C_{15} & C_{16} \\ C_{21} & C_{22} & C_{23} & C_{24} & C_{25} & C_{26} \\ C_{31} & C_{32} & C_{33} & C_{34} & C_{35} & C_{36} \\ C_{41} & C_{42} & C_{43} & C_{44} & C_{45} & C_{46} \\ C_{51} & C_{52} & C_{53} & C_{54} & C_{55} & C_{56} \\ C_{61} & C_{62} & C_{63} & C_{64} & C_{65} & C_{66} \end{pmatrix} \begin{pmatrix} \varepsilon_1 \\ \varepsilon_2 \\ \varepsilon_3 \\ \varepsilon_4 \\ \varepsilon_5 \\ \varepsilon_6 \end{pmatrix} \quad (2—6)$$

From above relation, the equation 2—2 can be written in a compact notation as:

$$\sigma_i = C_{ij}\varepsilon_j \quad (2—7)$$

As mentioned earlier, the symmetry imposed by strain energy implies that the stiffness matrix C (6×6) is symmetric. It is of $C_{ij} = C_{ji}$ that implies only 21 independent elastic constant exist. Finally for the general term, the 81 components and the 21 components elasticity tensor are related by the expression:

$$C_{ij} = \begin{pmatrix} C_{1111} & C_{1122} & C_{1133} & C_{1123} & C_{1131} & C_{1112} \\ & C_{2222} & C_{2233} & C_{2223} & C_{2231} & C_{2212} \\ & & C_{3333} & C_{3323} & C_{3331} & C_{3312} \\ & & & C_{2323} & C_{2331} & C_{2312} \\ & & & & C_{3131} & C_{3112} \\ & & & & & C_{1212} \end{pmatrix} \quad (2—8)$$

The same procedure can also be established to the compliance matrix that equation (2—2) can be seen as:

$$\varepsilon_i = S_{ij}\sigma_j \quad (2—9)$$

For silicon having a cubic symmetry there are three independent elastic constant to describe the elastic behaviour that is given as:

$$C_{ij} = \begin{pmatrix} C_{11} & C_{12} & C_{12} & 0 & 0 & 0 \\ C_{12} & C_{11} & C_{12} & 0 & 0 & 0 \\ C_{12} & C_{12} & C_{11} & 0 & 0 & 0 \\ 0 & 0 & 0 & C_{44} & 0 & 0 \\ 0 & 0 & 0 & 0 & C_{44} & 0 \\ 0 & 0 & 0 & 0 & 0 & C_{44} \end{pmatrix} \quad (2—10)$$

It is common in a cubic crystal like silicon that the [100] directions represent a Cartesian xyz axis. Thus stress and strain relationships for directions aligned with those axes can be calculated as:

$$\begin{pmatrix}\sigma_1\\ \sigma_2\\ \sigma_3\\ \sigma_4\\ \sigma_5\\ \sigma_6\end{pmatrix} = \begin{pmatrix}C_{11} & C_{12} & C_{12} & 0 & 0 & 0\\ C_{12} & C_{11} & C_{12} & 0 & 0 & 0\\ C_{12} & C_{12} & C_{11} & 0 & 0 & 0\\ 0 & 0 & 0 & C_{44} & 0 & 0\\ 0 & 0 & 0 & 0 & C_{44} & 0\\ 0 & 0 & 0 & 0 & 0 & C_{44}\end{pmatrix}\begin{pmatrix}\varepsilon_1\\ \varepsilon_2\\ \varepsilon_3\\ \varepsilon_4\\ \varepsilon_5\\ \varepsilon_6\end{pmatrix} \quad (2\text{—}11)$$

where the value of C_{11}= 165.7 GPa, C_{12}= 63.9 GPa, and C_{44}= 79.6 GPa.

For our devices fabricated on a [100] standard silicon wafer and the Cartesian axis $x - y$ was designed to coincide with the [110] silicon crystal directions can be described in an orthotropic expression as given by [80]:

$$\begin{pmatrix}\sigma_1\\ \sigma_2\\ \sigma_3\\ \sigma_4\\ \sigma_5\\ \sigma_6\end{pmatrix} = \begin{pmatrix}C_{11} & C_{12} & C_{13} & 0 & 0 & 0\\ C_{12} & C_{11} & C_{13} & 0 & 0 & 0\\ C_{13} & C_{13} & C_{33} & 0 & 0 & 0\\ 0 & 0 & 0 & C_{44} & 0 & 0\\ 0 & 0 & 0 & 0 & C_{44} & 0\\ 0 & 0 & 0 & 0 & 0 & C_{66}\end{pmatrix}\begin{pmatrix}\varepsilon_1\\ \varepsilon_2\\ \varepsilon_3\\ \varepsilon_4\\ \varepsilon_5\\ \varepsilon_6\end{pmatrix} \quad (2\text{—}12)$$

where the value of C_{11}= 194.5 GPa, C_{12}= 35.7 GPa, C_{13}= 64.1 GPa, C_{33}= 165.7 GPa, C_{44}= 79.6 GPa and C_{66}= 50.9 GPa.

2.4. Fracture probability

In general, the probability of an infinite brittle material of getting a fracture failure δf depends on its failure function ψ and the internal stress σ due to an applied load It can thus be said [8]:

$$\delta f = \delta f[\psi(\sigma)] \quad (2\text{—}13)$$

with $\delta f \geq 0$, σ is a continuous random variable and $\int_{-\infty}^{\infty} \delta f[\psi(\sigma)]d\,\sigma = 1$.

From the fracture consideration that the failure is mostly from tensile rather than compressive stresses, therefore it can be said that $\delta f = 0$ for $\sigma \leq 0$. Depends on the internal stress determined from an applied load to a structure, the material is very likely to fail, $\delta f = 1$, when the stress is very large, and it is very likely to withstand the load, $\delta f = 0$, when the stress is very small or it can be said $\int_{0}^{\infty} \delta f[\psi(\sigma)]d\,\sigma = 1$.

2.4.1. Review of Weibull Weakest Link Failure Theory

The Weibull approach to describe a failure is referred as the weakest link model where failure of any part within a structure will lead the entire structure to fail. Considering a

structure with volume V consisting of N number of infinitesimal volume elements δV that can be described as:

$$V = \int_V dV = \lim_{N\to\infty} \sum_{\lambda=1}^{N} \delta V_\lambda. \tag{2—14}$$

For an infinitesimal volume δV, the probability of the volume to fail δf as a monotonously increasing function of such stress can be considered to be given by:

$$\delta f = \psi[\sigma_{ij}(p)]\delta V \tag{2—15}$$

where $\psi(\sigma)$ is a failure function that depends on the stress state $\sigma_{ij}(p)$ of an infinitesimal element volume δV at point p. As there are only two possible states of possibility of rupture δr of such volume due to the applied load, withstand the load or ruptured, then $\delta r = 0$ for a very heavy load and $\delta r = 1$ for a very low load. Its probability to withstand the load can now be described as:

$$\delta r = 1 - \delta f = 1 - \psi[\sigma_{ij}(p)]\delta V. \tag{2—16}$$

As it is assumed that the continuum is considered to be a chain consisting of links connected in series, then the strength of this continuum is governed by the strength of the weakest link. It is also assumed that the event of a link failure which leads the continuum to fail is independent of any other link in the chain. Hence, by rendering the theory of probability for events occurring simultaneously and independently, the probability r of such a structure to withstand an applied load of N events of N infinitesimal elements having the probabilities of δr_1, δr_2, δr_3, ..., δr_N can be obtained by multiplying the N individual probabilities as given [81]:

$$r = \lim_{N\to\infty} \prod_{\lambda=1}^{N} \delta r_\lambda$$

$$r = \lim_{N\to\infty} \prod_{\lambda=1}^{N} \{1 - \psi[\sigma_{ij}(p)]\delta V_\lambda\}. \tag{2—17}$$

This can equivalently be written in summation form by adding the natural log to both sides as:

$$\ln r = \lim_{N\to\infty} \sum_{\lambda=1}^{N} \ln\{1 - \psi[\sigma_{ij}(p)]\delta V_\lambda\}. \tag{2—18}$$

as the infinitesimal volume δV_λ is very small so $[\sigma_{ij}(p)]\delta V_\lambda \ll 1$, hence the above equation can be simplified since the Taylor series expansion for $x \ll 1$ is:

$$\ln(1+x) = x - \frac{1}{2}x^2 + \frac{1}{3}x^3 - \frac{1}{4}x^4 + \frac{1}{5}x^5 + \cdots \tag{2—19}$$

$$\ln(1+x) \approx x \tag{2—20}$$

thus simplifying equation (2—18) to:

$$\ln r = \lim_{N\to\infty} \sum_{\lambda=1}^{N} -\{\psi[\sigma_{ij}(p)]\delta V_\lambda\} = -\int_V \psi[\sigma_{ij}(p)]dV. \tag{2—21}$$

This can also be written as:

$$r = \exp\left\{-\int_V \psi[\sigma_{ij}(p)]dV\right\}. \tag{2—22}$$

Considering the two parameters Weibull cumulative distribution function (CDF) of fracture failure of structures under uniformly distributed uniaxial stress which has given by [8]:

$$f = 1 - \exp\left[-\left(\frac{\sigma}{\sigma_\theta}\right)^m\right] \tag{2—23}$$

or, in term of the failure function ψ, the Weibull distribution can be rewritten from the above equation as:

$$\psi = \left(\frac{\sigma}{\sigma_\theta}\right)^m \tag{2—24}$$

where m is the Weibull modulus, also called the shape parameter, where represents the scatter degrees of fracture data whilst σ_θ is the characteristic strength. The characteristic strength is determined when the cumulative failure probability is at 0.6321 (this value determined from equation (2—23) when $\sigma = \sigma_\theta$). The characteristic strength is dependent on the uniaxial test specimen and the value will change according to a different

size and/or geometry. Thus for its utilisation on a different loading condition, the characteristic strength σ_θ should be converted to the Weibull material scale parameter σ_0 which is independent of specimen size and geometry. Due to this independency, the material scale parameter should have a dimension of stress.volume$^{1/m}$ (GPa.m$^{3/m}$) rather than only stress (GPa) [82]. By substituting the Weibull material scale parameter σ_0 to the characteristic strength σ_θ from equation (2—24) and explicitly mention the size and geometry of the sample (represented by volume V_0 and non-uniform stress distribution $\sigma_{ij}(p)$ due to different geometry) which was included in σ_θ before into the equation as:

$$\psi = \frac{1}{V_0}\left(\frac{\sigma_{ij}(p)}{\sigma_0}\right)^m \qquad (2—25)$$

Then, the probability of a structure to withstand the load r in equation (2—22), by considering the Weibull distribution in the form of a failure function ψ in equation (2—25), can be rewritten as a failure probability of a structure having a non-uniform stress distribution over the volume as:

$$f = 1 - r = 1 - \exp\left\{-\int_V \psi\left[\frac{1}{V_0}\left(\frac{\sigma_{ij}(p)}{\sigma_0}\right)^m\right] dV\right\}. \qquad (2—26)$$

For the application in this experiment, the failure is assumed to always start from the surface and therefore the integration is made over the surface area under the load rather than the volume of the device structure. Hence, the above equation can be written as:

$$f = 1 - r = 1 - \exp\left\{-\int_A \psi\left[\frac{1}{A_0}\left(\frac{\sigma_{ij}(p)}{\sigma_0}\right)^m\right] dA\right\}. \qquad (2—27)$$

2.4.2. Differential probability of failure of a non-uniform stress distribution device

As the nature of the flexural stress distribution which was in use in this experiment work is such that the stress is non-uniformly distributed over the structure volume, a differential form of the failure probability of a volume element δV having a stress state of σ_{ij} suggested by Cassenti [58] is in use. He suggested that the probability of failure δf of an infinitesimal volume element δV will increase to $\delta f + d(\delta f)$ when the stress state is increased infinitesimally to $\sigma_{ij} + d\sigma_{ij}$ given by:

$$\delta f + d(\delta f) = \psi(\sigma_{ij} + d\sigma_{ij})\delta V \tag{2—28}$$

with $d(\delta f)$ is the probability of such a volume to fail between a stress condition of σ_{ij} and $\sigma_{ij} + d\sigma_{ij}$. By referring the first mentioned probability to failure δf of an element volume δV, the above equation can also be written to as:

$$d(\delta f) = [\psi(\sigma_{ij} + d\sigma_{ij}) - \psi(\sigma_{ij})]\delta V. \tag{2—29}$$

Expanding using the Taylor series about σ_{ij}, the failure characteristic function ψ can be written as follows:

$$\psi(\sigma_{ij} + d\sigma_{ij}) = \psi(\sigma_{ij}) + \frac{\frac{\partial\psi(\sigma_{ij})}{\partial\sigma_{ij}}}{1!}d\sigma_{ij} + \frac{\frac{\partial\psi^2(\sigma_{ij})}{\partial{\sigma_{ij}}^2}}{2!}(d\sigma_{ij})^2 + \cdots \tag{2—30}$$

Then, by neglecting the small second order derivative and above, the probability of failure of the element δV between the stress condition of σ_{ij} and $\sigma_{ij} + d\sigma_{ij}$ can be written as:

$$d(\delta f) = \frac{\partial\psi(\sigma_{ij})}{\partial\sigma_{ij}}d\sigma_{ij}\,\delta V. \tag{2—31}$$

Further, by adopting the basic assumption of the weakest link theory that only one infinitesimal volume element need fail for failure of the total structure volume, then by implementing this assumption Cassenti [58] also suggests the probability of such an infinitesimal volume δV, which resides within a structure volume V, to fail between a stress condition of σ_{ij} and $\sigma_{ij} + d\sigma_{ij}$ is:

$$d(\delta f)^{\circ} = rd(\delta f) \tag{2—32}$$

giving:

$$d(\delta f)^{\circ} = \exp\left\{-\int_V \psi[\sigma_{ij}(p)]dV\right\}\frac{\partial\psi(\sigma_{ij})}{\partial\sigma_{ij}}d\sigma_{ij}\,\delta V. \tag{2—33}$$

The probability δf° of such an infinitesimal volume δVfailing can be determined by integrating the above equation about the applied stress σ_{ij}:

$$\delta f^{\circ} = \int_{0}^{\sigma_{ij}} \exp\left\{-\int_{V} \psi[\sigma_{ij}(p)]dV\right\} \frac{\partial\psi(\sigma_{ij})}{\partial\sigma_{ij}} \delta V d\sigma_{ij}. \quad (2—34)$$

2.4.3. Dynamic model of the structure

Cantilever beams with end mass were designated to carry out the dynamic load tests and were used in the entire experiment. Each beam was driven to a certain load to get a required displacement and strain for characterisation. An excessive load was applied to cause the cantilever to fail.

A dynamic model that gives an analytical approximation of the stress distribution on the beam is derived in this section.

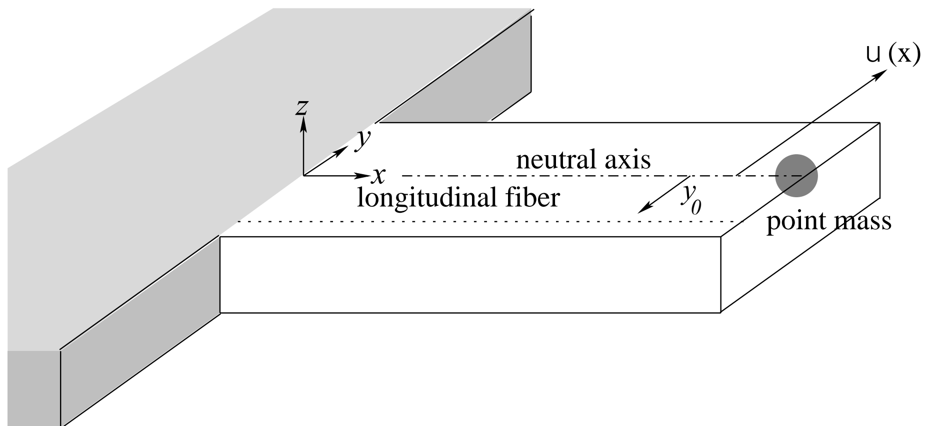

Figure 2—3: Cantilever beam diagram; with unit vector of *x*, *y*, *z* parallel to [110], [-110] and [001] respectively.

As the devices were ruptured during vibration, a dynamic model of the structure should be considered. For the cantilever beam used in this experiment, as shown in Figure 2—3, it may be modelled as a cantilever beam with large end mass.

Considering the Euler-Bernoulli beam assumption, a beam with a uniform cross section and homogenous material that is subjected to a couple of pure bending in the in-plane y direction will experience a tensile and compressive axial strain, σ_{xx}, in the x direction. The magnitude of the stress is varied linearly in the y direction, $\sigma_{xx} = \sigma_{xx}(y)$, due to the fibre position distance to the neutral axis as given by [83]:

$$\sigma_{xx}(y) = E\, y_0 \kappa \ , \quad (2—35)$$

where κ is the curvature of the flexural. The stress is zero on the neutral axis and with maximum compression and tension stress achieved at $-w/2$ and $w/2$ respectively, the above equation can be rewritten as:

$$\sigma_{xx}(y) = \frac{1}{2}Ew\kappa\left(\frac{2y}{w}\right) \tag{2—36}$$

with $-w/2 \leq y \leq w/2$.

For a vibrating cantilever beam, the axial stress is also varied in the x direction due to the mode shape curvature variation along the beam length $\kappa = \kappa(x)$ that can be written as:

$$\sigma_{xx}(x, y) = \frac{1}{2}Ew\kappa(x)\left(\frac{2y}{w}\right) \tag{2—37}$$

where $\kappa(x)$ is the curvature along the beam. For a large beam deflection, the radius of curvature is given by [84]:

$$\kappa(x) = \frac{\vartheta''(x)}{[1 + \vartheta'(x)^2]^{3/2}} \tag{2—38}$$

where $\vartheta(x)$ is the in-plane deflection of the neutral axis. Since the cantilever is driven to vibrate at its resonance frequency, the deflection of the beam can also be described in terms of its mode shapes as:

$$\vartheta(x) = \lambda_s X(x) \tag{2—39}$$

with

$$\lambda_s = 0.5\,\vartheta_L \tag{2—40}$$

where λ_s is scaling factor of the free-end amplitude $\vartheta(L) = \vartheta_L$. Using Rayleigh's method, the approximate expression for the mode shape and natural frequency is obtained as [85] :

$$X(x) = \left(\frac{L - x}{L}\right)^3 - 3\left(\frac{L - x}{L}\right) + 2. \tag{2—41}$$

By measuring the deflection $\vartheta(L)$ at the free end of the cantilever and evaluating $X(L)$ the value of λ_s can be determined. Thus the equation (2—38), the curvature along the x direction can then be written as:

$$\kappa(x) = \frac{6\lambda_s(L-x)}{L^3\left(1+\left(\frac{3}{L}-\frac{3(L-x)^2}{L^3}\right)^2 {\lambda_s}^2\right)^{3/2}}. \quad (2—42)$$

An approximation of the curvature value with an assumption that the slope is small compared with unity, so that it can be simplified as:

$$\kappa(x) \approx \vartheta''(x) \quad (2—43)$$

which gives a linear function of x:

$$\kappa(x) \approx \frac{6\lambda(L-x)}{L^3}. \quad (2—44)$$

Using the above simplification, the axial stress distribution over the beam can be written as:

$$\sigma_{xx}(x,y) = \frac{6Ew\lambda_s(L-x)}{2L^3}\left(\frac{2y}{w}\right) \quad (2—45)$$

or:

$$\sigma_{xx}(x,y) = \frac{3Ew\vartheta_L}{2L^2}\left(1-\frac{x}{L}\right)\left(\frac{2y}{w}\right). \quad (2—46)$$

From the above equation it can be seen that the stress achieves its maximum when $x = 0$ and $y = w/2$. The maximum stress can be written as:

$$Max\big(\sigma_{xx}(x,y)\big) = \sigma_m = \frac{3Ew\vartheta_L}{2L^2}. \quad (2—47)$$

During the experiments to break the cantilever beam samples, the load increased gradually to excessive stress/strain until the structure failed which meant that ϑ_L also gradually increased and thus was not constant. Hence, the maximum stress that might occur on the sample can be written as:

$$\sigma_m = \sigma_m(\vartheta_L) \quad (2—48)$$

Accordingly, the distributed stress magnitudes will also be a function of ϑ_L and can be written as:

$$\sigma_{xx} = \sigma_{xx}(x,y,\vartheta_L). \quad (2—49)$$

For most of the calculation in this chapter, the maximum deflection ϑ_L of the cantilever beam is assumed as a constant for simplification.

2.4.4. Volumetric probability of failure of the structure: model

For a structure of a uniform cross section and homogenous material subjected to a tensile force at both ends, the structure will be subjected to a uniform uniaxial stress distribution [86]. Its Weibull failure cumulative distribution function can be described using equation (2—26) by taking the stress distribution over the structure $\sigma_{ij}(p)$ to a uniform stress distribution σ. Thus such equation can be rewritten as:

$$f(\sigma) = 1 - \exp\left[-\int_0^V \frac{1}{V_0}\left(\frac{\sigma}{\sigma_0}\right)^m dV\right] \quad (2—50)$$

For the cantilever beam structures in use in this experiment, the stress, which is assumed mainly as an uniaxial stress, is non-uniformly distributed over the structure that the term $\sigma_{ij}(p)$ in equation (2—26) to become $\sigma_{xx} = \sigma_{xx}(x, y, \vartheta_L)$ and can be rewritten from the earlier equation as:

$$\sigma_{xx}(x, y, \vartheta_L) = 2\big(\sigma_m(\vartheta_L)\big)\left(1 - \frac{x}{L}\right)\left(\frac{y}{W}\right). \quad (2—51)$$

The volumetric failure probability as shown in equation (2—26) can also be written in the form of flexural stress distribution as:

$$f(\sigma_{xx}) = 1 - \exp\left[-\int_0^V \frac{1}{V_0}\left(\frac{\sigma_{xx}(x, y, \vartheta_L)}{\sigma_0}\right)^m dV\right] \quad (2—52)$$

and by taking the integration to their axes:

$$f(\sigma_{xx}) = 1 - \exp\left[-\int_0^H \int_{-\frac{W}{2}}^{\frac{W}{2}} \int_0^L \frac{1}{V_0}\left(\frac{2\big(\sigma_m(\vartheta_L)\big)\left(1 - \frac{x}{L}\right)\left(\frac{y}{W}\right)}{\sigma_0}\right)^m dx\,dy\,dz\right]. \quad (2—53)$$

Thus, after took the integration in place, the failure probability of whole structure gives:

$$f = 1 - \exp\left[-\frac{1}{2(m+1)^2}\left(\frac{LWH}{V_0}\right)\left(\frac{\sigma_m(\vartheta_L)}{\sigma_0}\right)^m\right]. \quad (2—54)$$

From the above equation it can be seen, if compared to the uniaxial stress tensile with uniform stress distribution, the cantilever beam is stronger by a factor of $2(m+1)^2$ from the integration of equation (2—50) below,

$$f = 1 - \exp\left[-\left(\frac{V}{V_0}\right)\left(\frac{\sigma}{\sigma_0}\right)^m\right]. \quad (2—55)$$

Due to the existence of the concentrated stress, the volume at or near the maximum stress is much less compared with the uniform stress distribution case.

2.4.5. Surface area probability of failure of the structure: model

Considering the early assumption that the structure failure always started from the surface and that the material volume effectively has no mechanical defect [21], area consideration will be made rather than volume.

Referring to Figure 2—3 that for in-plane vibration having y direction of motion, there will be two types of stress distribution surface, the upper and lower surface, and the side surfaces. The stress distribution of the upper and lower surface are affected by the fibre position of interest parallel to the neutral axis by a factor of $\left({}^{y}/_{W}\right)$ whilst the other surfaces lied on the outermost position about the neutral axis that their stress distribution is only depends on x. Thus we have upper and lower surface area failure function ψ_U and the side surface area failure function ψ_S. Then the failure probability of the structure can be recomposed from equation (2—27) to:

$$f = 1 - \exp\left\{-2\int_{A_U} \psi_U dA_U - 2\int_{A_S} \psi_S dA_S\right\}. \quad (2—56)$$

In this experiment case, surface properties, i.e. the surface roughness due to the different fabrication processes was considered. The upper and lower surfaces were mechanically polished and the side surfaces were DRIE. Therefore each type of surface has different Weibull parameters, the modulus m and the characteristic strength σ_0. The upper-lower surface was U indexed and the side surface was S indexed. Thus the failure functions for both terms of equation (2—56) can be detailed as:

$$\int_{A_U} \psi_U dA_U = \int_{-\frac{W}{2}}^{\frac{W}{2}} \int_0^L \frac{1}{A_{0_U}} \left(\frac{2(\sigma_m(\vartheta_L)) \left(1 - \frac{x}{L}\right) \left(\frac{y}{W}\right)}{\sigma_{0_U}} \right)^{m_U} dxdy \tag{2—57}$$

and,

$$\int_{A_S} \psi_S dA_S = \int_0^H \int_0^L \frac{1}{A_{0_S}} \left(\frac{2(\sigma_m(\vartheta_L)) \left(1 - \frac{x}{L}\right)}{\sigma_{0_S}} \right)^{m_S} dxdz. \tag{2—58}$$

2.4.6. Location probability of failure of the structure: model

A failure location probability [54, 58] of a particular test condition having a particular maximum stress σ_m is discussed in this section. By incorporating the earlier derived equation which describes the spatial distribution of the uniaxial stress along the cantilever beam, it can be seen that magnitude of the internal stresses vary due to its position parallel to the neutral axis and its position along the cantilever beam $\sigma_{xx} = \sigma_{xx}(x, y)$. The stress distribution can be rewritten from equation (2—51) in term of its maximum value as:

$$\sigma_{xx}(x, y) = 2\sigma_m \left(1 - \frac{x}{L}\right) \left(\frac{y}{W}\right). \tag{2—59}$$

Considering the above stress distribution into the probability of the structure to withstand the load r, the probability of the infinite volume described earlier in equation (2—32) can then be written as:

$$d\delta f^\circ = r(\sigma_{xx}(x, y)) d(\delta f)_{\sigma_m} \tag{2—60}$$

To solve the above equation, it was separated into two parts, $r(\sigma_{xx}(x, y))$ and $d(\delta f)_{\sigma_m}$.

For the first part $r(\sigma_{xx}(x, y))$, consider equation (2—22) which shows that an element volume of dV can withstand a load as described by:

$$r(\sigma_{xx}(x, y)) = \exp\left[-\int_V \psi(\sigma_{xx}(x, y)) dV \right]. \tag{2—61}$$

Specifically for the device structures used in this experiment, the above equation can be detailed with integration limits of:

$$r(\sigma_{xx}(x,y)) = \exp\left[-\int_{0}^{H}\int_{-\frac{W}{2}}^{\frac{W}{2}}\int_{0}^{L}\psi\big(\sigma_{xx}(x,y)\big)\,dxdydz\right]. \qquad (2\text{—}62)$$

By considering the failure function ψ of the above equation to have such a stress distribution $(\sigma_{xx}(x,y))$ as shown in equation (2—59), thus it can be written as:

$$\psi(\sigma_{xx}(x,y)) = \frac{1}{V_0}\left[\frac{2\sigma_m\left(\frac{y}{w}\right)\left(1-\frac{x}{L}\right)}{\sigma_0}\right]. \qquad (2\text{—}63)$$

Then after integrating the equation (2—62) over the entire cantilever beam, we get the probability of the structure to withstand r in terms of the structure geometry and under a Weibull term of distribution as:

$$r(\sigma_{xx}(x,y)) = \exp\left[-\frac{1}{2(m+1)^2}\left(\frac{LWH}{V_0}\right)\left(\frac{\sigma_m}{\sigma_0}\right)^m\right]. \qquad (2\text{—}64)$$

For the second part $d(\delta f)_{\sigma_m}$, by considering the probability of failure δf of the element δV in a stress condition near σ_m , then equation (2—31) can be rewritten as:

$$d(\delta f)_{\sigma_m} = \frac{\partial\psi(\sigma_{xx}(x,y))}{\partial\sigma_m}\,d\sigma_m\,\delta V. \qquad (2\text{—}65)$$

By incorporating equation (2—63) into equation (2—65) and partially differentiate the failure function over σ_m using a package software Mathematica® from Wolfram® we get:

$$d(\delta f)_{\sigma_m} = \left(\frac{2m}{\sigma_0}\right)\left(2\frac{\sigma_m}{\sigma_0}\right)^{m-1}\left(\frac{y}{W}\right)^m\frac{\big(F(x)\big)^m}{V_0}\,d\sigma_m\,\delta V. \qquad (2\text{—}66)$$

By recomposing the first part, equation (2—64), and the second part, (equation (2—66) into equation (2—60), the probability that the element will fail because of the internal stress is:

$$d(\delta f^\circ) = \qquad (2\text{—}67)$$

$$\exp\left[-\frac{1}{2(m+1)^2}\left(\frac{LWH}{V_0}\right)\left(\frac{\sigma_m}{\sigma_0}\right)^m\right]$$

$$\times \left(\frac{2m}{\sigma_0}\right)\left(2\,\frac{\sigma_m}{\sigma_0}\right)^{m-1}\left(\frac{y}{W}\right)^{m}\left(F(x)\right)^{m} d\sigma_m\,\frac{\delta V}{V_0}.$$

Integrating the above equation about σ_m gives:

$$\delta f^{\circ} = 2^{m+1}(m+1)^2\left\{1-\exp\left[-\frac{1}{2(m+1)^2}\left(\frac{LWH}{V_0}\right)\left(\frac{\sigma_m}{\sigma_0}\right)^{m}\right]\right\} \tag{2—68}$$

$$\times\left(\frac{y}{w}\right)^{m} F^{m}(x)\left(\frac{\delta x\delta y\delta z}{LWH}\right).$$

by integrating the above result about the cross section gives:

$$\delta f^{\circ} = (m+1)F^{m}(x)\left\{1-\exp\left[-\frac{1}{2(m+1)^2}\left(\frac{LWH}{V_0}\right)\left(\frac{\sigma_m}{\sigma_0}\right)^{m}\right]\right\}\frac{\delta x}{L} \tag{2—69}$$

and

$$\delta f^{\circ} = (m+1)F^{m}(x)\frac{\delta x}{L} \tag{2—70}$$

it can be seen as a probabilistic failure location density, q, given by:

$$q = \frac{\delta f^{\circ}}{\delta\left({}^{x}/_{L}\right)} = (m+1)F^{m}(x). \tag{2—71}$$

The failure position probability density can be seen in figure 2—4.

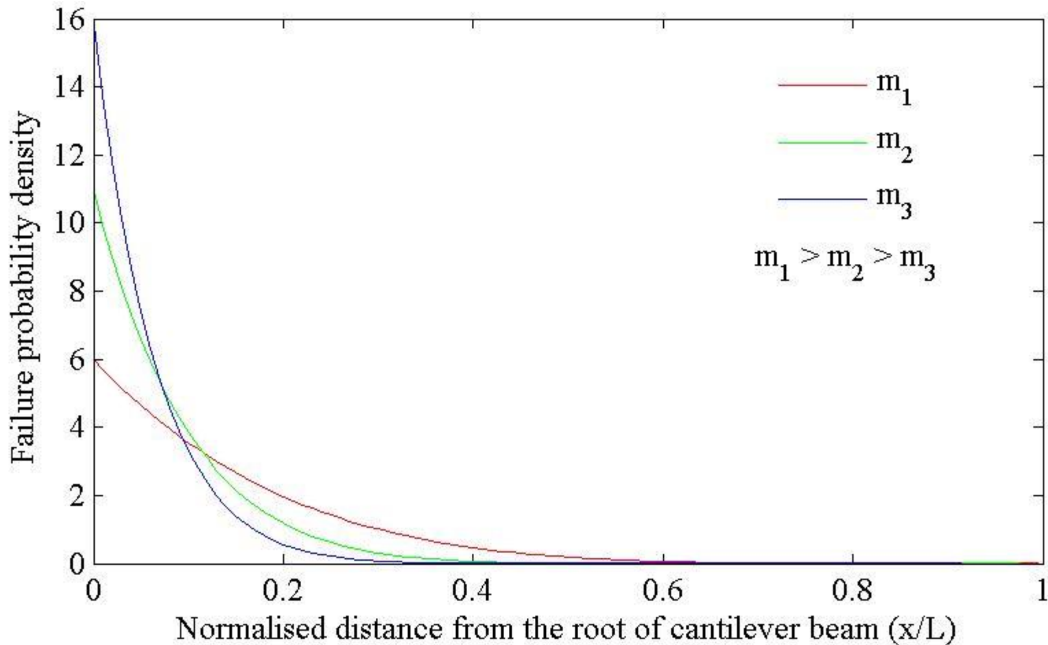

Figure 2—4: Failure location probability density

2.5. Weibull Parameters Determination

Another assumption has to be taken here. Extractions of the Weibull parameters were taken from fracture test under dynamic load during either first in-plane or the first out-of-plane resonance. During in-plane fracture, it was assumed that the failure only initialised from the side DRIE surface. Thus the fracture data from these tests were extracted to determine the Weibull parameters of such surfaces. Likewise for the fracture test during the out-of-plane vibrations, the data extracted was used to determine the Weibull parameters of the polished surfaces. By imposing this assumption, the influence of the other surface probability to fail can be neglected.

Maximum Likelihood Estimator was used to obtain the Weibull parameter from the fracture data as recommended in ASTM Standard C 1239-07, Standard practice for reporting uniaxial strength data and estimating Weibull distribution parameters for advanced ceramics [82]. The estimator equation is given as follows:

$$\frac{\sum_{i=1}^{N}\left(\sigma_{u_i}\right)^m \ln(\sigma_i)}{\sum_{i=1}^{N}\left(\sigma_{u_i}\right)^m} - \frac{1}{r}\sum_{i=1}^{N}\ln\left(\sigma_{u_i}\right) - \frac{1}{m} = 0 \qquad (2—72)$$

and,

$$\sigma_0 = \left[\left(\sum_{i=1}^{N}\left(\sigma_{u_i}\right)^m\right)\frac{1}{r}\right]^{1/m} \qquad (2—73)$$

where r is number of failed test specimens from a particular group of a censored sample. There was no censoring required during the fracture test implemented in this experiment thus r is replaced by the number of the samples N in the equation 2—70 and 2—71. Equation 2—70 is solved first to obtain the scale parameter m and then equation 2—71 to determine σ_θ. The expression in equation 2—70 require a numerical calculation. Practically, the Weibull parameters determination was done using the statistical software Minitab® available at Newcastle University.

The above procedure delivered characteristic strength of failure σ_θ and the Weibull modulus m. This characteristic strength still represents the geometry of the sample and stress gradient. Thus for utilisation in this work, that the parameter were used to predict the reliability or can also said the to predict the failure of different size geometry, the σ_θ was converted to Weibull material scale parameter σ_θ . For a uniformly distributed stress

in tensile fracture test with volume failure consideration, the relation between the parameters is given as follows [82]:

$$(\sigma_0)_V = (V)^{\frac{1}{mV}}(\sigma_\theta)_V \tag{2—74}$$

derived by equating the expression of Weibull failure distribution for uniform uniaxial stress load condition equation (2—23) and Weibull failure distribution under the same condition having a volumetric consideration equation (2—50).

Similarly, for a cantilever beam having flexural stress distribution, the relation between the two parameters may be by equating the equation (2—23) with equation (2—56), the failure probability of a cantilever beam with mechanically polished and DRIE surfaces area consideration. Thus the relation between the parameters can be describes in simplified forms as:

$$(\sigma_0)_U = k_U(\sigma_\theta)_U \; ; \; (\sigma_0)_S = k_S(\sigma_\theta)_S \tag{2—75}$$

where the subscript U and S represents the surface consideration of mechanically polished surfaces and DRIE surfaces respectively. The relation between the parameters is determined by a constant k which is unique about the structure geometry/size and its load condition at the surface.

Chapter 3. Equipment and fabrication

This chapter describes the fabrication of tests samples, equipment setup and test procedures. The samples fabrication include mechanical cutting for the flexural silicon bar and microfabrication processes for the micro cantilevers devices. The equipment setups consist of a four-point bending machine, vacuum chamber and piezo-actuator, surface profiler, laser vibrometer, static Raman system, dynamic Raman system and SEM imaging. Also included in the equipment setup description are an overview of test procedures on curvature measurement under the surface profiler, frequency calibration on the Raman system, frequency response measurement under the laser vibrometer, strain measurements under the static Raman system, strain measurement under the dynamic Raman system, in-plane fracture test, out-of-plane fracture test and the data gathering processes.

3.1. Devices fabrication

3.1.1. Material consideration: Silicon wafers

Most of MEMS devices are fabricated from (100) or (111) cut silicon wafers. Figure 3—1 shows a typical form of a silicon wafers cut with a (110) plane primary flat. The cantilever beams in this experiment were fabricated along the [110] direction.

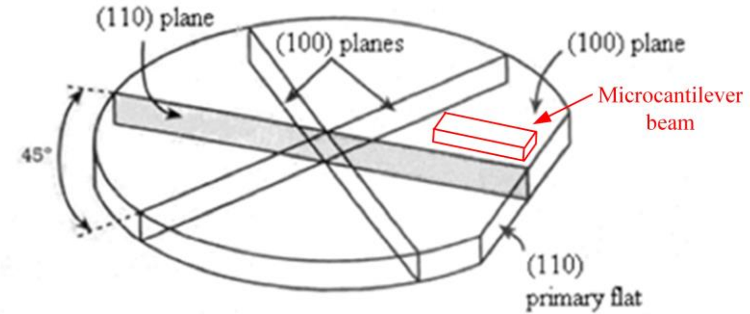

Figure 3—1: An illustration of a microcantilever beam longitudinal orientation fabricated along the [110] crystallographic direction. Picture is not scaled

The wafers are also doped to have p-type mobility charge carrier in the silicon yet the silicon purity still remains very close to 100% so that it can still be expected there is no mechanical effect due to the doping. The properties and tolerance of the SOI wafer used in this work can be seen in table 3—1.

Table 3—1: SOI wafer properties

Manufacturer	Ultrasil Corporation, Hayward, California
Device Layer:	
Diameter:	150 ± 0.2mm
Type/Dopant:	P/Boron
Orientation:	<100> ± 0.5 degree
Thickness:	15 ± 1µm
Resistivity:	0.01-0.02 Ohm cm
Flats:	Semi std 1
Finish:	Polished
Buried Thermal Oxide:	
Thickness:	2µm ± 5%
Handle Wafers:	
Type/Dopant	P/Boron
Orientation	<100> ± 0.5 degree
Resistivity:	0.01-0.02 Ohm cm
Thickness:	500 ± 15µm
Finish:	Polished

There were two types of samples studied in this thesis. The first type is the microcantilever beam devices for dynamic characterisation that were fabricated under microfabrication processes and the second type is mechanically cut silicon bars from a wafer disk into small beams for static characterisation under four-point bending. The beams were also cut to have their longitudinal direction parallel with [110] direction. The same cutting direction of the silicon bars with the microcantilever beam is important as it were used to calibrate the Raman shift due to strain.

3.1.2. Microfabrication processes

The cantilever beam structures were fabricated having such crystal direction from a single crystalline silicon wafer. The samples will fit to the (001) Raman geometry so that only one Raman transition would be observed. The fracture tests being implemented with these samples were estimated to have amplitudes of motions of several microns so the die was designed to have enough space necessary for both in plane motions and out-of-plane motions. The handle silicon was also removed from the device location to facilitate the potentially large out-of-plane amplitude vibrations. The (100) silicon-on-insulator (SOI) wafers used to produce the microcantilever beam were composed of a 15μm device layer with 2μm sacrificial buried oxide (BOX) layer together with 500μm of handle silicon as shown in figure 3—2:

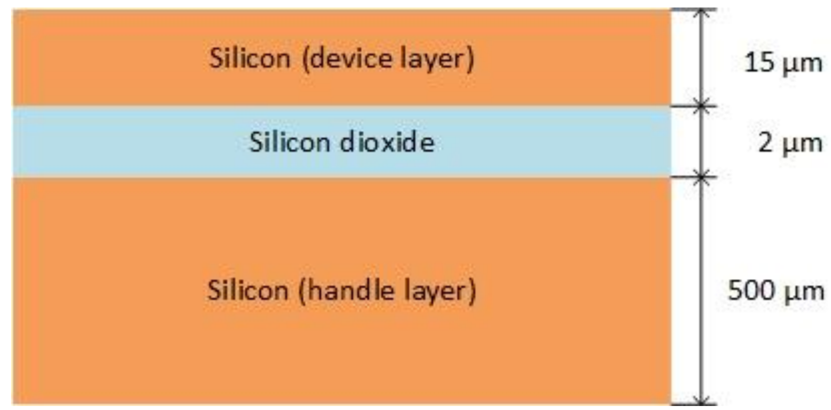

Figure 3—2: SOI wafer layers

The fabrication of the device was performed by Barry Dunne at the INEX facility within Newcastle University using a STS Advanced Silicon ICP Etcher having an etch rate of 5µm to 8µm per minute.

In photolithography process, a photomask is laid on a light sensitive photoresist coated on a silicon wafer. The geometric pattern of the device was put on such a photomask having opaque and transparent areas. Under ultraviolet light, the shined region of the photoresist chemically change. Using positive photoresist processing type, the protected region (unexposed from the light) of the photoresist remain on the wafer. The process then followed with etching process to remove the clear regions on the wafer while opaque regions of the mask remain as oxide.

Plasma etching process is done by directing a high stream plasma pulse of gas mixture to the wafer. The plasma source (also known as etch species) can be either charged (ion) or neutral (atoms and radicals). Volatile etch products were created as a result of reaction between neutral particles with the wafer surface. The products then can be removed using vacuum pump. The same effect can also be produced using ions which can produce sputtering effect removing materials by direct bombardment. Various gases containing small molecules rich in chlorine and fluorine may act as an etch species. They are for example, CF_4 and SF_6 for silicon etching, a mixture of CF_4/H_2 for silicon dioxide etching, a mixture of CF_4/O_2 for silicon nitride etching [87]. Deep, steep-sided with high precision features can be produced using DRIE (deep reactive ion etching). A side effect of plasma etching is the creation and deposition of polymers from the etchant that may be exploited. Bosch developed a DRIE process that proceeds in alternating steps of; a standard reactive ion etch in a SF_6 plasma and; polymer deposition from a C_4F_8 plasma.

The reactive ion etch rapidly removes the polymer at the bottom of the feature, but the polymer on the sidewall stay in place longer. Thus, the top of the feature does not become

wider as the sidewalls remain protected by the deposited polymer. During the process, the sidewall polymer is eventually eroded that the polymer deposition step should be repeated. Based on this behaviour, a large number of very small etch step having a very small effect on the sidewall is possible through repeating process of the etch and deposit step in many times. Table 3—2 summaries the process.

Table 3—2: Microfabrication process summary

Step No.	Process Description	Wafer Cross-Section	Mask Required	Comments
1.	Issue Silicon-On-Insulator (SOI) wafer			500 μm handle, 2 μm BOX and 15 μm device silicon thicknesses.
2.	Deposit hard mask layer on handle side			Used later as mask for deep reactive ion etching (DRIE) of handle silicon
3.	Photolithography for DRIE etch		Backside mask on handle layer	Positive photo-resist
4.	Plasma etch hard mask			Use end-point system to determine etch time
5.	Wet & dry removal of remaining photo-resist			Turned upside down
6.	Photolithography of device side silicon pattern		Topside mask on device layer	Photoresist used to define the beams

7.	DRIE of device side silicon, stopping on BOX layer			Short DRIE etch process used to cut through the device layer
8.	Protection layer			To assist with protecting the cantilevers during the DRIE of the handle layer silicon
9.	Wafer bond			Temporary bond to a backing wafer to assist with the DRIE etch process of the handle silicon
10.	DRIE Handle silicon layer			Stopping on BOX layer This also defines each chip at this point. Turned upside down.
11.	Plasma etch BOX layer			This frees the cantilevers at this point which are supported by the protective resist layer
12.	Solvent release of die from backing wafer			Also has a plasma clean once die are removed from solvent. Finished die are ready. Turned upside down.

3.1.3. Microfabricated devices

The microcantilever beams with end mass were fabricated on a SOI wafer and then cut into multiple 10mm square dies. The dies contain a variety of microcantilever beams geometries and sizes as shown in figure 3—3. Some devices are identical in design but may be different due to the fabrication processes. Devices that have identical design are: all in the group E and L, group J and H, A1 and R2 and K12, A2 and R1 and K13, B1 and Q2 and K3, B2 and Q1 and K4, C1 and P2 and H12, C2 and P1 and H13, D1 and N2

and H3, D2 and N1 and H4. The variations on a die were intended to give different resonance frequencies between the different designs of microcantilever that actuation of a particular microcantilever can be selected by actuating in such resonance frequency.

Microcantilevers on the edges of the dies were used for in-plane motion characterisation as the position enables the incident light beam to reach the side surface of the beam. According to the nomenclature of the devices as shown in figure 3—2, A, B, C, D, N, P, Q and R are enabled for in-plane characterisation.

Group H, J, K and M have a symmetrical design. Group E, G and L have an asymmetrical design. Group F is a clamped-clamped end beam that is unused in this experiment. The asymmetrical design of end mass was intended to have a twisting effect during the vibration. This twist effect was also excluded from this work.

The cantilever beams in the group E, G, H, J and L were designed as a rectangular beam having a rectangular end mass. For every group there are 4 sub-groups sizes. There are also variations of the cantilever beam length within the sub-group having sequential differences of 10μm differences. There are two size variations of size of the clamped end width of 20 μm for beams on the left hand side and 10 μm for the right hand side.

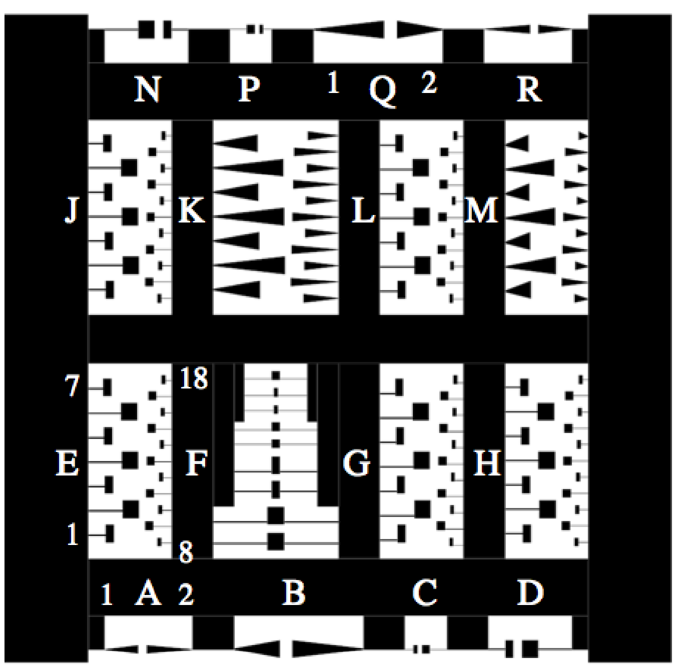

Figure 3—3: Beams nomenclature within a dies

The K and M group are triangular design cantilever beams. These groups were also designed to have a sequentially 10μm of length differences for every sub-group. The length of the beams in group K varies from 860 μm down to 370 μm whilst in group M

varies from 610 μm down to 120 μm. As with the earlier mentioned groups, there are also two size variations of size of the clamped end width of 20 μm for beams on the left hand side and 10 μm for the right hand side.

This work only used the microcantilever beams from group H and J which are rectangular design having uniform cross sectional area and symmetrical end mass. The choice on using these groups was made that stress gradient along a rectangular design beam is more gradual being compared to a triangular design of the beam whilst the choice of symmetrical end mass was to avoid possibility of beam twisting during either in-plane or out-of-plane motion. The rest design geometry available in the dies were intended to be used for different researches within Newcastle University MEMS research group.

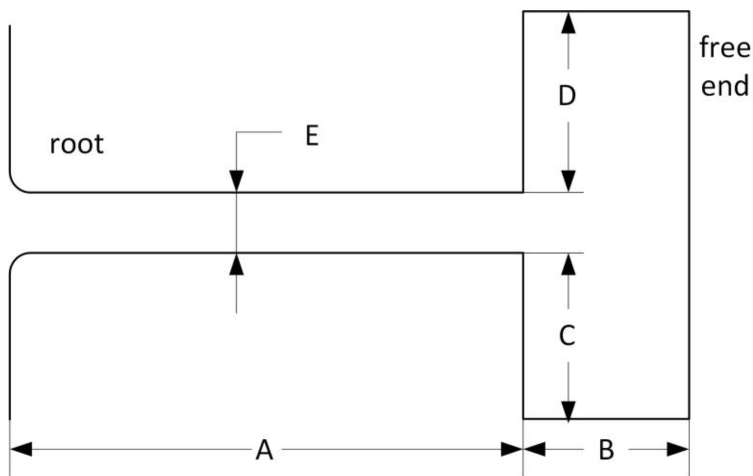

Figure 3—4: Device dimensions (see table 3—2 for a particular device)

Table 3—3: Devices with symmetrical rectangular end mass, J = H

No	A	B	C	D	E
J01/H01	210	100	100	100	20
J03/H03	200	100	100	100	20
J05/H05	190	100	100	100	20
J07/H07	180	100	100	100	20
J02/H02	410	200	100	100	20
J04/H04	400	200	100	100	20
J06/H06	390	200	100	100	20
J08/H08	120	50	50	50	10
J10/H10	110	50	50	50	10
J12/H12	100	50	50	50	10
J14/H14	90	50	50	50	10
J16/H16	80	50	50	50	10
J18/H18	70	50	50	50	10
J09/H09	220	100	50	50	10
J11/H11	210	100	50	50	10

J13/H13	200	100	50	50	10
J15/H15	190	100	50	50	10
J17/H17	180	100	50	50	10

Figure 3—4 shows the feature size of J/H devices where A, B, C, D and E denote for the length of cantilever beam, the length of the end mass, left width of the end mass, right width of the end mass and the width of the cantilever beam respectively.

3.1.4. Mechanically cut silicon beams

Silicon beams for static characterisation under the four-point bending were diced mechanically using a diamond tip cutter from a SOI disk into 2mm width and 10mm length with the thickness of about 520 microns. The beams were used to calibrate the Raman peak shift being compared to the strain calculated from measured beam curvature. These beams were not intended for fracture test as the diced faces (side surfaces cut) of the bar were very rough being compared to the mechanically polished topside.

3.2. Equipment and characterisation procedure

3.2.1. Four point bending

The four-point bending machined was used to bend the silicon bar. The force applied to the bar (Figure 3—5) was generated by four parallel springs. The springs are positioned on the corner of the machine and retracted by tightening their screw-nut holders.

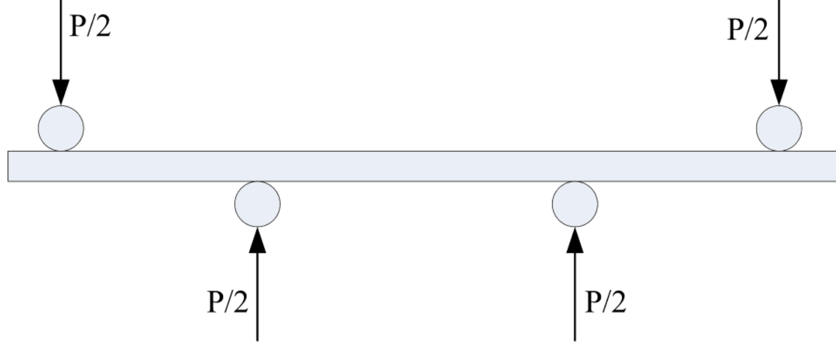

Figure 3—5: A silicon bar loaded under four-point bending

The bending machine was designed to allow either a Zygo profiler or the Raman setup objective lens to focus on the silicon bar surface. This machine was designed to hold and bend the silicon bar sized of 10mm x 2mm with about 520μm thickness as shown in figure 3—5. The machine itself doesn't have any capability of measurement. The radius of curvature was measured using the profiler and the induced strain was measured using Raman spectroscopy.

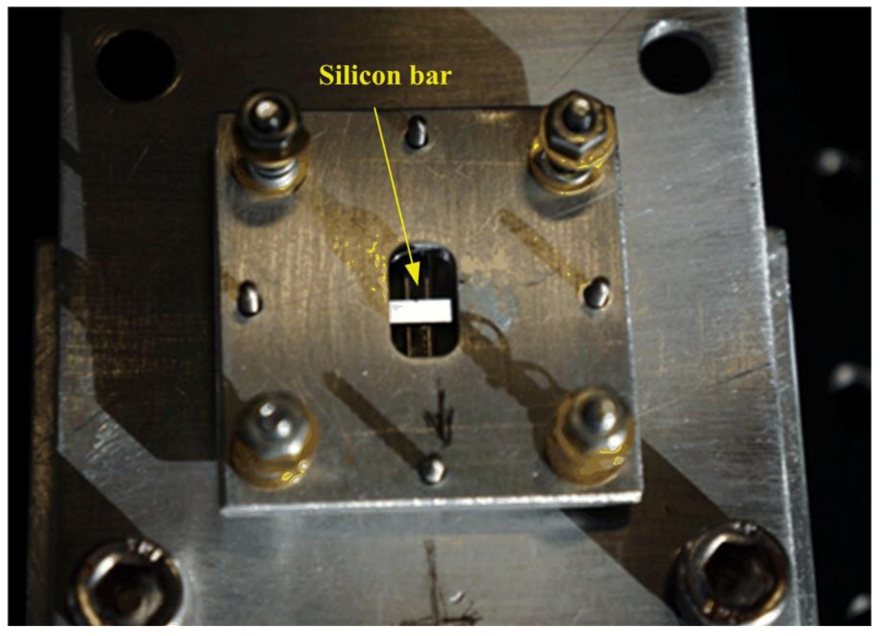

Figure 3—6: Four-point bending machine with a silicon bar loaded.

As the bending tests were performed using either the profiler or the Raman system, the test sample had to be transported from one piece of equipment to another. Theoretically, all area surfaces within the inner span will give a same response, but the measurements show a small variation both on the sample profile and the strain. Due to these observations, a point location was chosen on every test sample for reference location of measurements to assure data validity.

3.2.2. Vacuum chamber

Vibratory characterisation and dynamic Raman spectroscopy were done by placing the sample in vacuum chamber. The chamber was sealed with a screwed lid having a sight glass window. The lid rested on a nitrile O-ring attached to the chamber that gave the capability of being pumped down to approximately 2.8 mbar. The window was a 2 inch diameter and 3mm thick Edmund Optics glass with anti-reflection coating secured to a 33 mm diameter aperture with a nitrile O-ring.

3.2.2.1 Test setups

There were two setup types during the experiments. The first setup was used during vibratory characterisation. In this setup, the chamber was fixed horizontally to the motorised XY jig. The stage positioned the device of interest under the laser beam whilst the laser focus was done manually by raising or lowering the objective lens.

For the second type of setup for dynamic Raman characterisation, the chamber was fixed vertically to a manual XYZ micrometer jig. This kind of jig was used because the

laser position and the focus were fixed so that the jig had to be able to position the device surface at the focus of the laser beam.

3.2.3. Piezo-actuator and die mounting

The die was mounted on a piezo disk supplied by Morgan Matroc that allowed the in-plane and out-of-plane actuation of the cantilever beams. The actuation of the sample was made by supplying a sine wave signal to drive the piezo disk. The sine wave signal was generated from a signal generator and amplified using a TEGAM 2350 high voltage amplifier.

The piezo disk was glued between the metal test sample holder and the base using Rite-Lock SL65 Silver Loaded Epoxy Adhesive as can be seen from figure 3—7. The actuation motion was generated by supplying a sinusoidal voltage across the thickness of the piezo disk. The disk expands and contracts sinusoidally proportional to the supplied voltage.

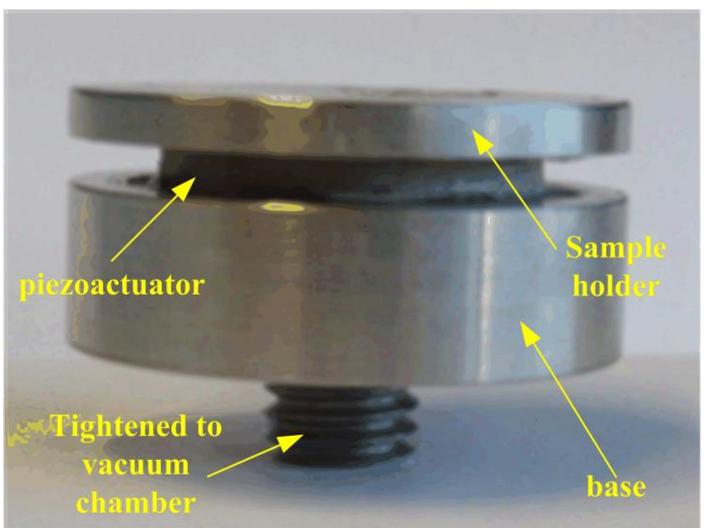

Figure 3—7: The piezoelectric actuator glued between two pieces of metal holder

The test piece was permanently glued to fix it in place with Bond Lok B2012 Epoxy on a glass slide to avoid a direct contact with the heated wax resin during attaching the test piece to the actuator as can be seen on figure 3—6. Utilisation of such heated wax resin was to make an easy dismantling of the dies from the actuator holder by heating the wax thus the samples which haven't tested still in safe condition due to smooth releasing process. Utilisation of the wax also make reattaching of the sample possible. The black mark under the slide glass is residual wax resin during the removal of the test piece from the holder by reheating the wax after fracture tests were completed.

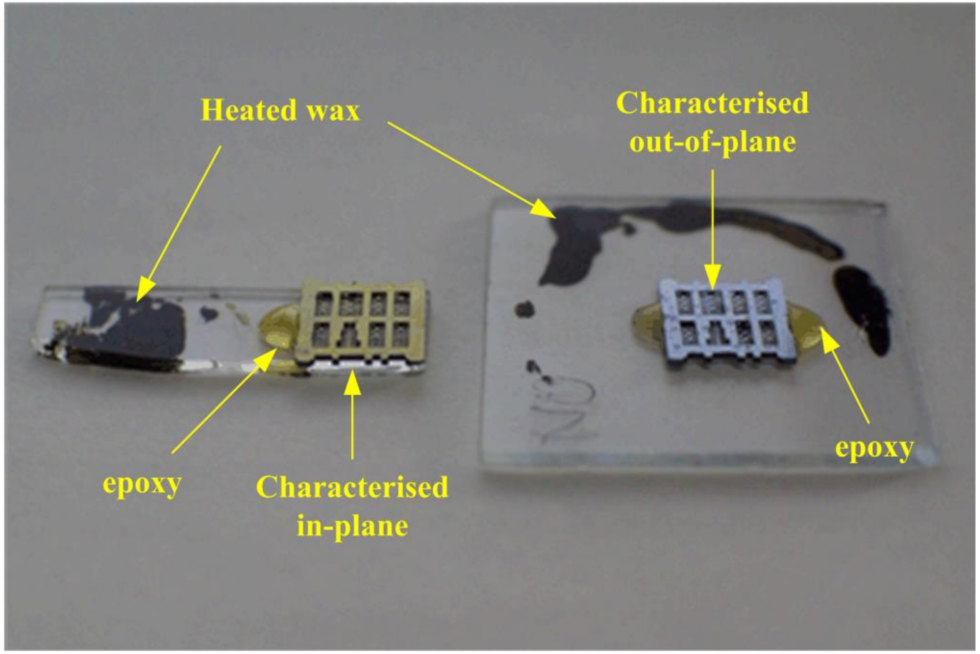

Figure 3—8: Dies fixed on glass slide.

Two types of die mounting were applied. Figure 3—6 shows the left side sample, prepared to enable the in-plane characterisation. The side glass base was made to have a smaller width compared to the dies width to enable the objective lens to come close to the sample edge. For this characterisation type, the dies have to be fixed to stand in an upright position. Also, only the devices located on the upper side of the die edge can be characterised; the remaining devices were unreachable by the light probe.

The right side sample that can be seen from the same figure was prepared for out-of-plane characterisation. In this configuration, the slide glass only needed to be placed on the holder surface and fixed using heated wax.

3.2.4. Surface profiler

The Zygo NewView 5000 surface profiler was used to characterise the surface profile of the samples and to measure the radius of curvature of the flexure during static bending in the four-point bending test.

This 3D non-contact profiler uses scanning white light interferometry to produce high-resolution images and measure the microstructure surface topography. The equipment is capable of height profiling from less than 1nm up to 5mm with scanning speed as fast as 10μm per second and has a vertical resolution of about 0.1nm.

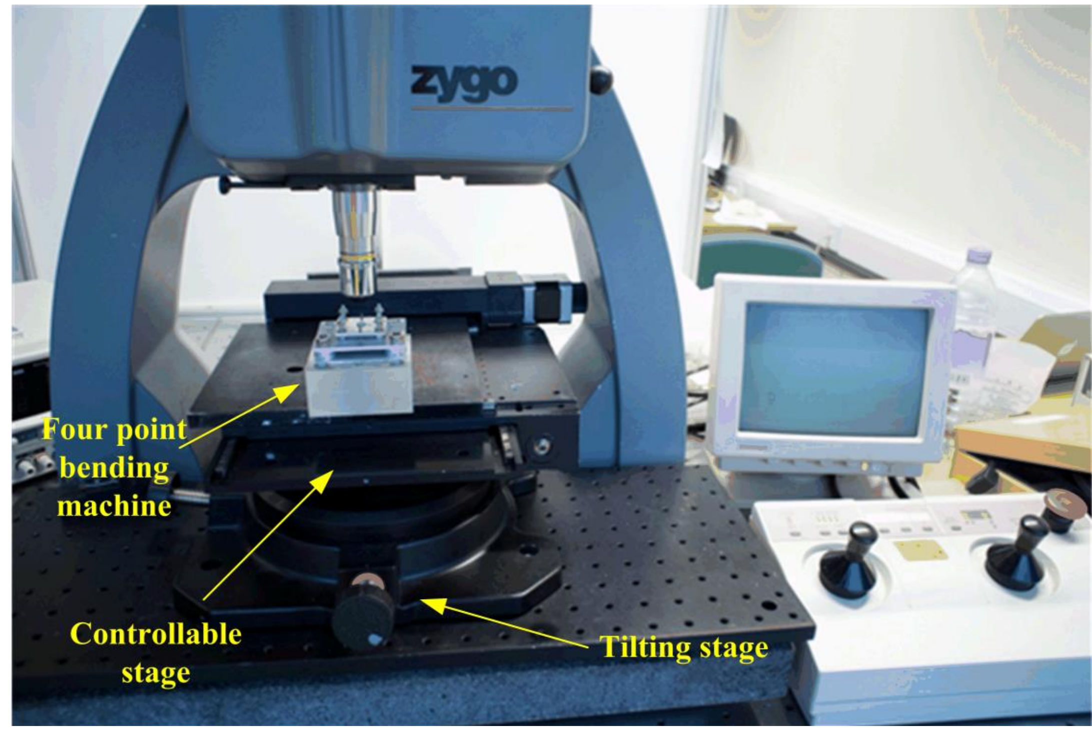

Figure 3—9: Four-point bending machine under the Zygo® profiler

This profiler setup, as shown in figure 3-7, is featured with a motorised XY table which sits on a manual-tilting stage to bring the sample in position, objective lenses were mounted on a five-position motorised turret. A six indexed variable image zoom is also available. The MetroPro® metrology software package was used to control the operation and interpret the data.

3.2.4.1 Curvature measurement

The curvature measurement was used together with the Raman static strain measurement to give a relation between calculated strains determined from measured curvature and the Raman peak shifts. This measurement was conducted under the Zygo profiler to measure the radius of curvature of the bent silicon bar using a function available in MetroPro, the $RadCrv$. The function gives a direct measure of the radius of measured curvature as can be seen in figure 3—8.

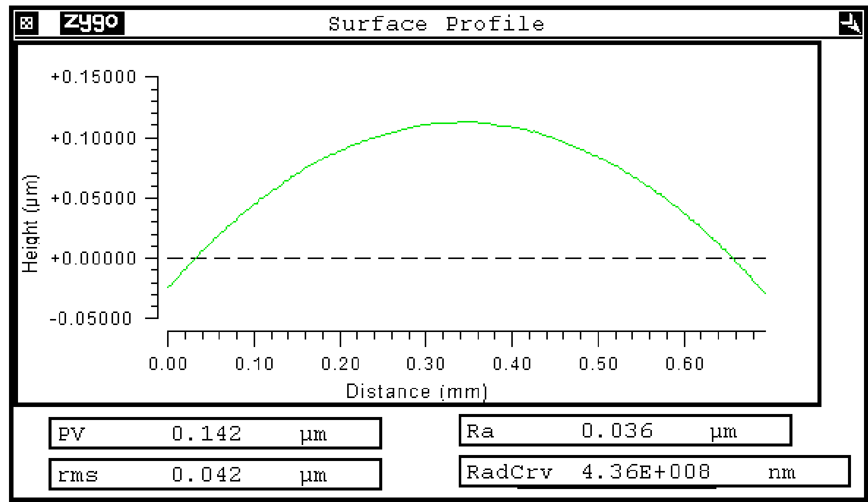

Figure 3—10: Radius of curvature measured using the Zygo® surface profiler.

$RadCrv$ function estimates the radius of curvature by calculating the distance from the part being measured to the centre of the curvature of the surface. The estimation can be seen as follows:

$$RadCrv = {s^2 + \left(\frac{d}{2}\right)^2} \Big/ {2s} \quad (3—1)$$

with sag(s), diameter(d), and radius of curvature($RadCrv$) as shown in figure 3—9. A positive value corresponds to a convex surface and a negative value corresponds to a concave surface.

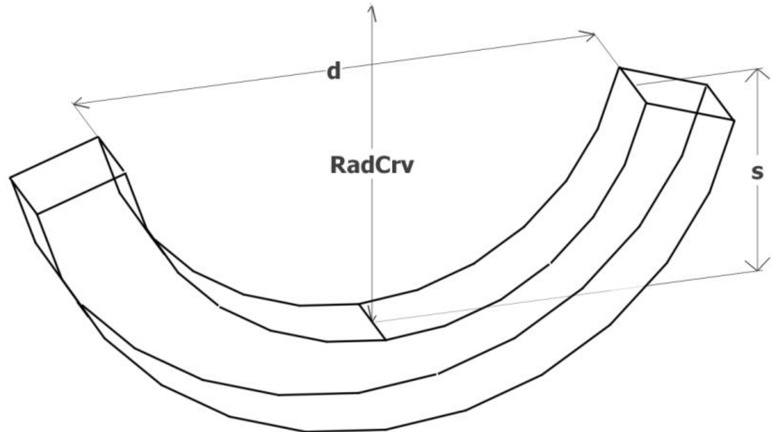

Figure 3—11: Radius of curvature determination

3.2.4.2 Surface roughness characterisation

There are two kinds of surface that can be found on the microfabricated devices. The mechanically polished surface and DRIE surface having a different surface roughness.

3.2.5. Laser Vibrometer

A Polytec laser vibrometer system was used for vibratory measurements in this experiment. The schematic instrument setup can be seen in Figure 3—12. The resonance frequencies of every device used in this work were characterised using this equipment. The frequencies recorded were later used to actuate the devices excessively to fail during fracture tests.

This vibrometer is equipped with the laser-Doppler vibrometer – a precision optical transducer, capable of measuring either vibration velocity or displacement at a fixed point. The unit works by sensing the frequency shift of back scattered light from a moving surface. The technique is known as 'the Doppler effect'. The laser vibrometer setup consisted of a Polytec® fibre optic interferometer and a Polytec® controller unit for the signal processing. A HP 3562A unit was also used in the setup as a signal analyser and actuation signal generator. The signal voltage and frequency range were set on this unit.

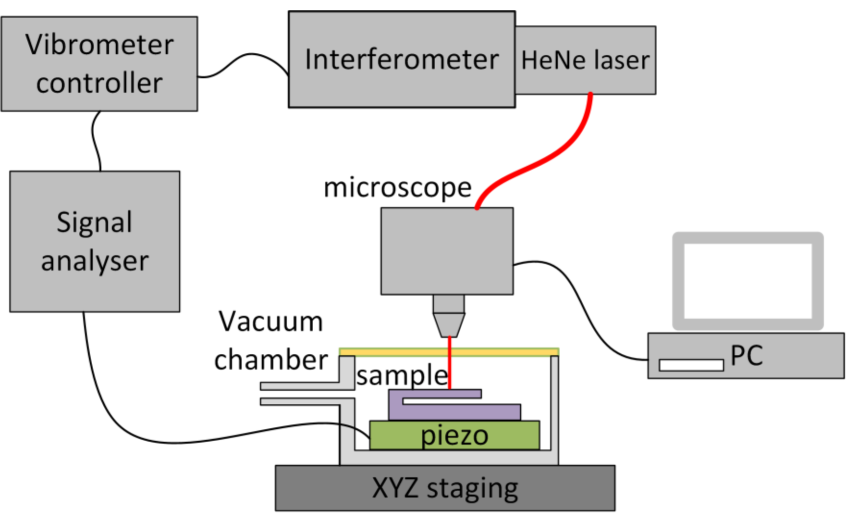

Figure 3—12: Schematic of laser vibrometer system

3.2.5.1 Signal analyser

Dynamic testing measurements in this experiment were made using a HP 3562A dual channel dynamic signal analyser that covers a frequency range of 64 μHz to 100 kHz. Channel 1 was used to excite the device under test at voltage of up to 5 V whilst channel 2 received the output signal from the laser vibrometer. The analyser used within the laboratory can be seen in figure 3—13.

Figure 3—13: HP 3562A signal analyser.

The analyser works by performing a Fast Fourier Transform (FFT). Calculation of a device frequency response function (FRF) begins by digitising the input at channel 1 by 256kHz sampling. This sample data then fills a data buffer and when the buffer is full, FFT of the data buffer calculates the frequency spectrum. The device frequency response is then calculated from the ratio of the cross spectrum to the power spectrum of channel 1. The schematic calculation of the frequency response function can be seen in Figure 3—14 where F_1 is the FFT of channel 1 signal, F_2^* is the complex conjugate of the FFT of the channel 2 signal, $F_1F_1^*$ and $F_1F_2^*$ are the direct and cross spectra respectively.

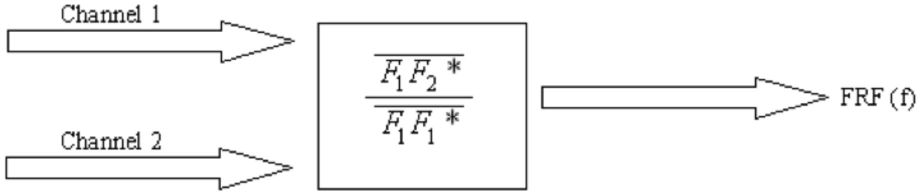

Figure 3—14: FRF from signal analyser working in linear resolution mode.

The device frequency response was measured under a Swept Sine operation mode. The unit generates a swept frequency sine wave with fixed amplitude to actuate the device through the range of interest. Then, the device response is processed as mentioned above to determine the FRF. The device response is displayed graphically by presenting the device response power spectrum of channel 2 or the FRF of the device under test.

3.2.5.2 Resonance frequency measurement

Before doing a fracture test, resonance frequencies of a device were determined for the actuation frequency reference. Ideally, the first in-plane and the first out-of-plane resonance frequency of the device can be easily measured using the laser vibrometer. However it is possible to characterise only in-plane or only out-of-plane resonance frequencies due to the limitation of the die fixing method. As mentioned earlier, the dies were fixed to the actuator holder using wax (the wax was melted using heated air) and it was highly likely that a change of orientation from vertical to horizontal or vice versa could damage the device. As the working principle of the equipment is using the Doppler effect, it should be noted that characterisation under this equipment should be performed for a motion having parallel direction with the laser beam. A motion purely perpendicular to the beam direction cannot be detected.

Considering these limitations, most of the devices were only characterised out-of-plane. Fortunately, this was not an issue during the fracture test in the vacuum chamber under the Raman setup, In-plane resonance frequency was easily recognised under visual observation by sweeping the actuation frequency within a range of the estimated resonance. The resonance frequencies for out-of-plane motions were performed with the vibrometer.

The resonance frequency characterisation was performed by actuating the device across a range of frequencies. In the analyser unit, the actuation signal was set to ‘Swept Sine’ to provide the sweep of actuation frequencies. The frequency range of the device was estimated beforehand using the finite element package ANSYS.

3.2.5.3 Frequency range limitation

Due to the limitation of the analyser being in used in this experiment, only a resonant frequency of 100 kHz or lower can be characterised. However, a higher resonance frequency can be characterised by visual observation.

3.2.5.4 Displacement amplitude measurement

The vibrometer is capable of either velocity or displacement measurement of the object. The displacement amplitude can be calculated from velocity measurement. For harmonic vibrations, the displacement amplitude $\tilde{x}$ is given by:

$$\tilde{x} = \frac{\tilde{v} V_R}{2\pi f} \qquad (3—2)$$

where $\tilde{v}$ is the measured velocity amplitude in volts, V_R the selected velocity range setting on the vibrometer controller and f the driving frequency. Available V_R values are 5, 25, 125 and 1000mm/second/Volt. Most of the measurements in this experiment used 125mm/sec/V or 1000mm/sec/V to give optimal resolution of displacement measurement.

3.2.5.5 Out-of-plane motion

The maximum displacement measurement utilising the visual observation mentioned earlier is only possible for the in-plane motion. While for the out-of-plane motion, due to the utilisation of HP 3562A signal analyser to interpret the signal from the laser vibrometer, the measurement was limited to only 100kHz.

For maximum displacement measurement, a particular procedure was used in which the laser spot was positioned to a selected position not at the far end of the cantilever beam. Then, the maximum displacement was estimated based on the displacement on such selected position. The advantages of this procedure is mainly to keep the laser spot in-focus and avoid an over-ranged V_R.

As the maximum displacement during the motion was only necessary to calibrate the dynamic Raman characterisation method used in this experiment, the out-of-plane strain/stress estimation also incorporated the in-plane calibration which was considered to be well calibrated.

3.2.6. Visual observation

3.2.6.1 Resonant characterisation

Visual observations to characterise resonant frequencies of the devices in this experiment were possible due to large displacement during vibration. However, only the in-plane motion is visible. The characterisation to recognise that a device was at its resonance can be seen from blurring of the image of the device on the microscope monitor.

3.2.6.2 Maximum displacement

The maximum displacement measurements were done visually by measuring the structure blurring edge during its vibrations as can be seen in Figure 3—15. The length calibration was made based on the actual known length of the structure feature and relating this with the measured width of the feature on the camera monitor. The maximum

displacement was determined by fixing a chosen feature edge with normal to the motion direction as the zero displacement reference and measured its distance to the edge of the blurring feature during the device motions. Using this method a resolution of 1 μm of length was achieved. The camera system incorporates a shared objective optical lens with the Raman system having magnification of 50X.

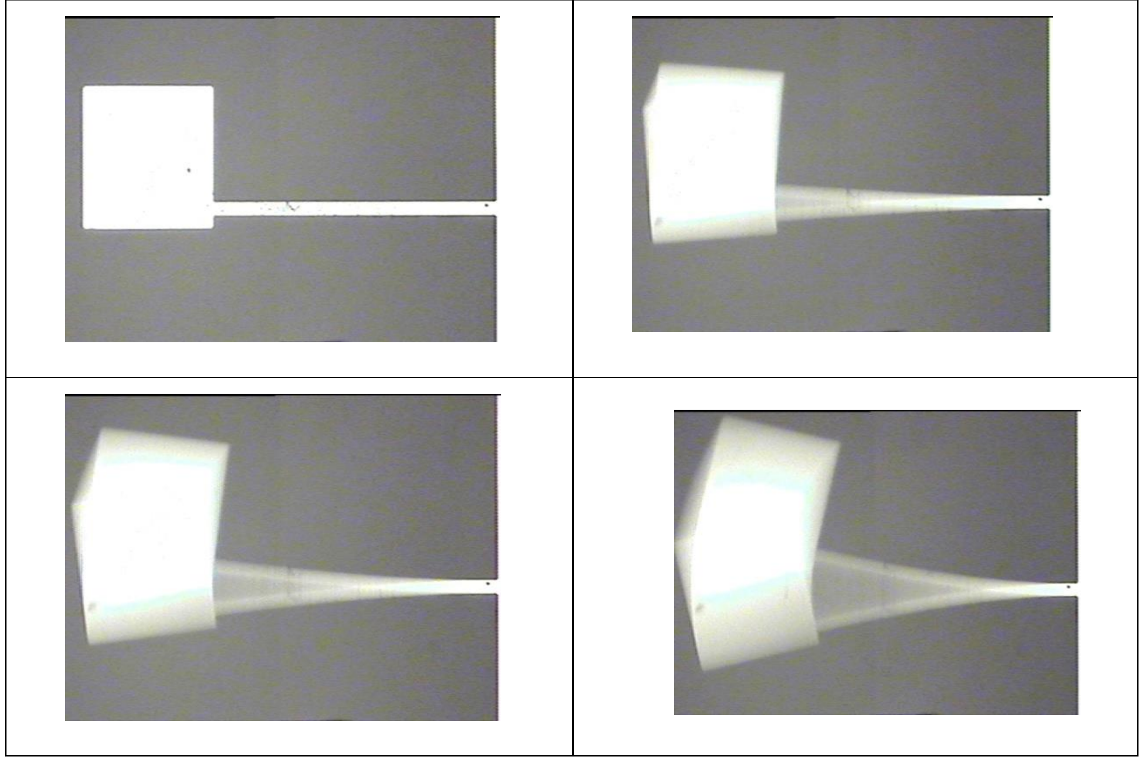

Figure 3—15: Maximum displacement measurements of in-plane motions.

3.2.7. Raman spectroscopy

Micro Raman spectroscopy was extensively used to measure strain in this experiment. To get a reliable strain measurement result, a calibration was necessary. A calibration was performed which relates the calculated strain from measured displacement or deformation with the Raman peak shift. Below is an overview of both the static and dynamic Raman characterisation procedure.

Figure 3—16 shows the schematic of the Raman system experimental setup. The setup consisted of a HR1000 Horiba Jobin Yvon Raman spectroscopy system coupled with a 632.8 nm HeNe laser source of 30mW, which was directed via two mirrors into the ‘super-head’ having an objective lens of 50× magnification. Having this setup, the laser spot diameter was approximated to 1 μm and the penetration depth of 3 μm. XYZ micro staging was used to position and focus the laser beam. The staging was used to carry either the four-point bending machine or the vacuum chamber. The scattered light was collected through the same lens back to the super-head and returned via an optic fibre

into a spectrometer. The Raman scattering signal then was detected using a CCD with liquid nitrogen cooling. Data signals were collected every 0.25 cm^{-1} thus there were 4 data point available for every 1 cm^{-1}. Further discussion on such data density is available in section 4.2.3.Instrument control and data processing were done under LabSpec® Spectroscopy Suite Software which came packaged with the Raman system.

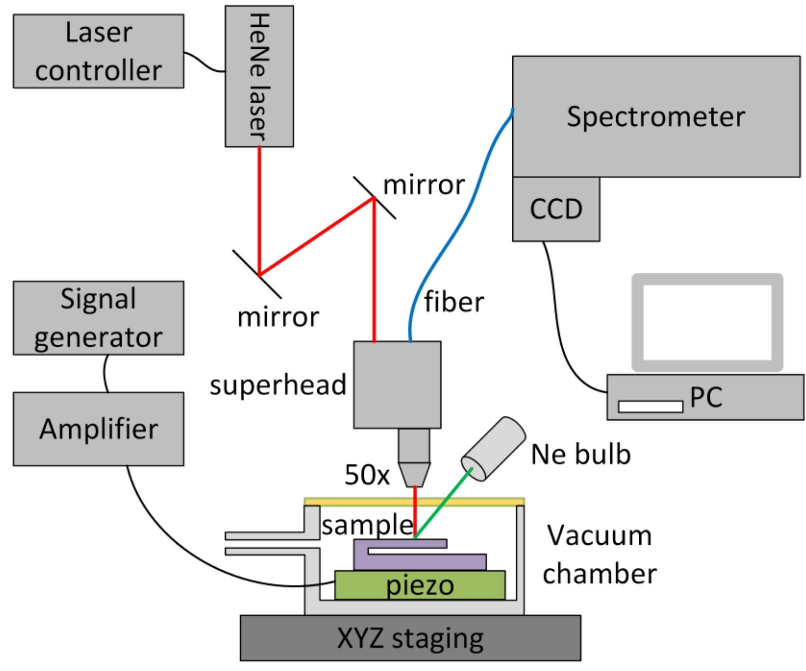

Figure 3—16: Schematic of Raman system

3.2.7.1 Laser alignment, position and laser spot diameter

Instead of using fiber-optics which was come with the Raman system package, the laser beam alignment between laser source and the super-head was done by incorporating two mirrors to get the smallest possible diameter of laser spot. The laser source, mirrors and the laser head were fixed on an optical table. The positions and the directions of the units were fine-tuned so that a visually measured laser spot diameter on the device of about 3μm was achieved.

3.2.7.2 Ne bulb reference

A calibration technique that makes use a Ne bulb as a reference was implemented in this experiment to overcome the continuous shifting of the peak frequency of silicon due to temperature drifts in the equipment. Frequency calibration is commonly done by measuring a single crystal silicon standard sample and calibrates further Raman readings with respect to this known value of the standard silicon peak. In this work, the light of a neon lamp was directed to the laser spot on the device being measured. The known

frequencies from neon are then automatically superimposed on any Raman scan and can be related to the silicon peak position. Using this technique, any error in the peak shift can be estimated continuously.

3.2.7.3 Static strain characterisation

Static strain characterisation was performed using the procedure discussed in section 3.2.4.1. The strain was calculated from the measured radius of curvature of the sample whilst the Raman peak shift was obtained by performing a measurement on the same sample with identical loading conditions between both Zygo profiler and the Raman system. A careful handling procedure was necessary as the sample was moved between the equipment to ensure that both measurements were taken under identical conditions.

3.2.7.4 Dynamic strain characterisation

Dynamic strain characterisation was performed on a dynamically loaded microcantilever beam loaded within a vacuum chamber. As the vibratory motions of interest were the first in-plane and the first out-of-plane mode, the dynamic strain characterisations were also performed under both conditions. The laser spot was positioned on the corner of the clamped end of the cantilever beam as the maximum strain was expected at this location.

3.2.7.5 Fracture strength characterisation

Either the fracture tests under in-plane or out-of-plane motions were characterised using Raman. The failure mechanism of a device was effectively instant, much faster than the measurement duration required by the Raman. Thus, the real fracture strength of a device, the maximum stress that brought the device to fail, was never really measured, yet the ‘one step before fail’ maximum stress was measured. Consequently, the fracture strength of a ruptured device was extrapolated based on the trend of stress and supply voltage increments relation. The trends were considered to be linear.

3.2.8. Scanning Electron Microscopy imaging

SEM imaging, performed by Tracey Davey of the Electron Microscope Research Services unit at Newcastle University, was used to give a high resolution visual observation of the samples. Samples were mounted onto a holder and coated with a 10nm gold film. This thin coating prevents the build-up of charge during the SEM imaging process. Samples were loaded into the SEM chamber which was then evacuated down to

10^{-6} mbar. Images of the fracture were taken at a variety of viewing angles to help interpret the exact fracture mechanism. The results are presented in chapter 6.

Chapter 4. Raman Spectroscopy

4.1. Introduction

Continuous beam Raman spectroscopy is the primary measurement technique used in this experiment. Utilisation of the technique is due to its ability to characterise the stress/strain condition of a particular position of a MEMS structure during dynamic loading. The main advantages of such a technique is that surface features are not required to characterize the 3D motion as the crystal lattice is used as the reference frame and that it is suitable to high frequency measurements. Another advantage of the technique is that it is also capable to characterise the stress/strain of a high frequency MEMS structure utilising a standard default setup or with very minimum modifications of a commercially available Raman system. This advantage makes the method easily implementable outside the campus laboratory.

The works were also designed to justify the usability and to develop an utilisation procedure of a dynamic Raman spectroscopy characterisation method in the reliability prediction of MEMS devices. The justification of this usability was done by evaluating the capability of the method in acquiring the necessary data, the accuracy of the measurements and the resolution of the characterisation.

As the measured stress/strain was determined by interpreting the Raman profiles, a calibration factor was also calculated within this experiment. The calibration factor was determined by relating a series of gradually increasing stress and its Raman shifts under a four point bending machine. This calibration factor was then used to interpret the stress/strain of the device structure from the Raman profile broadening taken using the dynamic Raman procedure. The result of the measurement utilising this procedure was evaluated with an ANSYS simulation to allow for the finite beam spot size and penetration depth. A calculation averaging the stress due to the diameter of the laser spot and the laser penetration through the device surface was made. After the capability of such a characterisation procedure was known, a reliability prediction procedure utilising the characterisation procedure was developed.

The reliability of this characterisation technique to be used in this experiment is discussed and evaluated in this chapter. The main consideration of the evaluation is to identify its sensitivity to characterise the stress/strain induced during the sample loading. A Raman profile peak shifting of a SCS (single crystal silicon) MEMS structure of 0.02 cm^{-1} in some particular conditions is related to about 10 MPa stress applied to such

structure. This approximated relation indicates the sensitivity level of measurement available during the experiment. To evaluate the reliability of the technique it is necessary to evaluate the factors that potentially affect the sensitivity that includes but is not limited to technical specification of the Raman system available within our laboratory, spectrum intensity, spectral resolution and spatial resolution.

Calibration of the technique that relates the Raman profiles characteristic to the stress/strain are described and discussed in this chapter. Such a calibration factor was taken from flexural loading under a four point bending machine and utilising static Raman spectroscopy. The calibration factor was determined by evaluating the radius of curvature and the Raman shift of a SCS flexed under a four-point bending machine. The static calibration factor determined in this experiment shows good agreement compared to published calibration data.

Using this calibration factor, the reliability of the dynamic characterisation method was evaluated by estimating its accuracy and the uncertainty of the measurement result. The tests were done on a microcantilever beam vibrated at its resonance frequency and driven to a series of selected deflections. The Raman profile broadening and the deflections during the vibration were recorded and evaluated. The deflection of the beam during vibrations were characterised either under laser vibrometer or visual observation using a camera monitor. A comparison between analytical calculation and measured stress was also made showing good agreement.

All of the Raman measurements in this experiment were taken from a (100) surface plane of single crystal silicon (SCS) using a [001] incident light of 632.8 nm HeNe laser and analysis done on the [001] back scattered light from the sample. This Raman geometry limits the measurement capability to only the particular peak related to the longitudinal direction. This restricts the determination of stress/strain to this direction only.

4.2. Raman Spectra

4.2.1. Raman Spectra of Single Crystalline Silicon

The single crystalline structure of silicon (SCS) exhibits a sharp triply degenerate Raman peak of two transverse and one longitudinal optical phonon modes centred at ω_0 = 521 cm^{-1} for a stress-free condition. When the incident and scattered light are both in [001] direction, the two transverse modes will be polarised along [100] and [010]

direction while the longitudinal mode will be polarised along [001] direction. The relative intensity of this scattered light is given by [88]:

$$I \propto \sum_i |p_I^T \cdot R_i \cdot p_S|^2 \quad i = 1,2,3 \tag{4—1}$$

with p_I and p_S as the polarisation vector of the incident and the scattered light whilst R_i is the polarisability second-rank tensor given by [32]:

$$R_1 = \begin{pmatrix} 0 & 0 & 0 \\ 0 & 0 & 1 \\ 0 & 1 & 0 \end{pmatrix} \tag{4—2}$$

$$R_2 = \begin{pmatrix} 0 & 0 & 1 \\ 0 & 0 & 0 \\ 1 & 0 & 0 \end{pmatrix}$$

$$R_3 = \begin{pmatrix} 0 & 1 & 0 \\ 1 & 0 & 0 \\ 0 & 0 & 0 \end{pmatrix}$$

which corresponds to the crystal direction of [100], [010] and [001] direction respectively.

For the Raman geometry being in used in this experiment, which implemented the incident and collecting the back scattered light from the [001] direction on a (001) plane, the polarisation direction vectors of both incident p_I and the back-scattered p_S have the form of $\begin{Bmatrix} k \\ l \\ 0 \end{Bmatrix}$ with arbitrary values of k and l. For this Raman geometry, by incorporating such a vector direction to the equation 4—1, the nonzero Raman backscattered intensity is only the longitudinal mode (LO_Z). Using Porto notation, the Raman geometry that was use for the entire measurement of this experiment can be considered as [001], $[k_I\ l_I$ 0], $[k_S\ l_S$ 0], [001] where index I and S are related to incident and scattered light respectively.

4.2.2. Voigt fitting for Raman spectra fitting

The Raman data from the measurement was fitted to a Voigt profile $f_V(\omega)$ that is composed from a convolution of Lorentzian profile $f_L(\omega)$ and Gaussian profile $f_G(\omega)$ given as:

$$f_V(\omega) = f_L(\omega) \otimes f_G(\omega) \tag{4—3}$$

with the Lorentzian profile as:

$$f_L(\omega) = \frac{\alpha_L}{\pi} \frac{1}{(\omega - \omega_0)^2 + \alpha_L^2} \tag{4—4}$$

and the Gaussian profile as:

$$f_G(\omega) = \frac{1}{\alpha_G\sqrt{\pi}} exp\left[-\left(\frac{\omega - \omega_0}{\alpha_G}\right)^2\right] \tag{4—5}$$

with α_L as the half-width of the Lorentzian profile and α_G as the Gaussian profile half-width while ω and ω_0 are the wavenumber and the peak profile wavenumber respectively.

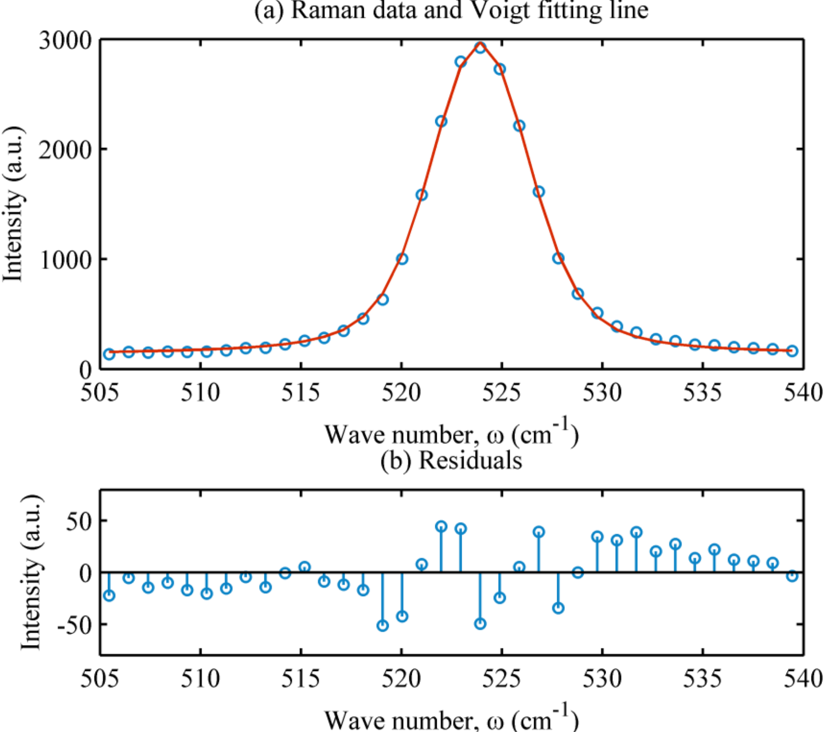

Figure 4—1: Typical fitting of Raman profile data to a Voigt profile.

The fitting of the data was implemented by utilising a non-linear least squares fitting routine with five parameters of the Gaussian and Lorentzian half-widths, the peak wavenumber ω_0, the background level and the intensity-scaling factor. Figure 4—2 shows a typical fitting of Raman data to a Voigt profile. The data used in this figure is taken using the lowest data density available from the Raman system available. In this case, it can also be seen from the figure that the Raman profile is composed from Raman data having a density about 1 data for every cm^{-1} wavenumber. More detail of such data density will be discussed in the following section.

4.2.3. Data density and spectral resolution

Since the data collections in this experiment were dealing with the value of stress/strain that was mostly measured from the characteristic Raman profiles, high accuracy of the spectra acquisition was important. Evaluations in this aspect were done to get an accurate interpretation of stress/strain within the test structures. Based on an evaluation of the data conveyed by the Raman system available within our laboratory under various settings, a maximum data density of 23.80/cm^{-1} was available. The highest data density available from the machine is preferable for all measurements during the experiment. Other setting and data densities can be seen from table 5—1. For a rough approximation of the data density effect in this experiment, it is compared to the Raman profile width of single crystal silicon which is about 4 cm^{-1}. Note this also depends on the instrumental width of the Raman system. A 0.02 cm^{-1} of Raman peak shifting of single crystal silicon is correlated with about 10 MPa uniaxial stress.

Table 4—1: Additional data density utilising extended data collection available in the Raman system equipment.

Spectrometer grid/mm	extended data collection per CCD pixel	distance between data (cm^{-1})	approx. data density per cm^{-1}
600	1	1.0412	0.96
1800	1	0.2531	3.95
1800	2	0.1261	7.93
1800	3	0.0841	11.89
1800	4	0.063	15.87
1800	5	0.0504	19.84
1800	6	0.042	23.8

The extended data collection per CCD pixel is made available by utilising Kiefer Scan mode. The method consist of shifting the grating step by step so that each individual spectral element is detected several times on different pixels of the detector. The method also called sub-pixel offset mode that make use very small overlaps in the spectrum, which provides an enhanced band definition. Here, a shift in position, will move the grating position by an amount less than one pixel on the detector that is called a sub-pixel. Operation procedures of this mode is available in the manual guide of LabSpec® Spectroscopy Suite Software which came packaged with the Horiba Jobin Yvon® Raman system. This method is essential to be used in SCS strain characterisation as it directly relates to the resolution of the strain characterisation.

4.3. Peak position calibration

It was found that during the measurements, the Raman machine shows an unstable behaviour that the measured wavenumber from a same SCS sample condition was constantly changing by as much as ± 1 cm^{-1} which is unacceptable for the stress/strain characterisation. A feature of the Raman machine to calibrate the wavenumber fault to a correct one is available by adjusting the reading to a reference wavenumber taken from a standard known wavenumber. But as the wavenumber changing is happen in a quite short time interval, the method becomes inefficient and a continuous wavenumber correction was needed. To get rid of this problem, light from a Ne bulb was used to give a reference wavenumber to be included in the measurement frame within the wavenumber range. Using this method, the calibration can be made for every measurement. Ne lines having wavelengths of 650.65 nm and 653.28 nm were introduced into the Raman system. With an actuation He-Ne laser light of 632.81 nm then the neon will be seen as line shapes having wavenumber 433.1895 cm^{-1} and 495.1912 cm^{-1}, seen in the measurement frame as a reference. The incorporated Ne lines into the measurement frame can be seen in figure 4—3. Any reading deviation of such reference line wavenumbers was then used to compensate the silicon wavenumber peak to the correct wavenumber.

A series of measurements was done on a (100) single crystal silicon (SCS) using a [001] Raman geometry for both incident and scattered light without the presence of load to test the reliability of the method. The test was done on the same sample being used in the experiment. There were two conditions being incorporated during the test, the first one was environment controlled utilising an air-conditioner to keep the laboratory temperature within 20°C ± 2°C and relative humidity of 60% ± 10% and the other one uncontrolled. The uncontrolled environment had temperature fluctuations of 18°C - 28°C with relative humidity unrecorded. The measurement from the controlled environment shows a more stable result compared to the uncontrolled one. It can be seen from figure 4—3 that the peak to valley deviation is 0.029 cm^{-1} and 0.063 cm^{-1} with standard deviation of 0.01221 cm^{-1} and 0.02579 cm^{-1} for controlled and uncontrolled environments respectively, as shown in figure 4-4. The average peak position for the controlled one is 520.99794 cm^{-1} and 521.01414 cm^{-1} for the uncontrolled one, which showed a difference of only 0.0162 cm^{-1}. The measurement result from the uncontrolled environment was more unstable when compared to the controlled one, but the Si peak wavenumber after correction was still acceptable in both cases however the controlled environment was

more preferable. From the above evaluation of this test, it can be regarded that the method utilising the Ne line as a reference line is reliable.

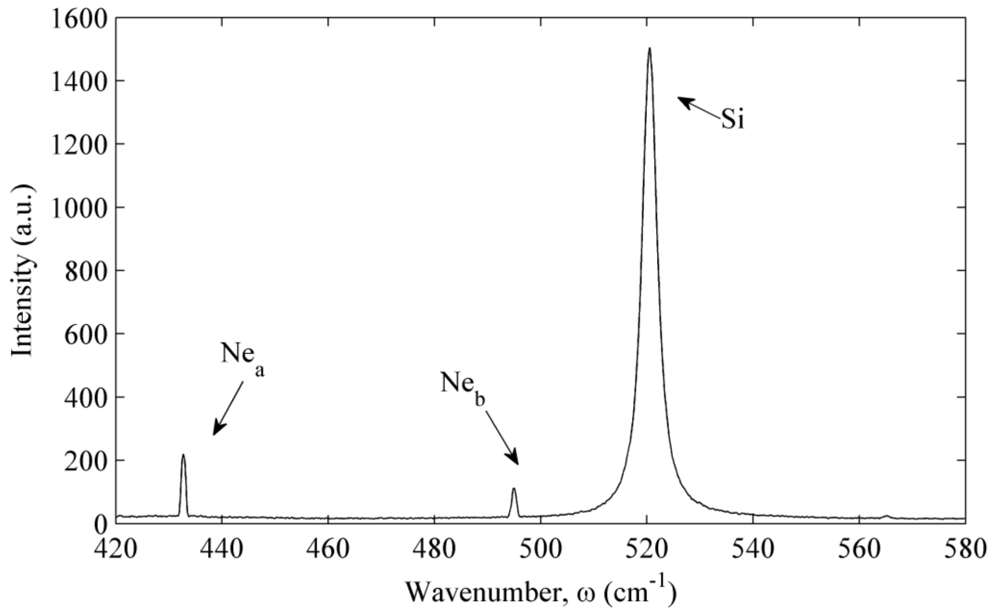

Figure 4—2: Ne spectrum lines as reference lines.

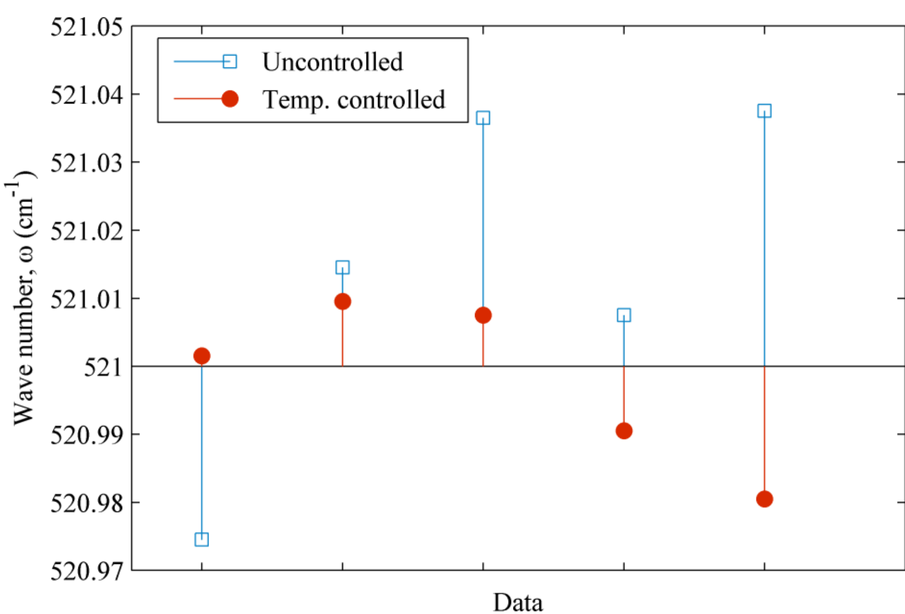

Figure 4—3: Peak position correction using Ne line wavenumber as a reference.

4.4. Raman shift and stress relation calibration

The relation of Raman shift ($\Delta\omega$) and stress (σ) was calibrated by measuring the Raman peak wavenumber of single crystal silicon beam under a bending load and compared with the unshifted peak (ω_0). A four point bending setup was in use to introduce pure bending load to the sample. This procedure was expected to give a uniform stress distribution along the mid span of the bending system so that the Raman

characterisation can be done easily in terms of spatial laser spot positioning on the sample surface. As long as the spot of the laser beam fell anywhere within the mid span of the bending setup, the characterisation would be expected to have the same results. Wavenumber correction due to the Raman system instability was also introduced by incorporating particular Ne lines within the measurement frame. The internal stress due to applied bending was determined by measuring the radius of curvature of the beam sample using a surface profiler and calculated using Euler-Bernoulli beam theory. As discussed in the mechanical properties of single crystal silicon section, the Young's modulus of [110] direction is in use to consider the stress direction due to the anisotropic behaviour of the material. The calibration factor from this measurement is also compared with earlier published papers.

4.4.1. Raman-strain dependency

The present of strain in the crystal lattice breaks the degeneracy and shifts the peaks due to a symmetry reduction of the Raman tensors, which are linear to the applied load [36, 38]. When the degeneracy is broken the three Raman peaks will split and shift to new wavenumbers that can be calculated by finding the eigenvalues λ_i with $i = 1, 2, 3$ that is referred to the crystal direction of [100], [010] and [001] respectively from the given characteristic equation below [89, 90]:

$$\begin{vmatrix} p_D\varepsilon_{11} + q_D(\varepsilon_{22} + \varepsilon_{33}) - \lambda_1 & 2r_D\varepsilon_{12} & 2r_D\varepsilon_{13} \\ 2r_D\varepsilon_{12} & p_D\varepsilon_{22} + q_D(\varepsilon_{11} + \varepsilon_{33}) - \lambda_2 & 2r_D\varepsilon_{32} \\ 2r_D\varepsilon_{13} & 2r_D\varepsilon_{32} & p_D\varepsilon_{33} + q_D(\varepsilon_{11} + \varepsilon_{22}) - \lambda_3 \end{vmatrix} = 0 \quad (4—6)$$

where p_D, q_D and r_D are the phonon deformation potentials (PDPs), which are material constants. The values of p_D/ω_0^2, q_D/ω_0^2 and r_D/ω_0^2 are reported as -1.49, -1.97 and -1.61 respectively by Chandrasekhar et al [91] and -1.85, -2.31 and -0.71 by Anastassakis et al [92]. The shifted frequencies to be determined are related to the unstrained wavenumber ω_0 by:

$$\omega_i^2 = \omega_0^2 - \lambda_i \quad i = 1,2,3 \quad (4—7)$$

which for small strains can be approximated as [36]:

$$\Delta\omega_i = \omega_i - \omega_0 \approx \frac{\lambda_i}{2\omega_0} \quad i = 1,2,3. \tag{4—8}$$

The structures used in this experiment were fabricated from a (100) SCS wafer to have a coordinate system with unit vector parallel to [110], [-110] and [001] for x, y and z respectively. For the convenience of calculations, the usages of the crystal coordinate parallel to [100], [010] and [001] is preferable. Hence, the axial stress σ_{xx} that coincides with the [110] direction can be converted into tensors of σ_{ij} and ε_{ij} in the crystal coordinate system as [93]:

$$\sigma_{ij} = \begin{bmatrix} \frac{\sigma_{xx}}{2} & \frac{\sigma_{xx}}{2} & 0 \\ \frac{\sigma_{xx}}{2} & \frac{\sigma_{xx}}{2} & 0 \\ 0 & 0 & 0 \end{bmatrix} \tag{4—9}$$

and,

$$\varepsilon_{ij} = \begin{bmatrix} \frac{(S_{11}+S_{12})}{2}\sigma_{xx} & \frac{S_{44}}{2}\sigma_{xx} & 0 \\ \frac{S_{44}}{2}\sigma_{xx} & \frac{(S_{11}+S_{12})}{2}\sigma_{xx} & 0 \\ 0 & 0 & 0 \end{bmatrix} \tag{4—10}$$

with S_{11}, S_{12} and S_{44} as the compliance tensor of SCS. By applying equation (4—6) to equation (4—10), the eigenvalues are:

$$\lambda_1 = \frac{1}{2}[p\sigma_{xx}(S_{11}+S_{12}) + q\sigma_{xx}(S_{11}+3S_{12}) + r\sigma_{xx}S_{44}]$$

$$\lambda_2 = \frac{1}{2}[p\sigma_{xx}(S_{11}+S_{12}) + q\sigma_{xx}(S_{11}+3S_{12}) + r\sigma_{xx}S_{44}]$$

$$\lambda_3 = [p\sigma_{xx}S_{12} + q\sigma_{xx}(S_{11}+S_{12})] \tag{4—11}$$

having direction of [110], [-110] and [001] respectively. For stressed crystal, the Raman polarisability tensor of the unstressed crystal R_i as shown in equation (4—2) is different for each of the initially degenerate peaks and assumed to have a linear relation to the unstressed tensor as [35]:

$$R_{i_s} = (n_1)_i R_1 + (n_2)_i R_2 + (n_3)_i R_3 \quad i = 1,2,3 \tag{4—12}$$

with $(n_1)_i$, $(n_2)_i$ and $(n_3)_i$ as the directional cosines of the ith eigenvector shown in equation (4—11) and each of the ith initially degenerate peaks. The modified Raman polarisability tensor then can be shown as:

$$R_{1_s} = \frac{1}{2}\sqrt{2}\begin{pmatrix} 0 & 0 & 1 \\ 0 & 0 & 1 \\ 1 & 1 & 0 \end{pmatrix} \quad (4—13)$$

$$R_{2_s} = \frac{1}{2}\sqrt{2}\begin{pmatrix} 0 & 0 & 1 \\ 0 & 0 & -1 \\ 1 & -1 & 0 \end{pmatrix}$$

$$R_{3_s} = \begin{pmatrix} 0 & 1 & 0 \\ 1 & 0 & 0 \\ 0 & 0 & 0 \end{pmatrix}.$$

As the Raman measurement are taken using incident and scattered light in the [001] direction, there will be only the singlet longitudinal Raman spectra that corresponds to the [001] direction detected. The Raman shift from equation (4—8) can be rewritten to include only the detected peak as:

$$\Delta\omega = \frac{\lambda_3}{2\omega_0} = \frac{p\sigma_{xx}S_{12} + q\sigma_{xx}(S_{11} + S_{12})}{2\omega_0}. \quad (4—14)$$

The Raman shift due to applied uniaxial stress relation can then be approximated by applying the phonon deformation potentials from Anastassakis [92] that were mentioned earlier as:

$$\sigma_{xx} \cong -434\Delta\omega \quad (4—15)$$

while using the Chandrasekhar [91] phonon deformation potentials gives a relation of:

$$\sigma_{xx} \cong -518\Delta\omega. \quad (4—16)$$

The above calibration factors will be used as comparison values to the calibration factor being determined in this experiment that will be discussed in the following section.

4.4.2. Four point-bending

A four point bending was used to allow for the simplest case of pure bending, that is a beam possessing a vertical axis of symmetry, subjected to equal and opposite end couples. This configuration also gives a uniform distribution of stress within the inner span of loading. This uniformity offers a particular advantage to this experiment in that the repeatability of the Raman measurement is more guaranteed in terms of spatial point

positioning of the laser beam. The strain at the segment shown in Figure 3—5 of the beam is given by:

$$\varepsilon_x = \frac{dx' - dx}{dx} = -\frac{z}{\rho} = -\mathcal{K}z \tag{4—17}$$

where $\mathcal{K} = 1/\rho$ with $\mathcal{K}$ and ρ as the curvature and the radius of curvature of the neutral axis of the beam respectively. The equation gives the relation between measured radius of curvature and the axial strain ε_x as a function of distance z to the neutral axis. The maximum strain ε_{max} occurs on the surface of the beam and maximum distance to the neutral axis is $z_{max} = t/2$ with t as the thickness of the beam. The maximum strain then can be written as:

$$\varepsilon_{max} = \frac{t}{2\rho} \tag{4—18}$$

and the axial stress on the beam surface for a particular crystal direction of x can be determined from:

$$\sigma_x = \frac{tE_x}{2\rho}. \tag{4—19}$$

whilst all other stresses are zero:

$$\sigma_y = \sigma_z = \tau_{xy} = \tau_{xz} = \tau_{yz} = 0. \tag{4—20}$$

For axis coordinate x coincide with [110] crystal direction, the axial stress in x direction σ_x can be rewritten as:

$$\sigma_x = \frac{tE_{[110]}}{2\rho} \tag{4—21}$$

with $E_{[110]}$ as Young's modulus in [110] crystal direction as calculated in earlier section. Other than the above-mentioned equation of stress to describe the sample condition under pure bending, it is also common to represent such a condition in terms of volumetric strain as:

$$e = e_0 + \Delta e \tag{4—22}$$

with $e_0 = dxdydz$ and $\Delta e = \varepsilon_x dx \varepsilon_y dy \varepsilon_z dz$ for an infinitesimal volume, thus:

$$e = (1 + \varepsilon_x)dx(1 - \nu\varepsilon_x)dy(1 - \nu\varepsilon_x)dz \tag{4—23}$$

Hence, the volumetric strain can also be written as:

$$\varepsilon_V = \frac{\Delta e}{e_0} = (1 - 2\nu)\varepsilon_x = \frac{1 - 2\nu}{E}\sigma_x. \tag{4—24}$$

while the volumetric μstrain is the more common term being used in microsystem and can be regarded as $\varepsilon_V \cdot 10^6$.

The bending tests were done by measuring the radius of curvature of the sample surface ρ_s using Zygo® surface profiler as can be seen in Figure 3—9. The samples we used for this four point bending were from a 675 μm thick (100) single crystalline silicon wafer and having a dimension of 2 mm × 10 mm with [110] axial direction. As the technique is measuring the surface radius of curvature then the radius of curvature of the neutral axis ρ has to be calculated from the surface radius of curvature and incorporating the sample thickness t as:

$$\rho = \rho_s - t/2. \tag{4—25}$$

As the radius of curvature value is measured, the axial stress in the [110] direction can be determined from equation (4—21). By varying the bending load, and recording the radius of curvature and the Raman profile, the relation between them can be determined and consider a calibration factor for the rest of this experiment.

4.4.3. Raman Shift due to Applied Load

From the bending tests using the four point bending machine as discussed in the previous section, the relation of Raman shift due to the applied load can be seen in Figure 4—4: Static Raman shift and stress calibration. The data fitting gives a relation of $\sigma_x \cong -481.5\Delta\omega$ for [110] crystal direction axial loading and (001) Raman geometry scattering with σ_x as the axial stress in MPa and $\Delta\omega$ as the Raman shifts in cm^{-1}. The Raman shifts $\Delta\omega$ can be described as $\Delta\omega = \omega_0 - \omega_m$ with ω_0 as the Raman peak wavenumber of single crystal silicon at 521 cm^{-1} and ω_m as the measured Raman peak position during loading. The test also includes the uncertainties that are scattered approximately within ±15 MPa from peak to valley about the fitting line, which is if it converted to our calibration number, is related to about 0.083 cm^{-1}. This uncertainty is larger compared to the stress-free test discussed in the earlier section that was mentioned to be less than 0.02 cm^{-1}. This additional uncertainty is expected as the contribution of the test procedure

which are incorporating two machines, the surface profiler and the Raman machine, thus there was a possibility for the sample to have a changing load during transport between the machines.

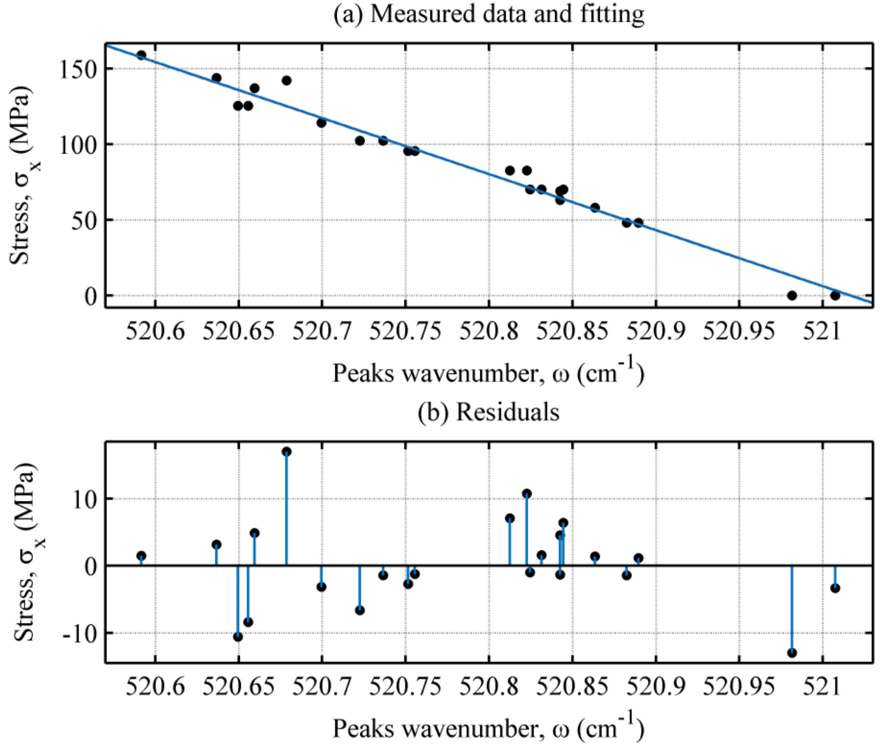

Figure 4—4: Static Raman shift and stress calibration

The calibration factors to relate the shifts due to a uniaxial load were also made by Srikar et al [42] which were calculated from the phonon deformation potentials (PDP) of Anastassakis [92] and Chandrasekhar [91] given as $\sigma_x \cong -434\Delta\omega$ and $\sigma_x \cong -518\Delta\omega$ respectively. Comparison of our calibration factor to these calibration factors can be seen in Figure 4—5: Anastassakis, Chandrasekhar and measured calibration factor comparison.

An approximation of about 0.02 cm^{-1} of frequency shifting for every 10 MPa load changing can also be used for convenience for uniaxial and biaxial stress [94]. Other calibration factor of Raman peak shifting for silicon due to applied load in term of volumetric μstrain [67] shows a factor of 5.2×10^{-4} cm^{-1}/volumetric μstrain. In the case of uniaxial strain this calibration factor can be converted into the same term as above. On the other hand, our calibration factor can also easily be converted to a volumetric μstrain by assuming the material to have an isotropic behaviour so that equation 4—12 is applicable by incorporating a Young's modulus of 169 GPa and Poisson's ratio of 0.29. The assumption gives a calibration factor of 8.1454×10^{-4} cm^{-1}/volumetric μstrain for

our calibration, 7.3173×10^{-4} cm^{-1}/volumetric µstrain and 5.9754×10^{-4} cm^{-1}/volumetric µstrain for Anastassakis and Chandrasekhar respectively.

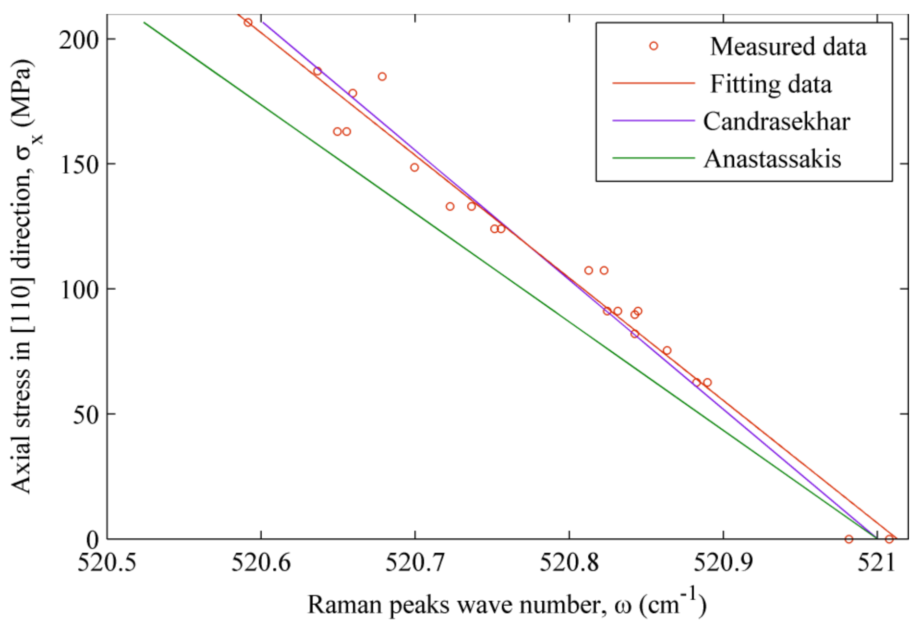

Figure 4—5: Anastassakis, Chandrasekhar and measured calibration factor comparison

4.4.4. Off-axis Raman spectroscopy

Raman geometry of incident and scattered laser beam direction of [001] which was used in this experiment has an inherent limitation that the procedure is only sensitive to longitudinal optical phonons. Different configurations of the above mentioned is available to overcome such limitations.

When a uniaxial stress is applied to [100] or [111], the threefold degeneracy of the Raman peak will split into a singlet and doublet whilst the hydrostatic component of the applied stress will shift the frequency of the optical phonons. By incorporating a different configuration of the incident and scattered light direction and also by filtering the light polarisation using analysers, all of the Raman peak can be collected. This configuration is also known as an off-axis Raman spectroscopy [75] which incorporate an inclined incident light rather than normal to the sample surface and selecting the peak using polarisers.

Although the Raman effect in silicon is well characterised and there have been many attempts by researcher to predict the unknown stress state and magnitude of the stress components, major limitations still exist. When attempting to isolate the peaks by selecting the polarisation of the incident and scattered light, it is still necessary to know

the stress state. The ratios of all stress components have to be known beforehand as only magnitude of them will be taken from the measurements [35].

4.5. Dynamic Raman Characterisation

The utilisation of dynamic Raman characterisation in this experiment is intended to characterise the stress/strain state of single crystalline silicon structures by capturing the shifting of the Raman peak during dynamic loading. Recently, there are two methods to characterise the stress/strain of a structure during its harmonic motion, modulated Raman spectroscopy and Raman profile broadening. The first method captures the Raman peak shifting by 'freezing' the structure on a fixed phase and compares the result to the unshifted peak whilst the second method collects all the Raman profiles during the motion. Using the first method, one can characterise the stress/strain condition of the structure of all particular phase of motions and is preferred as by utilising the second method there will only be the maximum stress/strain condition of the structure available. Although the latter is incapable of delivering the phase information, it has an advantage of having a simple experimental configuration and the technique can be implemented in industry utilising a standard Raman machine setup. To date, the Raman profile broadening method is not commonly used, and there are very few published papers exploring the usability of this characterisation technique. In this experiment, only the second method is used to explore its reliability of utilisation in reliability prediction of single crystal silicon MEMS.

4.5.1. Modulated Raman Spectroscopy

As the name suggests, the modulated Raman spectroscopy is implemented by modulating the laser beam in synchronisation with the motion of the structure at a fixed phase. The strobe light will illuminate the structure in a single phase for a particular sampling period/ duty cycle repeatedly to get a Raman profile having a signal to noise ratio for the stress/strain measurement at an acceptable level [13]. A trade-off between the duty cycle of laser beam modulation signal, which is related to the captured Raman intensity, and the measurement accuracy have to be considered. Increasing the duty cycle can increases the intensity of scattered light but it will reduce the accuracy, as there will be a wider range of captured phase of the structure motion in the test. A spectral resolution of 0.02 cm^{-1} Raman shift that relates to 10 MPa of uniaxial stress was reported with a capability to characterise a dynamic structure at frequencies of up to 100 kHz [14].

4.5.2. Raman Profile Broadening

The Raman spectra data captured using continuous Raman spectroscopy is fitted using a modified Voigt distribution. The Raman profile R_0 in a static condition can be described by a Voigt distribution V_f as a function of peak wavenumber position without the present of any load u_0:

$$R_0 \propto V_f(u_0). \tag{4—26}$$

The stress measurements being conducted in this experiment make use of the method which determine the axial stress from a vibrating structure using dynamic Raman spectroscopy from a broadened Raman profile R_B. The method was developed by Hedley and Hu [11, 14] and rewritten here as follow:

$$R_B \propto \int_T V_f\big(u(t)\big). \tag{4—27}$$

As the structure vibrates, the crystal lattice will experience a condition of tensile and compression sinusoidally so that the peak position $u(t)$ at the time of t of the profile will be shifted to the upper and lower wavenumber position compared to the unload peak position u_0 during a period of time T. As the technique of the measurement is collecting all the spectra during the vibration, the Raman profile will be broadened R_B by the sum of the Voigt profiles during that period. If the maximum peak shift during the vibration due to maximum strain of the structure considered as $A_{\max}$, the peak position at any time $u(t)$ during the phase relative to the no-load peak position u_0 can be written as:

$$u(t) = u_0 - A_{\max} \sin\left(\frac{2\pi t}{T}\right) \tag{4—28}$$

That the broadened Raman profile can also be written as:

$$R_B \propto \sum_{t=1}^{T} V\left(u_o - A_{\max} \sin\left(\frac{2\pi t}{T}\right)\right) \tag{4—29}$$

and the measured stress might be determined by applying the calibration factor to the maximum shift $A_{\max}$.

The broadening effect of the continuously captured profiles were simulated using Matlab. The simulation of the broadening effect were made by generating a number of

typical Raman profile of silicon having shifted peaks to a higher and a lower position $u(t)$ about the u_0 and sum all of these profile to produce a broadened profile as can be seen in Figure 4—6.

It can also be seen that the speed of motion is changing sinusoidally along the cycle of motion which affects the intensity, this being differently distributed between the phase as the collected intensity is higher for the slower motion, as the collection duration is longer.

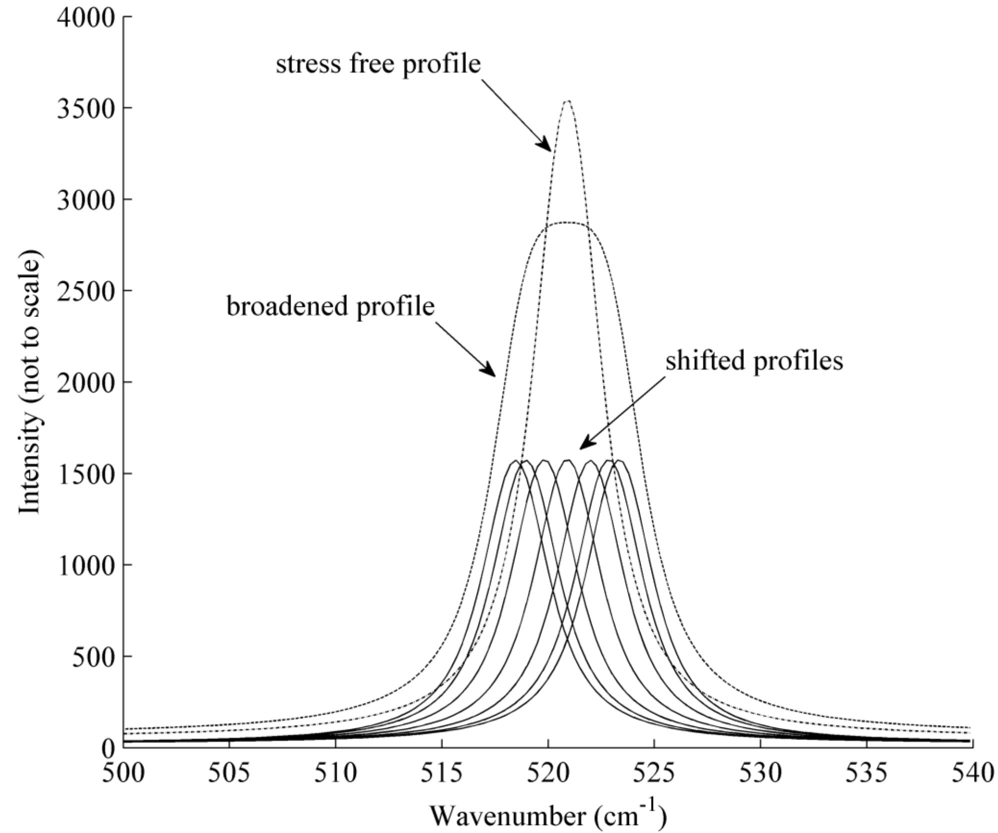

Figure 4—6: Simulation of Raman profile broadening

An evaluation to the method was made with the result as showed in Figure 4—7. A series of measurements were taken to determine the broadening characteristic due to applied load. The measurements were made by vibrating a cantilever beam in its fundamental frequency and increasing the load gradually. For every increment, the deflection of the free-end of the cantilever and the Raman spectra were recorded.

4.5.3. Comparison based on beam deflection

The measured data of stress were determined from the measured Raman profile broadening and converts to stress values by incorporating our calibration factor of 481.5 MPa/cm^{-1} for the Raman peak shifting. A typical Raman profile-broadening can be seen from figure (4—7). The peak shifting was calculated from the Raman profile broadening

using the fitting procedure mentioned in equation (4—29). These measured stresses were plotted against the cantilever deflections to compare with the analytical calculated stress. Such deflections of the in-plane vibration were measured visually on the camera monitor having a magnification of 50×.

From Figure 4—7b the residuals graph shows at a level of approximately ±50 MPa about the fitting line. Such errors are not only from the Raman broadening measurement procedure but also include the visually determined deflection.

From Figure 4—7a it can be seen that the fitting line of the measured stress determined from Raman broadening and the fitting line from the stresses calculated from the measured deflection are almost coincided. But as the measurements were taken in the vicinity of the clamped end fillet, they should show different values having a linear factor that is known as the concentration factor compared to the analytical values. Evaluation of the absence of this concentration factor is done in the next sub-section by incorporating the spot size diameter of the laser beam and the stress distribution in the vicinity of the clamped end fillet of the cantilever beam. The stress distribution in this area was determined using an ANSYS simulation.

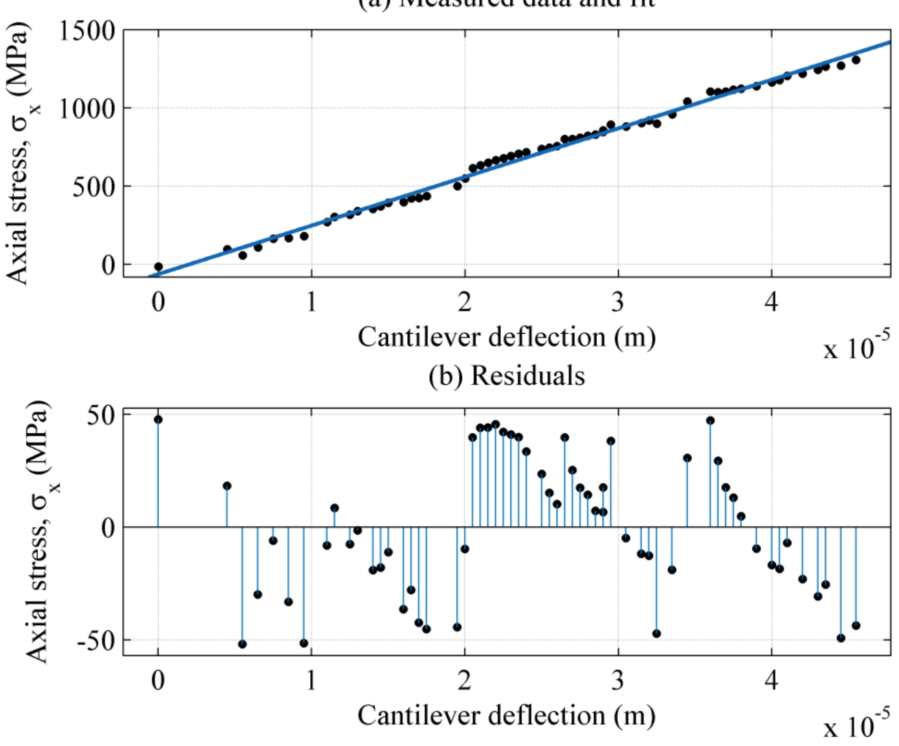

Figure 4—7: Comparison between analytical stress and measured stress using Raman profile broadening on an in-plane motion sample.

4.5.4. Concentration factor, spot size and penetration depth of the laser beam

To evaluate the reason for the absence of the concentration factor in the vicinity of the clamped end fillet as mentioned earlier, there are a number of possible causes of the deviation to be considered; the spot size and penetration depth of the laser beam spreads the measurement result to not only from a single point but an average of a particular area/volume. For in plane movement with Raman geometry perpendicular to the surface plane, the variation of stress/strain is along the surface plane so that the spot size needs to be considered. While for the out of plane motion with the same Raman geometry, the stress/strain variations are along the depth of the cantilever beam so that the penetration depth of the laser beam in the SCS have to be included in the calculation.

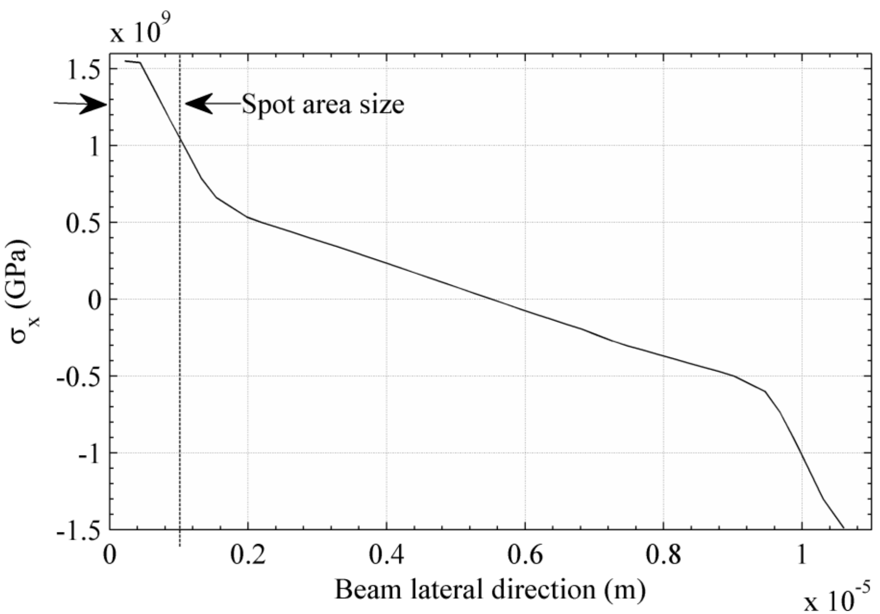

Figure 4—8: Stress distribution across the beam surface at the clamped end during in-plane motion. Spot area size depends on the laser beam diameter which is 1 μm during the experiment.

Calculation and simulation of the same geometry of sample being used in the experiment was done with a chosen maximum deflection in the y component of 40 μm. Having this deflection, the Raman broadening procedure gives a value of 1.163 GPa, the analytical calculation using equation (2—47) gives a value of 1.127 GPa whilst the ANSYS simulation gives the stress distribution as can be seen in Figure 4—8 and Figure 4—9.

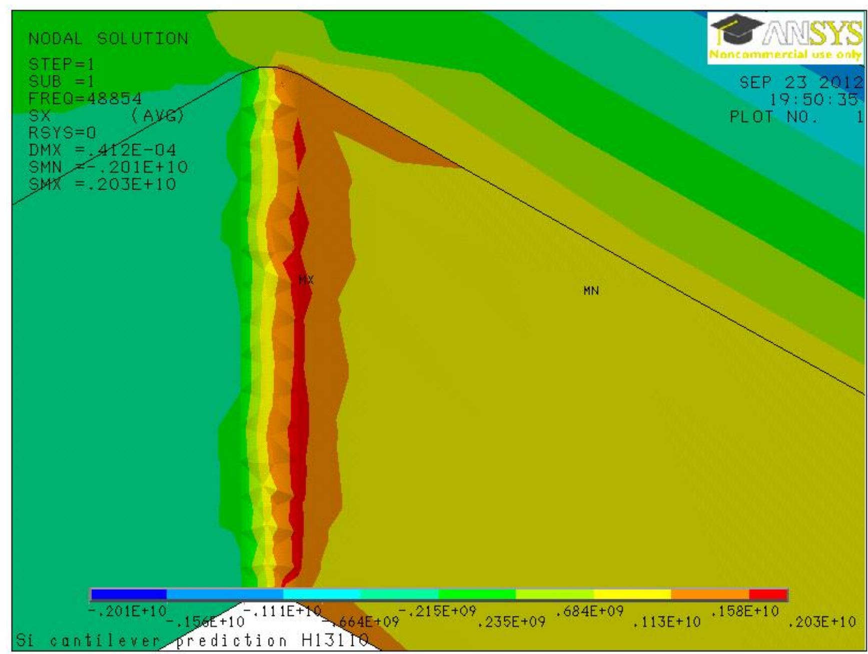

Figure 4—9: Stress distribution in the vicinity of the clamped end fillet of the cantilever beam during in-plane motion. Stress variation about the neutral axis is shown on the upper beam surface.

From Figure 4—8 it can be seen that the laser beam spot, which is about 1 μm in diameter, includes an area with stress range between 1 and 1.5 GPa. Considering such a stress range and the Raman measurement result it can be said that the measurement procedure gives an average result of the measurement area due to the laser spot diameter. From the Figure 4—9 a maximum stress of 2 GPa is seen to exist at the vertical surface of the fillet. This value is about 2 times larger than the analytical calculation but the measurement procedure cannot measure this stress as the location is unreachable by the laser beam in the current experimental setup.

According to this evaluation it can be concluded that the dynamic Raman spectroscopy making use of the Raman profile broadening can be used to characterise a dynamic MEMS structure with moderate accuracy of about ±50 MPa. In utilising this procedure, it is also importance to consider the penetration depth of the laser beam in the material of the sample, the spot size and the relative intensity of every mode of the scattered light to avoid a misinterpretation of the data.

Chapter 5. Weibull parameters determination

This chapter starts with experimental methodology and follows with the procedures used to characterise the devices. There were two type of tests performed, the devices responses due to dynamic load and the fracture behaviour of a series of selected devices. The response characterisation includes the resonance frequencies of first in-plane and the first out-of-plane whilst the fracture behaviour characterisation acquired the scattered fracture strength of the devices. The fracture data was used to obtain the Weibull parameters of such devices which can then be used to predict the reliability.

5.1. Data type

There were two data types being acquired which relates to the modelled prediction methods, the maximum stress of a certain location on the beam when the cantilever beam ruptured, and the rupture position of the beam relative to its root. Both data were taken during device fracture tests under vibration. The devices were actuated to rupture at their resonance frequencies. The load was increased gradually by increasing the supply voltage. The increment steps chosen were based on the measureable stress increment under dynamic Raman characterisation to assure the measurement resolution was properly controlled.

Stress of a certain location on the device induced from vibration, which was determined as the maximum stress, was acquired using dynamic Raman spectroscopy for every increment step.

5.1.1. Experiment procedure

There were two fracture tests implemented. The first one is the fracture test used to obtain the Weibull parameters for composing the prediction. The second one is the fracture test used to justify the reliability of the prediction.

The experimental procedure considered ASTM C1239-07 The standard practice for reporting uniaxial strength data and estimating Weibull distribution parameters for advanced ceramics [82] for Weibull distribution parameters estimation.

The Weibull parameters were obtained from J13/H13 included in the sub-group IV having a frequency range from around 40 kHz and 80 kHz for in-plane and out-of-plane motion. The J/H group is the symmetrical geometry. The sub-group contained 5 different cantilever beam sizes with a 10μm length difference between each (see Table 3—3 for device geometry and Table 5—1 for device grouping). The 13th index has the middle size

as compared with the rest in the sub-group. This chosen selection aimed to enable an evaluation on the effect of both longer and shorter length changes of the same cantilever beam geometry.

The fracture test to justify the modelled prediction methods that are detailed in Chapter 6 were done on all devices available on the dies with the exception of the group F devices having clamped-clamped beams.

5.2. Failure modes and surface roughness consideration

Fracture mode I, the opening mode (a tensile stress normal to the plane of the crack) is the most common failure mode occurring in fracture. The effect of surface roughness is widely known to relate to crack initiation. There are two types of surface roughness in this work that have to be considered, the mechanically polished surface and DRIE surface due to the microfabrication process. Top and bottom surface of the dies were mechanically polished whilst the side surfaces were DRIE. Under the Zygo® profiler the roughness of mechanically polished and DRIE surfaces were examined. R_{max} values are used to quantify roughness. The typical R_{max} for the polished surface lies within a range between 0.3 and 0.5 nm. However, values of R_{max} as large as 2.5 nm have been measured for polished surface. For the DRIE surface, R_{max} between 20 and 45 nm have been measured. Larger R_{max} values indicate a rougher surface. The surfaces profile of the dies can be seen in Figure 5—1 and Figure 5—2.:

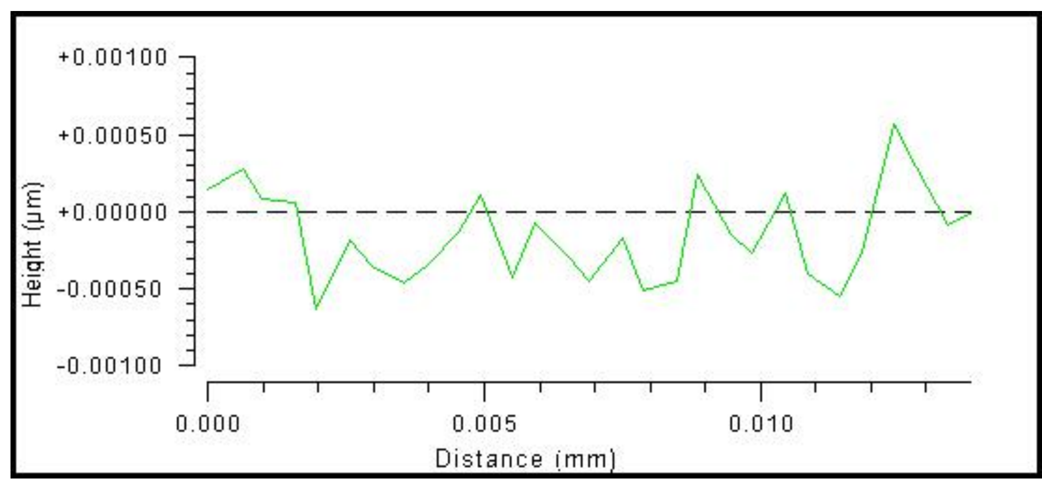

Figure 5—1: Mechanically polished surface profile

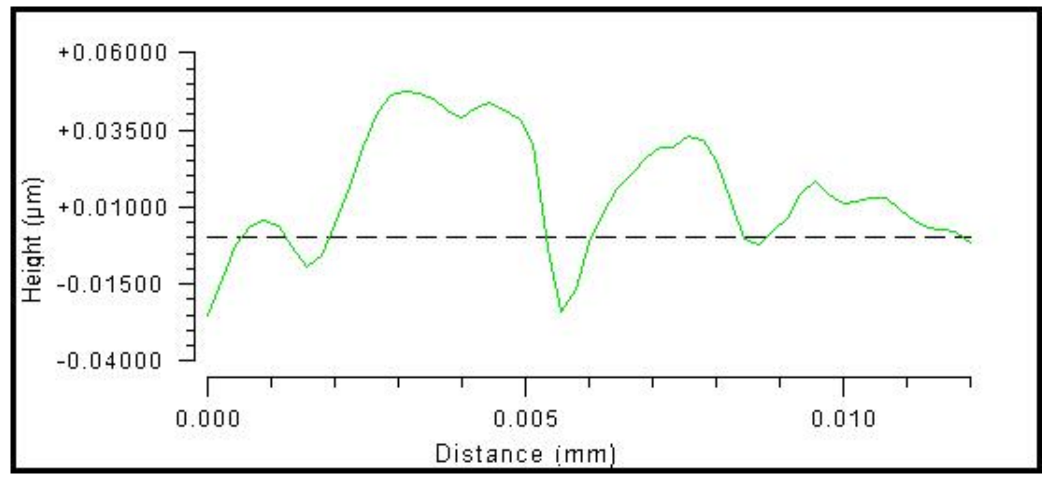

Figure 5—2: DRIE surface profile

The measured roughness values were not intended to be used for quantitative calculation, it was only to see qualitatively that the different roughness was expected to give a different flaw population distribution and thus have particular Weibull distribution parameters.

5.3. Resonance frequencies

The resonance frequency characterisations were done by sweeping over a range of frequencies to actuate the device while observing the response. The sweeping ranges were determined from the predicted resonance frequencies that were calculated using ANSYS. The resonance frequencies under interest were the first in-plane and the first out-of-plane modes. They are the fundamental frequency and the second resonance frequency.

The characterisations were done either using laser vibrometer or visual observations. Limitations were involved on the utilisation of the laser vibrometer in that it was unable to characterise a pure in-plane motion and limited to frequency measurements lower than 100 kHz due to the limitation of the signal analyser in use. These limitations have been detailed in chapter 3. Visual observations were in use to characterise the in-plane motion resonance, as shown in figure 5-3.

5.3.1. ANSYS resonance frequencies computation

The resonance frequencies of the devices were computed using the modal analysis solution procedure available in ANSYS. The device geometry model and material properties together with the boundary conditions were inputted in the pre-processor. Meshing was done semi-automatically by defining a series of divisions on the edge lines.

Table 5—1, below show the resonance frequencies of interest for the devices.

Table 5—1: Resonance frequencies of J/H devices

Device	1st (Hz)	direction	2nd (Hz)	direction	sub-group
J01/ H01	64193	out-plane	86331	in-plane	I
J03/H03	67786	out-plane	91033	in-plane	
J05/H05	71719	out-plane	96176	in-plane	
J07/H07	76036	out-plane	101800	in-plane	
J02/H02	17462	out-plane	23672	in-plane	II
J04/H04	17970	out-plane	24363	in-plane	
J06/H06	18503	out-plane	25087	in-plane	
J08/H08	149200	in-plane	216330	out-plane	III
J10/H10	164680	in-plane	238810	out-plane	
J12/H12	182880	in-plane	265330	out-plane	
J14/H14	204560	in-plane	297260	out-plane	
J16/H16	230630	in-plane	335240	out-plane	
J18/H18	262480	in-plane	382170	out-plane	
J09/H09	43657	in-plane	63680	out-plane	IV
J11/H11	46131	in-plane	67243	out-plane	
J13/H13	48844	in-plane	71147	out-plane	
J15/H15	51828	in-plane	75434	out-plane	
J17/H17	55131	in-plane	85385	out-plane	

5.3.2. Outlying observation due to unusual resonance frequency

In the samples used in this experiment, a normal behaviour of a sample can be presumed by comparing its measured resonance frequencies with resonance frequency of such cantilever beam calculated using ANSYS. The comparison may also be made with the others as the samples were designed with systematic size differences so that a systematic trend in resonance frequencies can be expected.

However, a major defect was sometimes present in the sample giving a test result that can be considered as an outlying observation. In these cases, some of the samples were found stationary when actuated at their expected resonance frequency or the resonant frequency lay far from the expected range of such a device. Therefore, such samples could not be considered as a representation of the population. Outlying observations due to an abnormality were handled based on ASTM E178 and omitted from further analysis.

5.4. Weibull fit of fracture data

The J13/H13 were brought to rupture to obtain the Weibull parameters for both in-plane and out-of-plane motions. The fracture strength data were interpreted from Raman profile broadening and taken at the root of the upper surface of the cantilever beam. The

laser spot was positioned corresponding to the maximum strain as predicted by the ANSYS simulation as discussed in chapter 4.

All of the fracture data were fitted to a Weibull distribution. It was assumed that the strength distribution of the samples used in this experiment follow a Weibull two parameter distribution. It was used not only because the distribution of the fracture data were usually asymmetric about the mean (Figure 5—3 shows the comparison of typical Weibull and normal distribution in a probability distribution plot) but also because the Weibull allows the size effect to be considered in the distribution. These characteristics limit that the data should have to be fitted to Weibull rather than the use of the normal distribution or other distributions even if the data fit well or slightly better to a different distribution function.. The ability of such distribution to consider the size effect is essential due to its utilisation to predict the different size of MEMS device.

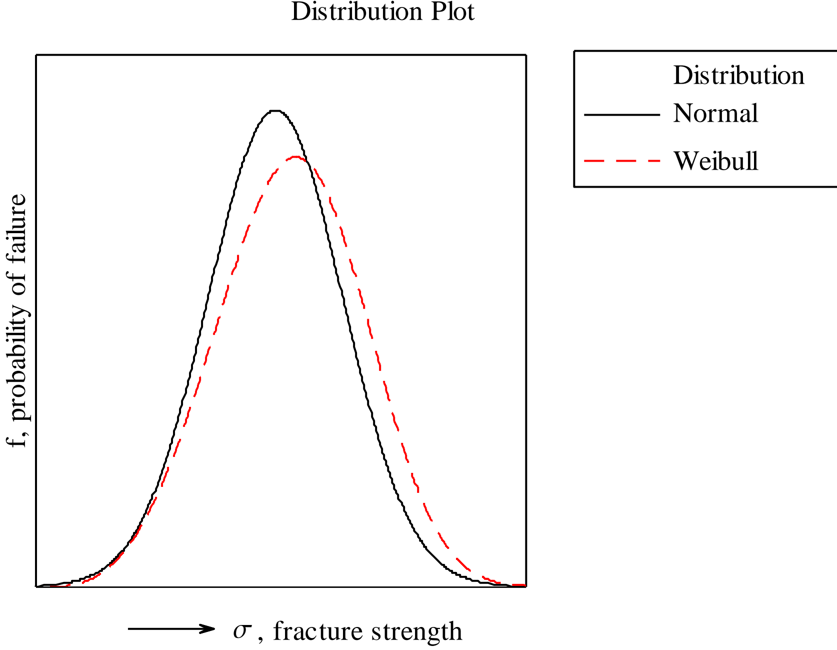

Figure 5—3: Typical probability distribution plot of normal and Weibull distribution. Weibull accommodate asymmetric data about the mean.

The numerical procedure in obtaining the parameter, which was done under Minitab® statistic software, yields the Weibull modulus $\hat{m}$ and the characteristic strength $\hat{\sigma}_{\theta}$. This characteristic strength still includes the test sample geometry and stress gradient condition over the cantilever beam surfaces. Utilisation of such parameters to a different geometry and stress gradient need the estimated Weibull material scale parameter σ_0 as earlier discussed in sub-chapter 2.5. Thus a conversion was necessary. The relationship between the parameters was shown in equation (2—73).

To evaluate the accuracy of the data fitting to the distributions which were estimated using the maximum likelihood, the Anderson-Darling statistic was utilised. The statistic used is a weighted squared distance from the fracture data plot points to the fitted line with larger weights in the tail of the distribution. A smaller Anderson-Darling statistic indicates that the distribution fits the fracture data better. Even though the Weibull distribution provide the best utilisation in case of failure prediction for different geometries due to size variations, comparisons to a different distribution were also made to support the conclusion. Comparisons between Weibull and normal distributions were made.

5.4.1. Mechanically polished surface

The mechanically polished surfaces of J13/H13 were characterised in the out-of-plane mode. The fracture data of the devices were recorded and all of these data were used for statistical evaluations without censoring. Results are shown in Figure 5—4, Figure 5—5 and Figure 5—6.

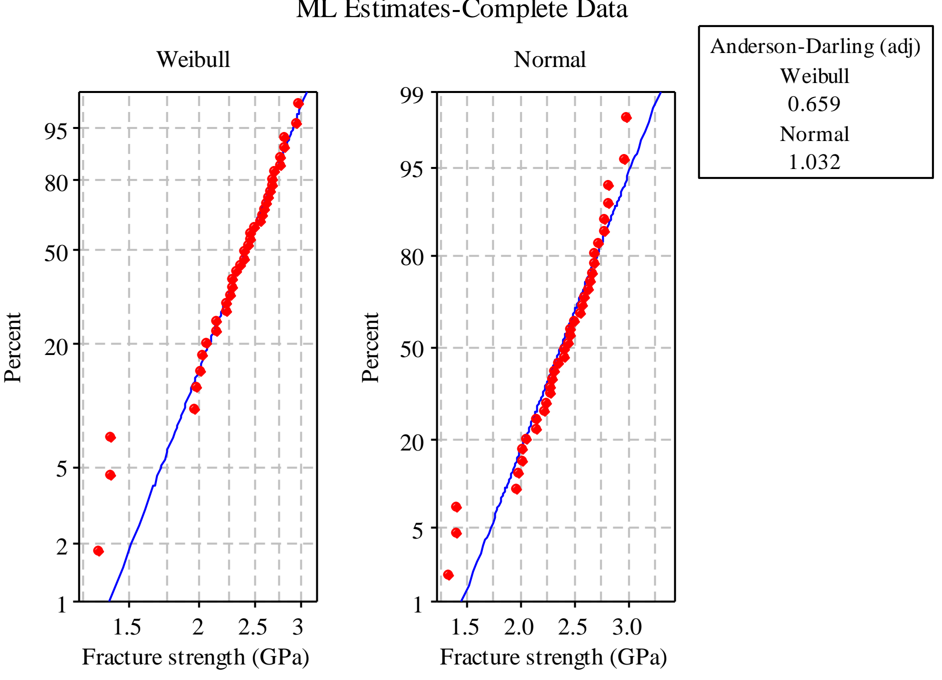

Figure 5—4: Cumulative distribution plot of H13/J13 out-of-plane fracture strength.

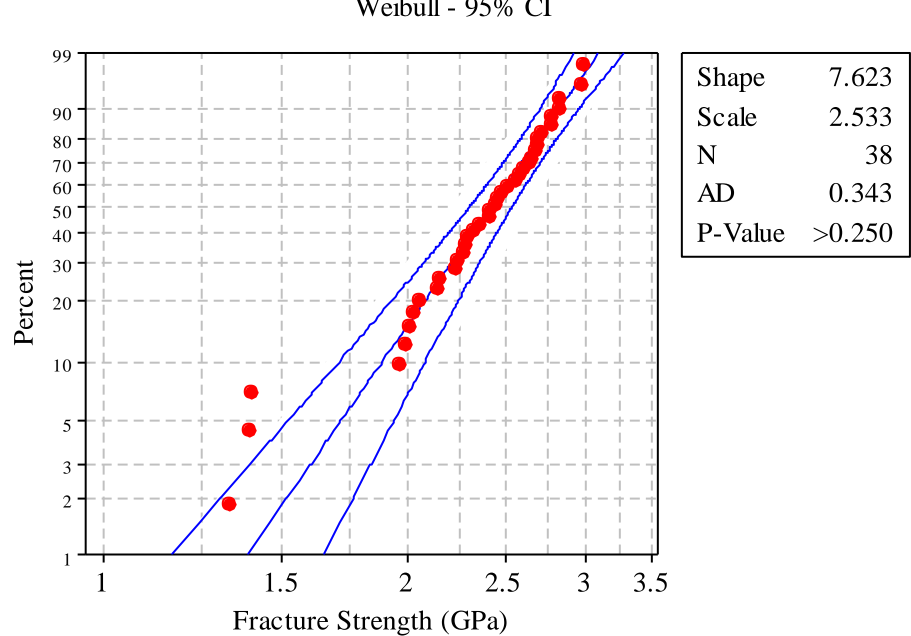

Figure 5—5: Probability plot of H13/J13 out-plane fracture strength

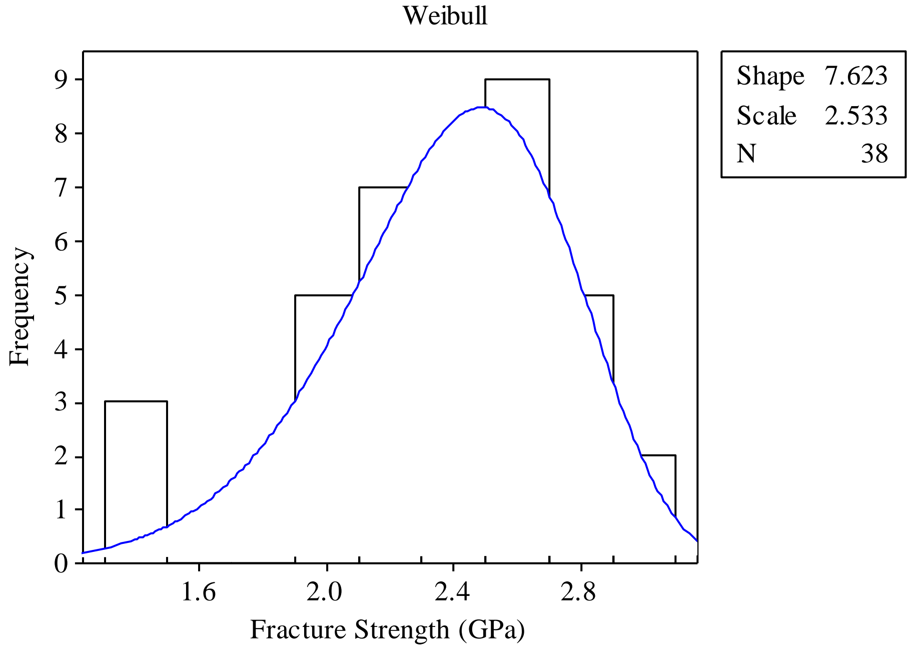

Figure 5—6: Histogram plot of H13/J13 out-plane fracture strength

Test of the data against a normal distribution are shown in Figure 5—4. It can be seen that the data best matched is with the Weibull distribution having an adjusted Anderson-Darling of 0.659 whilst of 1.032 when fitted to the normal distribution. Figure 5—5 shows the probability plot of fracture data of 38 samples with confidence interval of 95% fitted to a Weibull distribution having a shape parameter m of 7.623 and a scale parameter

(characteristic strength σ_0) of 2.533 GPa. A measure of fit in Anderson-Darling was 0.343 and p-value was higher than 0.250 which categorised this as a very good fit. Figure 5—6 shows the spread of the fracture strength as a histogram plot overlaid with such a Weibull fitting line.

5.4.2. DRIE surface

The DRIE surface characterisation to obtain its Weibull parameters was done under a similar procedure. The DRIE surfaces of J13/H13 group devices were characterised for the in-plane mode of each device. The results are presented graphically in Figure 5—7, Figure 5—8 and Figure 5—9. Figure 5-7 show the fit of the data which was determined under a least square estimation over the complete set of the data to a given type of distribution. The data best fit to the Weibull distribution and gave a correlation coefficient of 0.982.

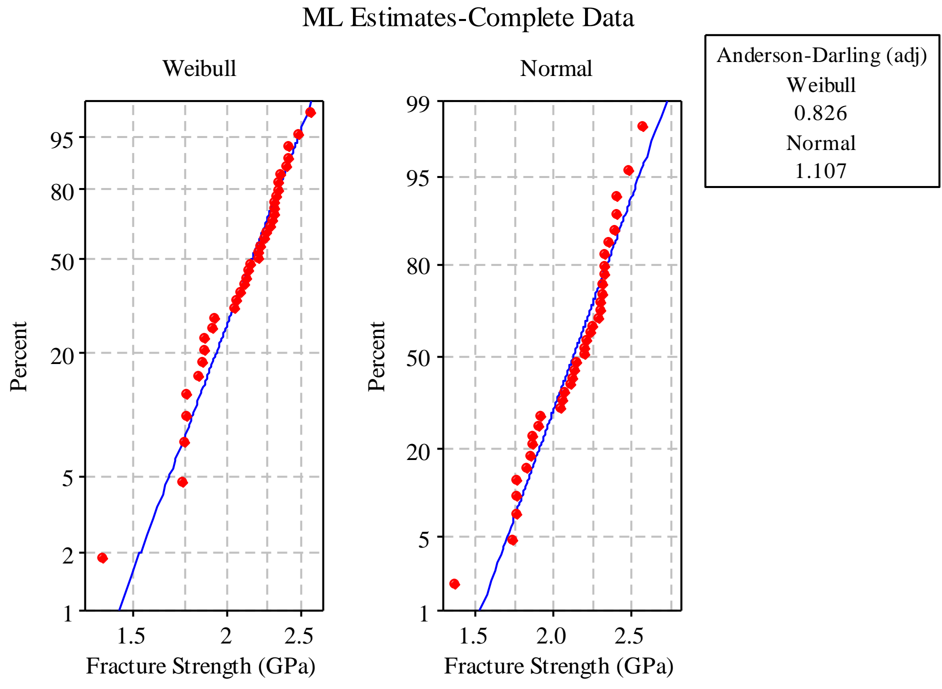

Figure 5—7: Distribution analysis plot of H13/J13 in-plane fracture strength.

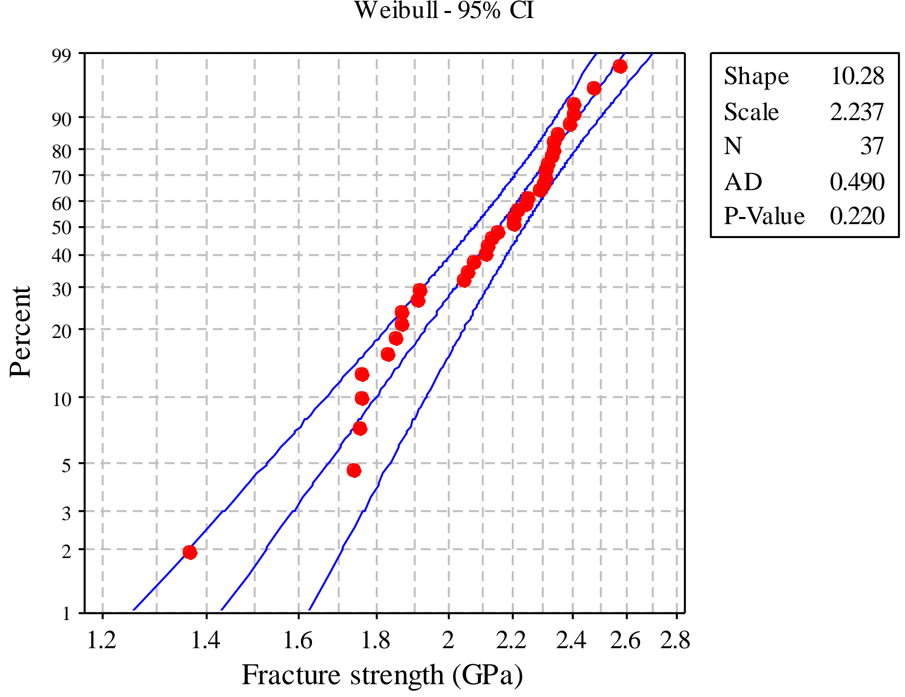

Figure 5—8: Probability plot of H13/J13 in-plane fracture strength.

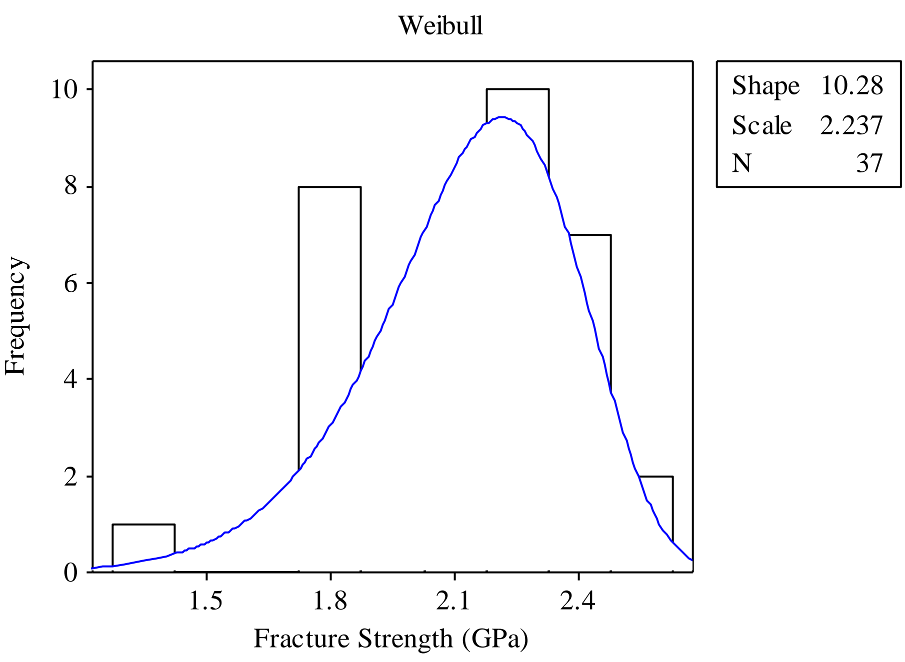

Figure 5—9: Histogram plot of H13/J13 in-plane fracture strength

Figure 5-8 is the probability plot of the DRIE surface fracture data in a Weibull distribution with 95% confidence interval with a shape parameter of 10.28 and scale parameter of 2.237 GPa. Anderson-Darling and p-value test gave values of 0.490 and 0.220 respectively which are considered as a very good fit to such a Weibull distribution.

Accompanying the distribution parameters that have been obtained, the geometry parameter of a cantilever beam having length, width and depth of $200 \times 10 \times 15$ µm with the 1×10^{-6} radius of fillet attached to the base were considered. The DRIE characteristic area located at the both side left and right surface of the cantilever beam is 6.3×10^{-9} m^2. The mechanically polished characteristic area is the total area of the upper and lower surface and is 4.1×10^{-9} m^2. These values of characteristic area A_0 will affect the characteristic strength when applied to a structure having a different geometry or size.

In comparison as can be seen on Figure 5—10, the polished surface has a shape parameter, the Weibull modulus, smaller than the DRIE surface indicating that the polished surface has a greater scatter of fracture data. The polished surface has a scale parameter, also called Weibull strength, higher than the DRIE surfaces of about 300 MPa at failure probability equal to 0.6321. The value occurs when the failure strength σ is equal to the characteristic strength σ_0. It should be noted that the values were determined under the earlier assumption that for a test in a particular motion i.e. either in-plane or out-of-plane, there was only one flaw population distribution affecting the failure.

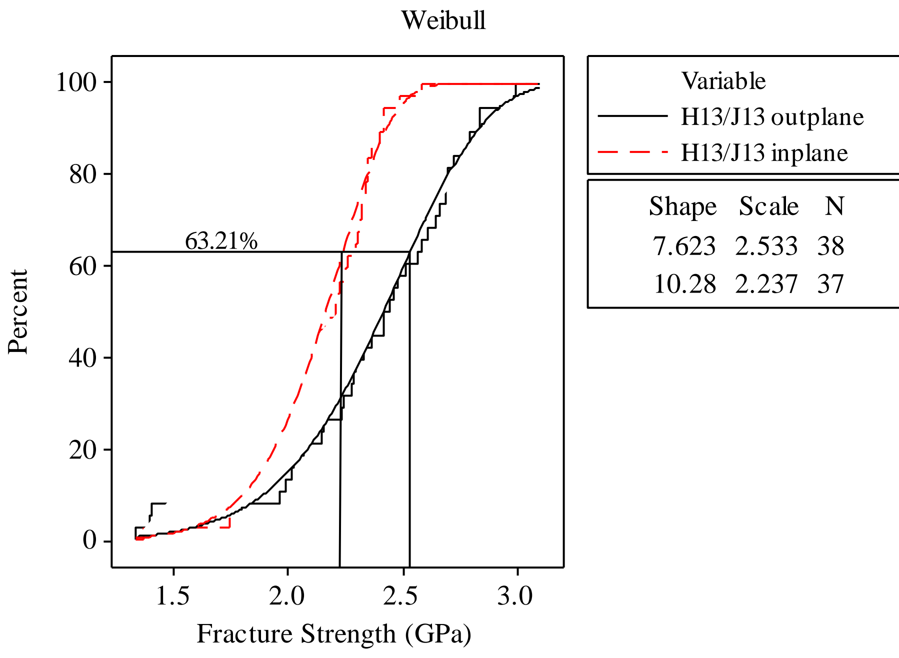

Figure 5—10: Cumulative distribution plot of both mechanically polished and DRIE surfaces from test

The above obtained Weibull fracture strengths are still in the form of characteristic strength $(\sigma_\theta)_U$ and $(\sigma_\theta)_S$ for mechanically polished surfaces and DRIE surfaces respectively. As mentioned earlier in this sub-chapter, the parameters should converted

to Weibull material scale parameters $(\sigma_0)_U$ and $(\sigma_0)_S$. The constants of the parameters relation k_U and k_S (see equation (2—73) for both surface types were determined empirically by putting the obtained characteristic strengths $(\sigma_\theta)_U$, $(\sigma_\theta)_S$ and the shape parameters m_U, m_S into the failure predictor module (see sub-chapter below for the module details). The module then was run on the postprocessing stage of ANSYS having a simulated stress condition of the same cantilever beam J13/H13 in in-plane and out of plane resonance. After that, the magnitude of the load was adjusted until a cumulative failure probability of such a structure achieved a value of 0.6321 which was a condition when the stress under interest is equal to the characteristic strength or material scale parameter (equal numerator and the denominator value in Weibull cumulative distribution function gives a probability of failure of 0.6321). The resulting stress value, if the input for the strength reference for the predictor module, that is the σ_0, is correct then the value should be of 2.533 GPa and 2.237 GPa for mechanically polished respectively. But because the value of $(\sigma_\theta)_U$ and $(\sigma_\theta)_S$ was in use, the result should be incorrect. The ratio between the resulting stress values and $(\sigma_\theta)_U$ and $(\sigma_\theta)_S$ thus can be considered as k_U and k_S. Furthermore, the $(\sigma_0)_U$ and $(\sigma_0)_S$ can be estimated by multiplying the $(\sigma_\theta)_U$ and $(\sigma_\theta)_S$ with the k_U and k_S. Such values of the parameters and constants can be seen in Table 5—2. Figure 5—11 shows the recomposed Weibull cumulative density plot using material scale parameter.

Table 5—2: The Weibull characteristic strength and material scale parameter

Surface type	σ_θ (GPa)	σ_0(GPa.m$^{2/m}$)	k
Mech. Polished → $(\cdots)_U$	2.533	1.799	0.7105
DRIE → $(\cdots)_S$	2.237	1.521	0.6801

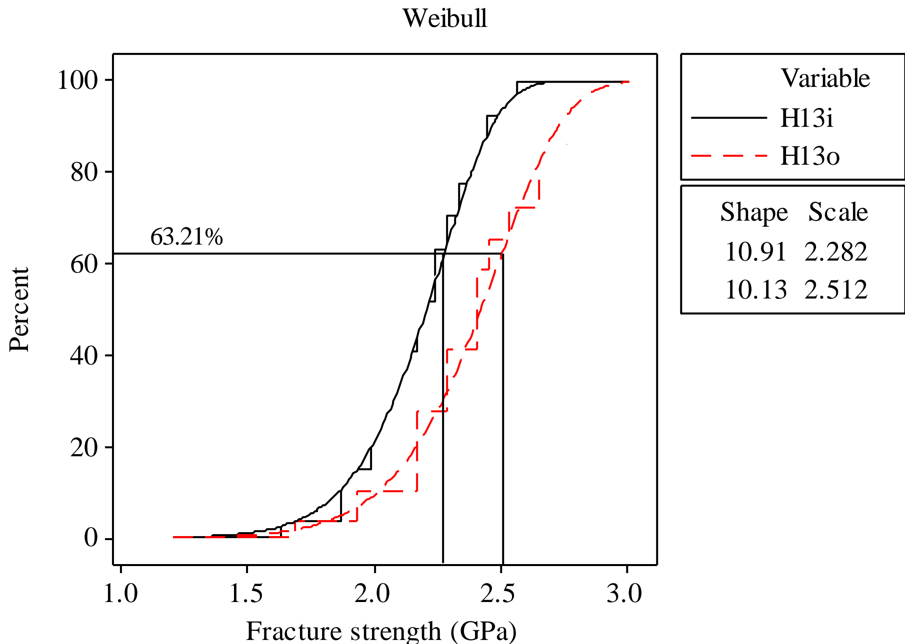

Figure 5—11: Recomposed Weibull cumulative density plot using material scale parameter

Chapter 6. Failure Prediction and method validation

This sub-chapter discuss the conditions of stress/strain that can bring a device to the possibility to fail. The discussion includes both the range of the stress/strain magnitude and prediction of the failure location on the device. The predictions were made using an APDL module specifically composed for this work that was run on a FE package ANSYS® post-processor.

The failure of the devices was predicted based on its stress distribution along the device surfaces, details of which were discussed in chapter 2.

6.1. Device model

FE models of the MEMS cantilever beams were created using ANSYS Multiphysics v.13.0. The devices were modelled using SOLID187 elements, a 3D 10-node tetrahedral structural solid with nodal translation in x, y, and z directions abilities. This element is well suited to model an irregular mesh as the model included fillets of 1µm radius at the root of the cantilever beam. The element has large deflection and large strain capabilities. The prediction algorithm was implemented using a numerical algorithm using ANSYS Parametric Design Language.

Mesh density was controlled based on typical stress distribution under the 1st and 2nd mode of vibration. Areas having a stress concentration i.e. at the root of a cantilever beam, had a denser mesh. The mesh density was controlled by dividing the feature edge line of such a structure into a desired number of components. Boundary conditions of the structure were setup by adjusting the nodes of the beam base to zero degrees of freedom. The device actuation was defined in the harmonic response analysis environment by defining the force and its frequency. A typical model of a device can be seen in Figure 6—1.

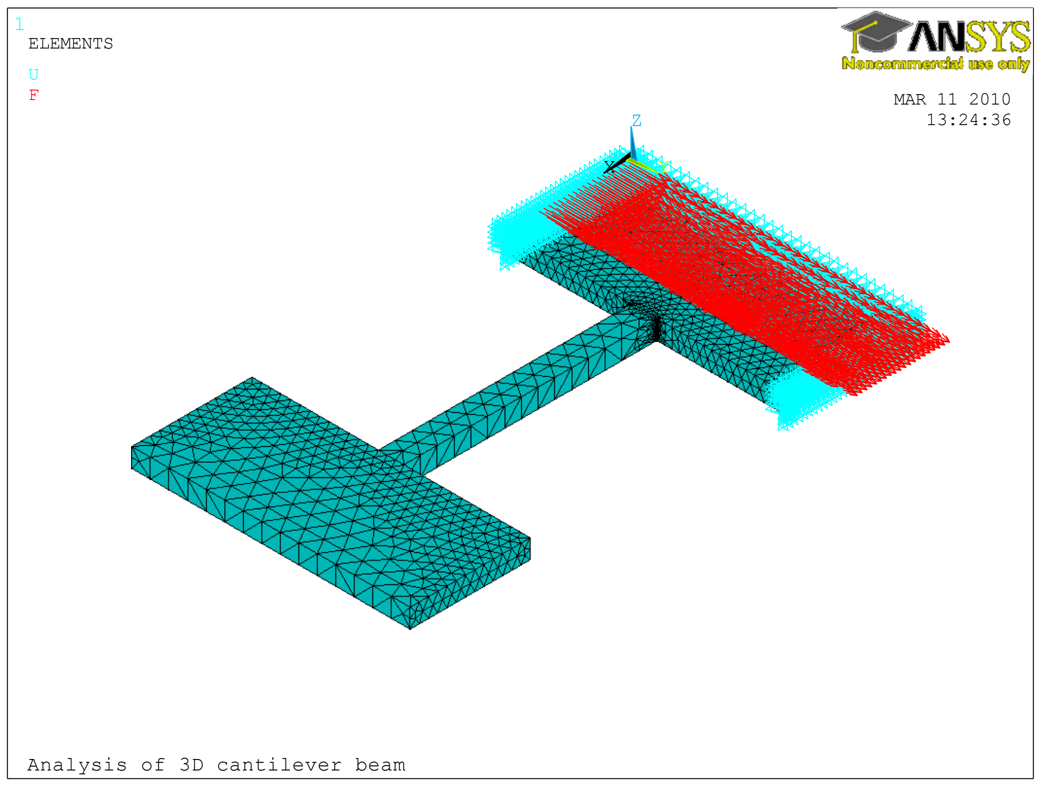

Figure 6—1: The device model, typical meshing, boundary condition (light blue) and actuation force (red).

6.2. Failure model

Failure prediction of a device f which is a probability of failure under a load condition was obtained using the numerical form of equation 2—54, 2—55, and 2—56 as follows:

$$f = 1 - \exp\left\{-\left(\sum_{u=1}^{N} \psi_{u_P} A_{u_P}\right) - \left(\sum_{u=1}^{M} \psi_{u_D} A_{u_D}\right)\right\}.$$

where ψ_u is the scalar failure probability per unit area of A_u at surface node u with N nodes number for polished surfaces and M number of nodes for DRIE surfaces.

The area A_u was defined as the area adjacent to node u as showed in Figure 6—2. As a single surface of an element at which the node u attached is shared with two other nodes, it was assumed for a single node the node u has a share of one third of such an element surface area. In ANSYS, the procedure to determine the area of a node was done by utilising extension of $*get$ function either $arnode(u)$ or $arface(e)$ function. The $arnode(u)$ gives the area at node u apportioned from selected elements attached to node u whilst $arface(e)$ returns the area of the face of element e containing the selected nodes which are associated with the node in interest u.

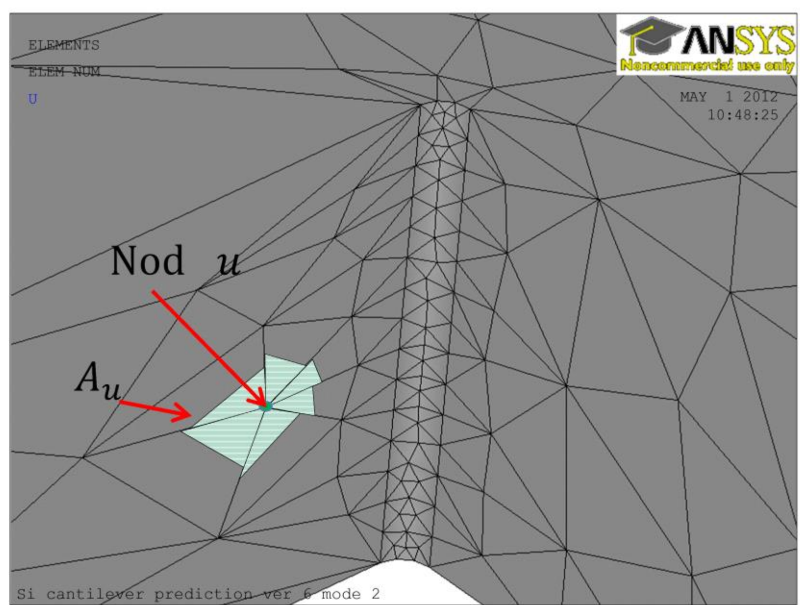

Figure 6—2: An area A_u in association with node u located on the device surface

The ψ_u was determined using a Weibull term of:

$$\psi_u = \frac{1}{A_{0_w}} \left(\frac{\sigma_{int_u}}{\sigma_{0_w}} \right)^{m_w}$$

where σ_{int_u} is the stress intensity of node u whilst σ_{0_w}, m_w and A_{0_w} are the Weibull terms of a particular surface characteristic w i.e. the polished and the DRIE surfaces, characteristic strength, shape modulus and surface area characteristic respectively.

6.2.1. Failure prediction procedure using ANSYS

Using the device model and the failure model discussed earlier in this chapter, the prediction was made based on the stress distribution simulated by ANSYS. Such a stress distribution over the surfaces of a particular device model is a response of an applied load. The failure prediction used in this experiment is based on a Weibull cumulative distribution function (CDF) that gives a single value of cumulative probability of failure (which is within 0 to 1) due to a given value of load. Thus the determination of a complete range of failure probability (from 0 to 1) of a device was made by sweeping a range of actuation load during the simulation as the probability is a function of stress. Figure 6—3 shows the predicted points as the results of the sweeping load input and then fitted to a Weibull distribution to get the parameter. The parameter is necessary in order to have a quantitative value to compare between the devices.

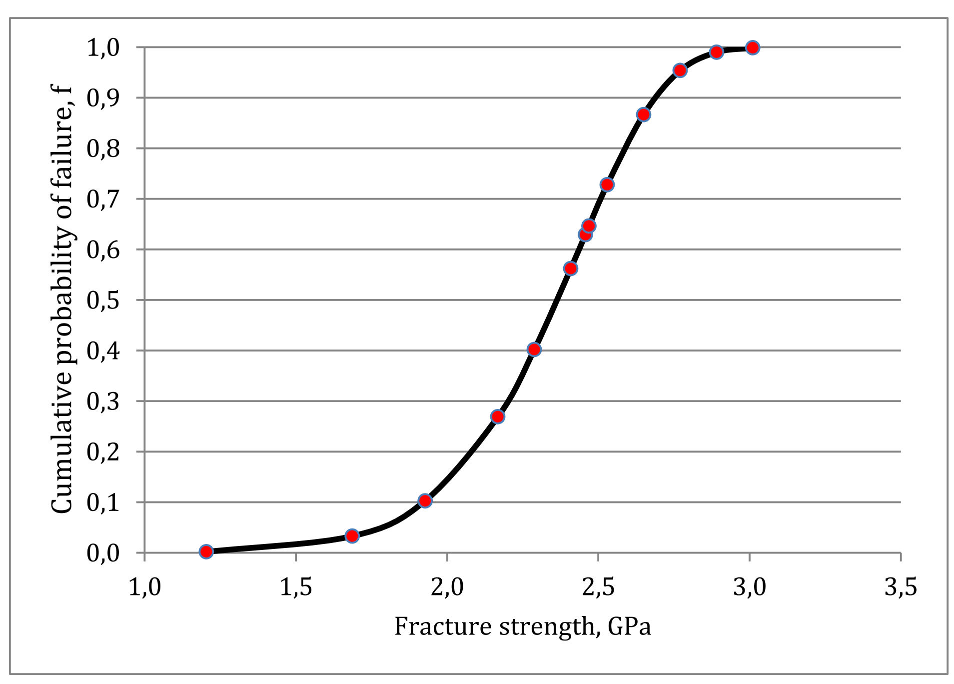

Figure 6—3: Typical predicted Weibull cumulative density of failure of a particular device

6.2.2. Failure Predictions of the Structures

The Weibull parameters were taken from H13/J13 devices which were located at sub-group IV (see Table 5—1). Thus predictions were made on sub-group I, II, and III on group H/J; The prediction and comparison were limited to only one size taken for every group. H03/J03 from group I, H02/J02 from group II, H12/J12 from group III and H13/J13 from group IV were used in this experiment. All of the devices have the same thickness of 15µm, group I and II have width of the beam of 20 µm whilst group III and IV have a beam width of 10 µm and varies about the length. The devices vary in length thus the selection was made based on the length that will give the length different about twice for groups having a same width of the beam. All of the selected devices failures were predicted in both their in-plane and out of plane resonance, except the H12/J12 devices were only predicted in its in-plane resonance as it was unable to characterise the out of plane resonance due to its high resonant frequency.

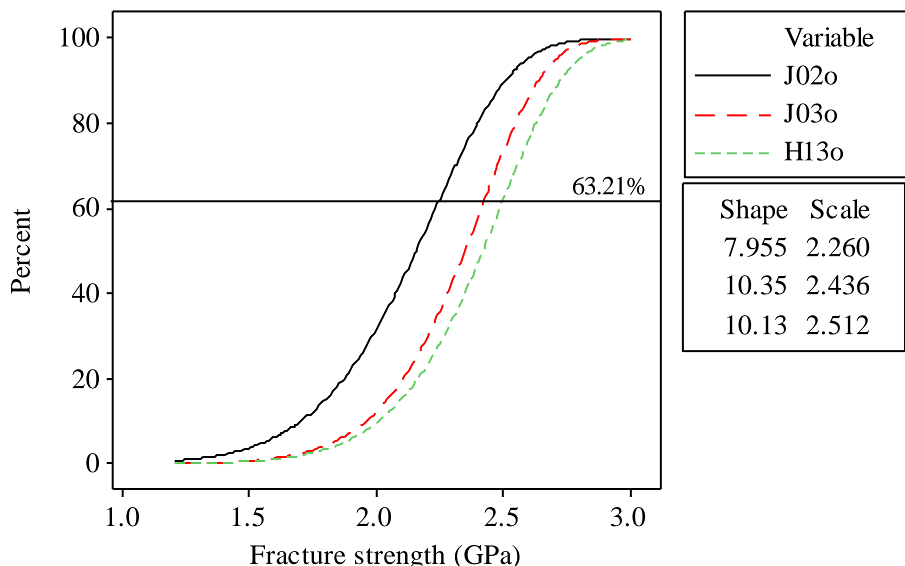

Figure 6—4: Probability of failure prediction of J02, J03 and J13 under out of plane mode

Figure 6—4 shows the comparison of the three devices under out of plane mode. J02 and J03 have a same cross section area having the same width of the beam of 20 µm with J02 twice longer than J03. H13 has a cross section area half of the two earlier mentioned having the same thickness but half the width of 10 µm. H13 has a same length of the cantilever beam of 200 µm as J03. Having the biggest size of geometry compared to the other device, J02 has the weakest fracture strength of 2.260 GPa then followed J03 of 2.436 GPa and 2.512 GPa for the smallest geometry H13. The predicted characteristic strengths show an increasing strength due to decreasing surface area. In term of the fracture data spreads, J02 shows a widest spread being compared with J02 and H13 of 7.955, 10.35 and 10.13 respectively.

Figure 6—5 describes the predicted failure under in-plane mode of the device J02, J03, H13 and J12. Area variations of side surfaces which is considered as the most affecting surface to the probability of failure of the device during the motion in this mode, are determined by only the length of the cantilever beam as the thickness for all of the devices are the same. It can be said from the graph that the wider beam devices, J02 and J03, have higher failure strength of 2.394 GPa and 2.522 GPa respectively being compared with the narrower beam devices, H13 and J12 of 2.282 GPa and 2.330 GPa respectively. And for within the devices having the same width, the shorter beam is stronger. Or it can be said the smaller the surface area considered as the most affecting

surface area during the particular motion, the stronger the device. In term of the spreads of the fracture strength, there was no obvious trend shown by the prediction results in this motion. Respectively for the devices J02, J03, H13 and J12 have shape parameter of 9.472, 9.838, 10.91, and 9.76. The smaller the shape number shows that the wider the data spreading.

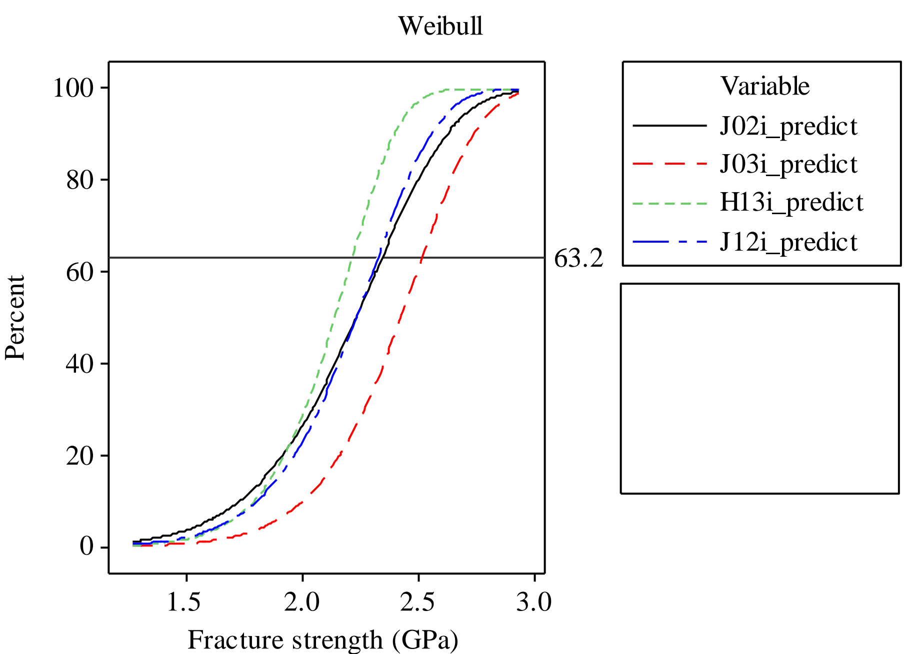

Figure 6—5: Probability of failure prediction of J02, J03, H13 and J12 in plane mode of vibration.

6.3. Validation of the prediction method

The experiments were done to validate the reliability prediction method modelled in Chapter 2. There were two predictions modelled, the fracture strength prediction, and the failure location prediction on the devices.

The predictions were made based on a Weibull distribution and the Weibull parameters that represent the surfaces properties are required. As mentioned in Chapter 3, due to the fabrication processes of the devices, two types of surfaces having a different surface roughness are involved, mechanically polished and DRIE. Thus it can be said that the device structure has a compound flaw distribution. Under such a condition, all flaw populations are present concurrently and are competing with each other to cause failure. Thus there were two sets of Weibull parameters obtained to represent the device structure surface properties in terms of its fracture strength scatter. The cantilever beams were fractured under in-plane motion to characterise the DRIE surfaces and out-of-plane to

characterise the mechanically polished surfaces. The stress at which each test specimen failed was recorded. The resulting failure stress data were used to obtain the Weibull parameters that are associated with the underlying flaw population distribution, i.e. the surface roughness.

Justification to the prediction methods were made by bringing various different geometries of devices to fail. The fracture strength and the rupture locations from these tests were collected to obtain their failure characteristic. Both fracture strength and rupture locations were presented using Weibull distribution terminology. Comparisons between the reliability prediction models and the failure characteristic of the devices validate the method.

6.3.1. Approach

It was also possible when the fracture test was implemented by vibrating the cantilever in in-plane or out-of-plane direction that a multiple competing or concurrent flaw population was in effect i.e. the upper-lower surface flaws characteristic and sidewalls surface characteristic. It was expected when the cantilever beam was actuated in in-plane the most affecting surface characteristic is the lower/upper surface and vice-versa. A fractography technique that can be use to approximate the initial failure surface can be used to distinguish which surface flaw characteristic was the dominant flaws characteristic to the particular fracture [82]. The fractography technique can be done for all ruptured devices after fracture tests using SEM but that was considered to be impractical due to the number of the samples.. However, SEM images were taken in this work for several samples to gain a better insight of which fracture mechanism occurred during the fracture tests.

6.3.2. Fracture strength

Fracture tests were done by increasing the load step by step whilst the strain was characterised using the Raman system and displacement reading. The increasing load was achieved by increasing the sinusoidal supply voltage at the device's resonant frequency.

Plots of fracture strength distributions below include H13/J13, J02 and H12 which represent the Weibull parameter reference, the biggest geometry group available in dies, and the smallest group respectively. Devices nomenclature of geometry and mode are available from Table 3—3 and Table 5—1. The plots show the comparison between devices geometry related to its size and surface characteristic. It can be seen by comparing the reference with the test device.

The accuracy of the prediction can also be seen from the same plots by comparing the measured fracture strength distributions with the prediction.

6.3.2.1 Fracture strength: in-plane

Figure 6—6 presents the plots predicted cumulative failure distribution compared with the test results of devices J02 and J03 in in-plane mode. Comparing the distribution profiles of J02 devices, it was predicted to have a modulus of 7.443, yet the test results showed more scattered fracture data of 7.385. At 63.2% cumulative failure distribution, fracture strength was expected to be 2.343 GPa instead of 2.120 GPa obtained from the test. A characteristic failure discrepancy of 223 MPa or about 10% lower than predicted strength occurred. For J03 devices, the spread of the data was expected to display a scatter of 9.838 instead of showing a narrower scatter of 9.050 with characteristic strength discrepancy of 141 MPa or about 6% lower than prediction.

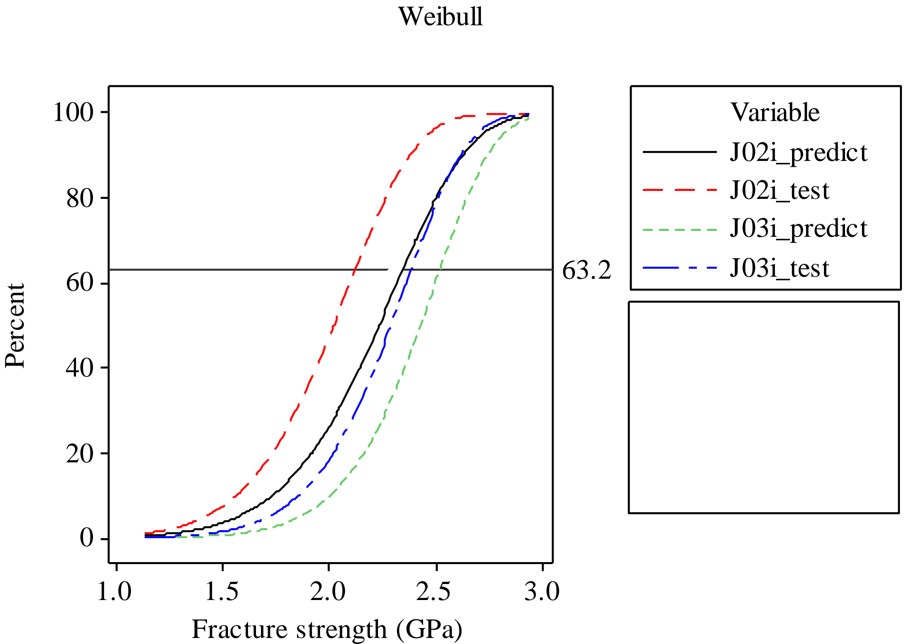

Figure 6—6: Plot of predicted and tests results cumulative failure distribution of J02 and J03 in in-plane mode

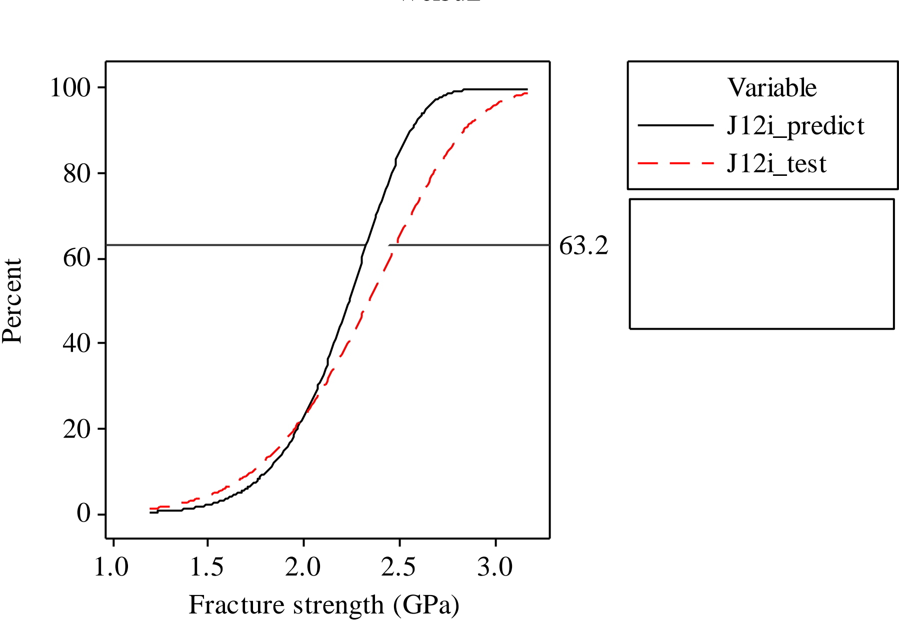

Figure 6—7: Plot of predicted and test results for cumulative failure distribution of J12 in in-plane mode

Figure 6—7 was taken from J12 devices breaking in their in-plane mode. The devices were included in group III having the smallest geometry group with highest resonance frequencies within the dies. These devices were available for the motion characterisation in in-plane mode only utilising visual observations. These devices have the most scattered data point from the test of 6.256 being compared with other devices available on the dies. Higher characteristic fracture strength occurred than predicted by 148 MPa or about 6%.

6.3.2.2 Fracture strength: out of plane

The out of plane fracture strength of J02 and J03 devices were plotted in Figure 6—8. For J02 devices, there was a 57 MPa characteristic strength difference or about 3% stronger between predicted of 2.260 GPa and test result of 2.317 GPa. The data from the test scattered at 8.456 which is a bit narrower than the predicted 7.955. For J03 devices, a characteristic strength of 2.436 GPa was predicted but tests gave a characteristic strength of 2.214 GPa which is about 222 MPa or 10% weaker than predicted.

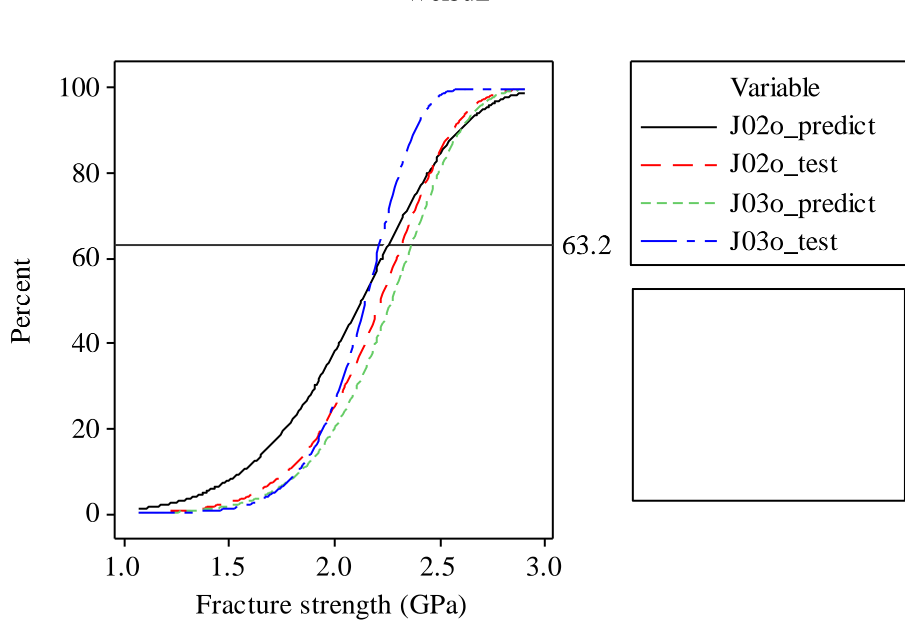

Figure 6—8: Plot of predicted and tests results of cumulative failure distribution of J02 and J03 in out of plane mode

6.3.3. Rupture position

Rupture position of the devices were heavily scattered over the cantilever beams length as shown in Figure 6—9 which were taken from a light microscope camera. Visual observations were used to measure the ruptured beams relative to the root. Figure 6—10 plots the relative rupture position of the beams measured from its root of group I-II devices having 20µm beam width and group III-IV devices having 10 µm beam width (see Table 3—3 for device geometry and Table 5—1 for device grouping). As the plotted data were collected from different sizes, the position label is normalised as (x/L). Where L is the length of the cantilever beam measured from its clamped end to its end without the mass whilst x is the distance of the rupture location measured from the root of the beam.

From the prediction made in chapter two that can be seen graphically in figure 2.4, the rupture distribution should peaking at the root of the cantilever beam which is far different being compared to the observation results shown in Figure 6—10 which were peaking at a non-root position.

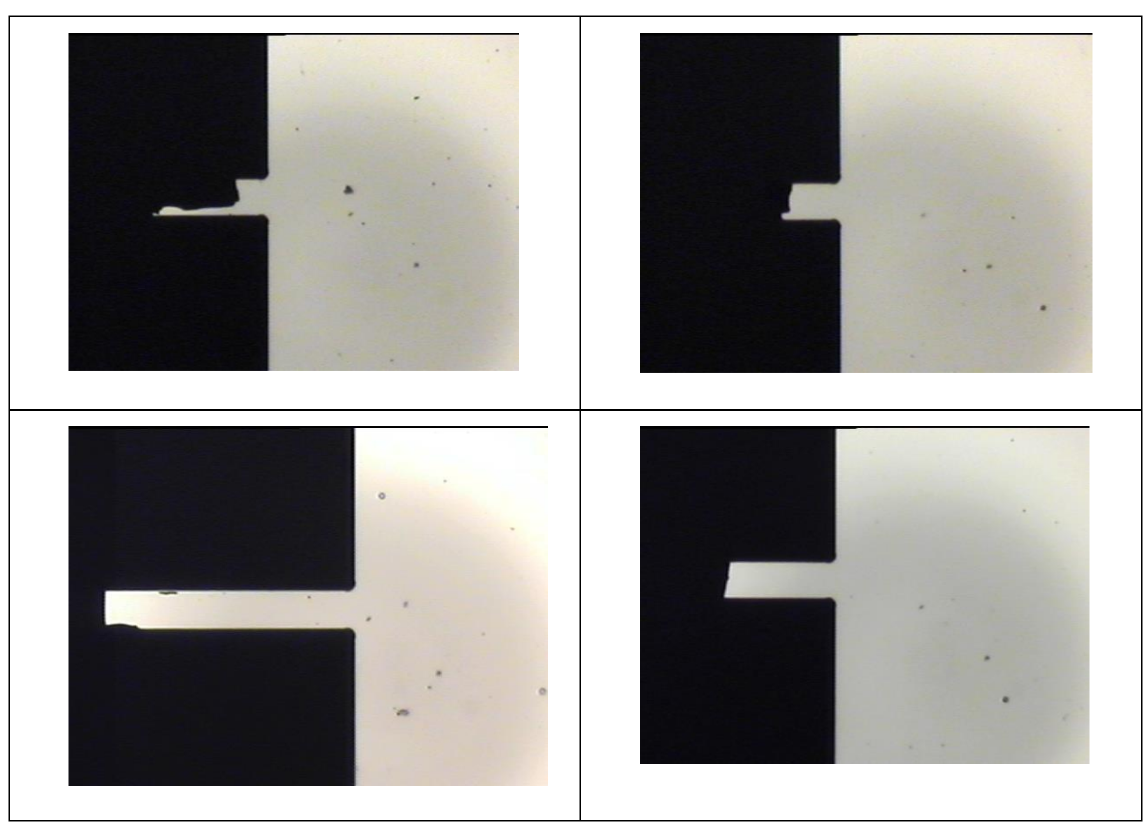

Figure 6—9: Scattered failure locations along the beam. The beam width is 10μm with beam length vary from 180μm to 220μm

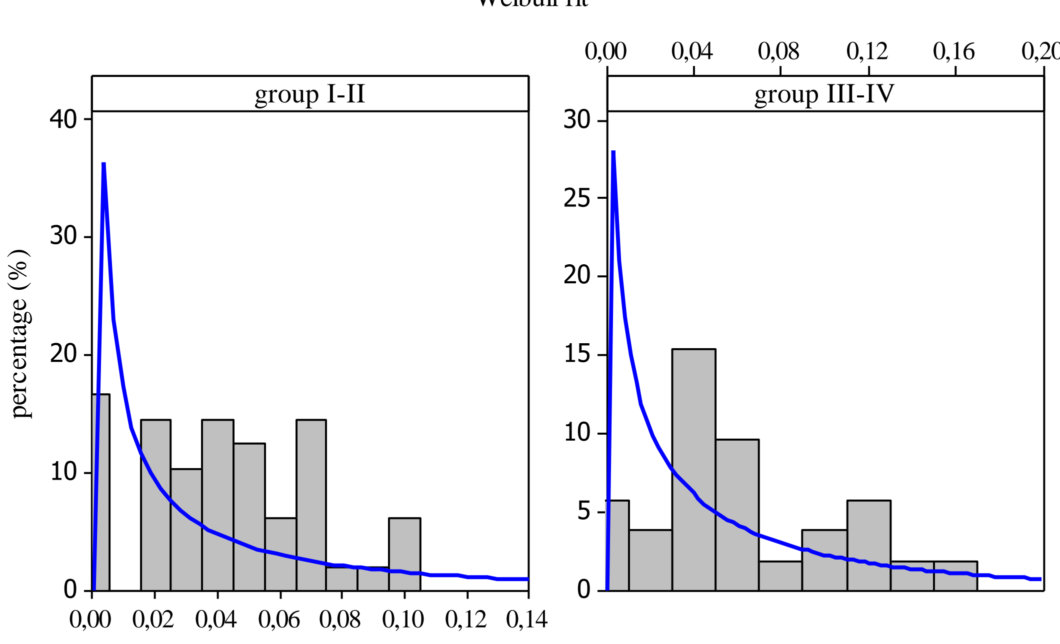

Figure 6—10: Weibull fitted rupture position of the cantilever beam devices measured relative from the root as $\left({}^{x}/_{L}\right)$

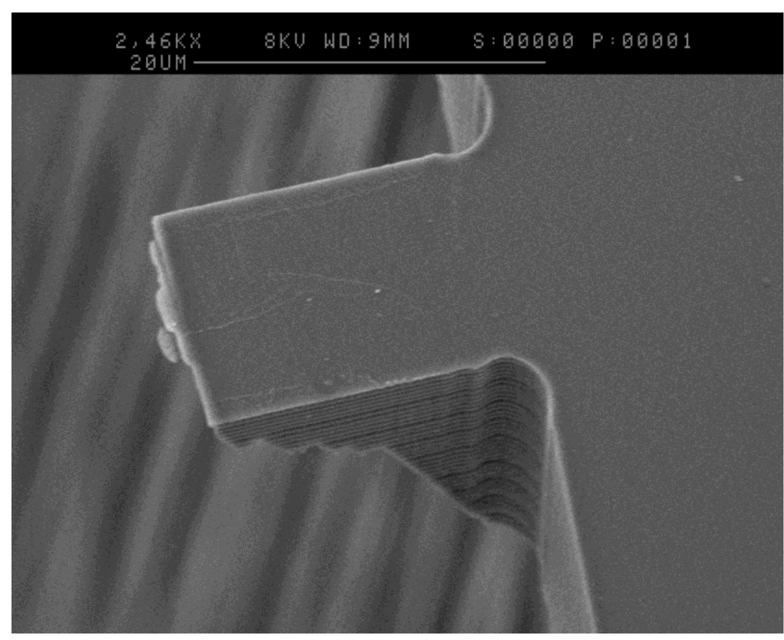

Figure 6—11: SEM image shows root rupture and propagated through [111] giving about 15um remaining

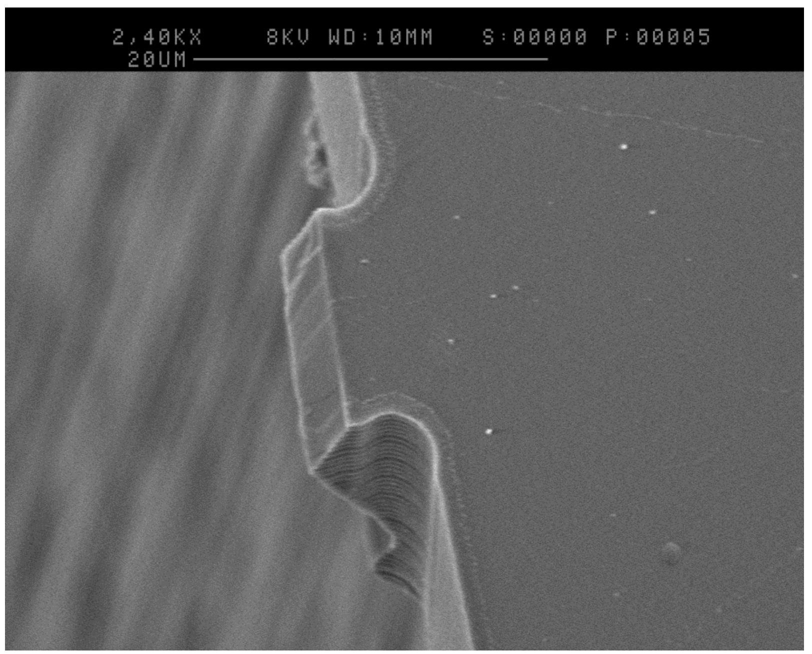

Figure 6—12: SEM image shows root ruptured and propagated through [111]

Figure 6—11 and Figure 6—12 show the SEM imaging about the rupture position. The first SEM image shows a beam remainder of about 5μm from the root of a 200 μm length cantilever beam. When plotted in Figure 6—10, such a cantilever beam will be positioned at 0.975 on the horizontal axis group III-IV plot whilst the beam which was ruptured at the root in SEM Figure 6—11 will be positioned at 1.00.

Thus from SEM images and the statistical plot of failure position distribution, we can consider that even though the beam appears to have ruptured at a distance from the root under microscope camera observation, the failure in most cases initiates from the root. The SEM images also shown that the ruptures propagated in the [111] direction which is known as the cleavage plane of the (100) single crystal silicon material.

Chapter 7. Discussion of Results

This chapter discusses the usefulness of the methods being used to predict the reliability of MEMS devices. There were factors affecting the accuracy of the method i.e. assumptions taken to simplify the work, the mathematical model in use, measurement equipment, and measurement methods. The discussion starts by evaluating the discrepancies between prediction and test to justify the usefulness of the method.

Further a discussion on the strengths and weaknesses of the method being used in this work follows.

7.1. The usefulness of the method

The prediction method in this work was coded into an APDL (Ansys Parametric Design Language) program executed in the postprocessor stage during a dynamic loading simulation procedure in Ansys. Descriptions of reliability predictions, or conversely failure predictions, of a series of MEMS devices was done and experimentally validated in chapter 6.

The accuracy of the method is evaluated by comparing the predictions and test results. Comparison was also made with commonly known failure tendencies related to single crystalline silicon or advance ceramic, such as size effect and surface roughness, although care has to be taken as they are not always applicable due to the existence of non-uniform stress distribution and stress concentration.

MEMS devices, which generally have multiple surface characteristics, typically contain multiple flaw distribution. Competing failure between primary and secondary surface may be an issue when the secondary surface significantly contributes to the failure, which was assumed to be obtained from the primary surfaces. Moreover, if the prediction accuracy, being compared to the test results, is poor, a data censoring procedure can be implemented to suspend outlier data. Fractography, by observing the surface pattern of ruptured samples from SEM imaging, is usually incorporated to identify the fracture origin surface to validate the data.

SEM images were incorporated in this experiment to observe the rupture details related to rupture position with respect to the root of the cantilever beam.

7.1.1. The failure predictions related to the size

Predictions of the failure strength of different size of devices were made based on a Weibull distribution. The H13/J13 devices were selected and ruptured to obtain the

Weibull characteristic failure strength parameter σ_θ which was then converted to material scale parameter σ_0 suitable for the prediction parameter of different device sizes.

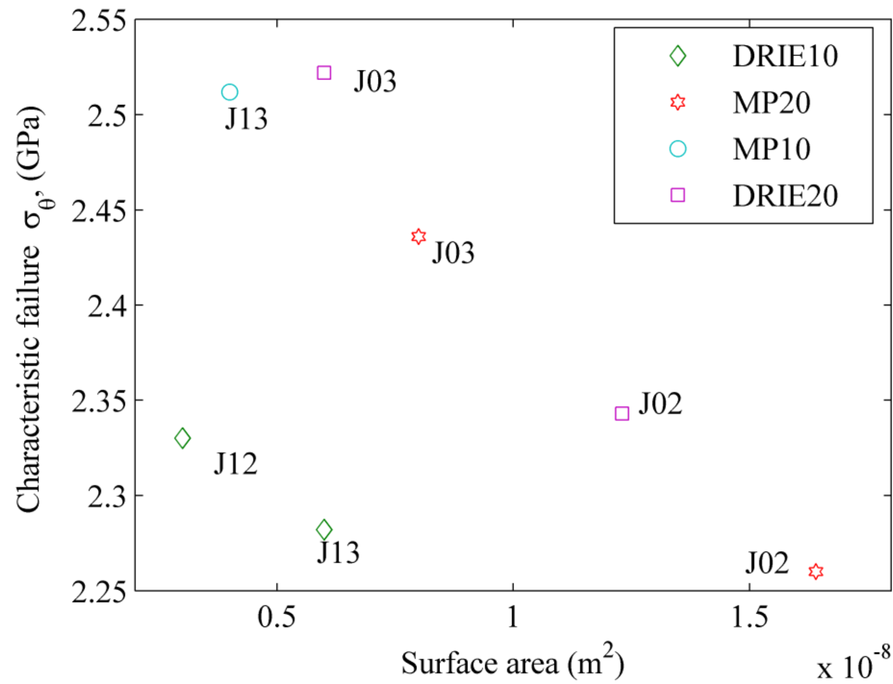

Figure 7—1: Predicted failure strength characteristic related to device surface area.

Figure 7—1 shows the effect of surface area size to the failure characteristic strength of the devices. DRIE10 and DRIE 20 mentioned in the legend of the graph are related to etched surface of the devices having the beam width of 10μm and 20μm respectively whilst MP10 and MP20 were the same but for mechanically polished surfaces.

It can be seen from the graph that for an increasing surface area within the same group (i.e. having the same beam width), the characteristic failure strength was consistently decreasing for all devices with a gradient between -2.8×10^7 to -1.6×10^7. The decrements were because of the size effect implemented due to its consideration in the Weibull failure strength distribution function as can be seen in equation (2—26) under volume consideration or equation (2—27) under surface area consideration with V/V_0 or A/A_0 being the ratio between volume or area of the structure of interest and the reference structure. In this work, H13/J13 structures were used for the reference structures, see Table 3—3 for device geometry and Table 5—1 for device grouping.

7.1.2. The failure predictions due to surface type

Figure 7—2 uses the same data plot as Figure 7—1 but graph compares the failure data of different surface types, i.e. polished surface and etched surface from the same device.

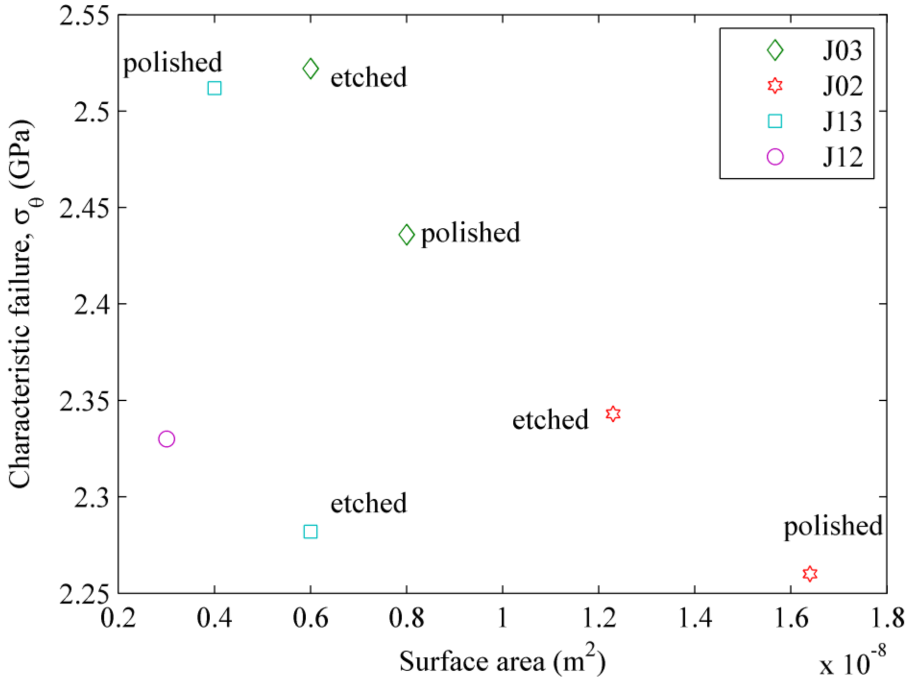

Figure 7—2: Relation of characteristic failure strength and surface type of every devices

J02 and J03 devices show that etched surfaces were stronger than the polished surfaces whilst J13 suggests otherwise. Theoretically, based on the surface type i.e. surface roughness (surface roughness of such devices used in this work can be seen on Figure 5—1 and Figure 5—2 for polished and etched surface respectively), a mechanically polished single crystalline silicon surface having a finer surface roughness has a higher material scale parameter compared with the DRIE surfaces. A rougher surface is considered to have a higher concentration of flaws and therefore has a higher probability of failure under the same level of load. This is contrary to whole J02 and J03 suggest. A possible explanation is that the size effect has a more dominant influence than surface roughness. Using this consideration the failure tendency for all devices was consistent for J02 and J03. For individual J13, both the size effect and surface roughness consideration are applicable yet it is not compatible with J02 and J03 results as such a device has a different beam width from a different group.

7.1.3. Data scatter prediction due to surface type

Shape parameter or Weibull modulus m, indicates the scatter degrees of fracture strength over a range of a distribution. Lower m value indicates a greater scatter of data. Figure 7—3 shows the scatter degrees of the devices.

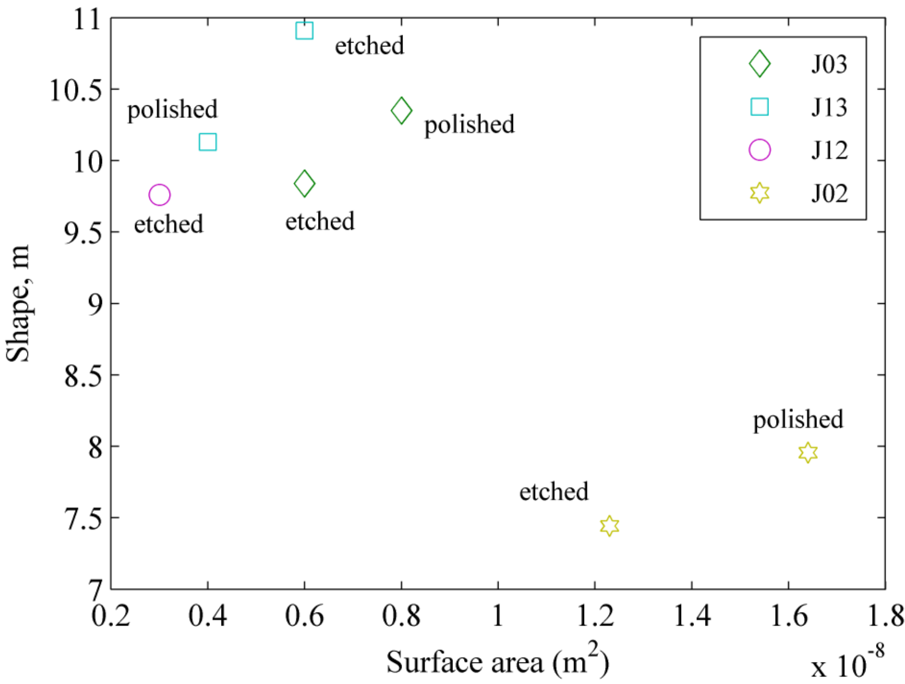

Figure 7—3: Fracture data scatter of the devices

Generally, a mechanically polished surface of single crystalline silicon is considered to have a greater scatter of fracture data being compared with a DRIE surface. This is applicable to J13. But such a consideration is inapplicable to J02 and J03 where the etched surfaces have a greater scatter than the polished surfaces.

J02 data were more scattered than the others. It was possible that outliers were involved in J02 data to increase the data scatter. Unfortunately, it is difficult to conclude that a particular data is a outlier because it is also possible that such a data is a representation of an extreme condition of such a sample.

Additionally, there is no quantified relation available that relates the surface roughness with the degree of data scatter. The data scatter is fully determined from experiment.

7.1.4. Failure location distribution

Failure location distribution was discussed in sub-chapter 6.3.3 showing the discrepancy between predicted location distribution showed in Figure 2—4 and from tests observations showed in Figure 6—10. SEM imaging was incorporated to justify the

light microscope camera observation showing the non-root rupture position distribution. The SEM imaging show that the failure which was considered to be a rupture at a distance from the root, was actually a rupture originating from the root and propagating along the [111] plane. For a [001] wafer used in this experiment, the [110] planes are the preferable cleavage planes. However, the [111] planes are found at an angle of 54.75° to the surface of the wafer and have the same number of atomic bonds of 1.22×thickness on its plane. Considering such a plane, if the beam ruptures at the root and propagates along [111] planes the remainder beam length is about 3.5 μm observed from the top. Therefore, by implementing the [111] cleavage plane consideration, the previously considered non-root root peaking distribution actually is a root peaking distribution. Thus, the failure location prediction procedure gives a good prediction. However, as the SEM imaging was only done on only a small sample. There was no quantification available for failure location distribution.

7.1.5. Analysis of prediction and test results discrepancy

Figure 7—4 shows the percentage error of all devices being evaluated during the experiment. It was found that the biggest discrepancy available from this experiment between the predicted and test result is up to 10% which quantifies as223 MPa.

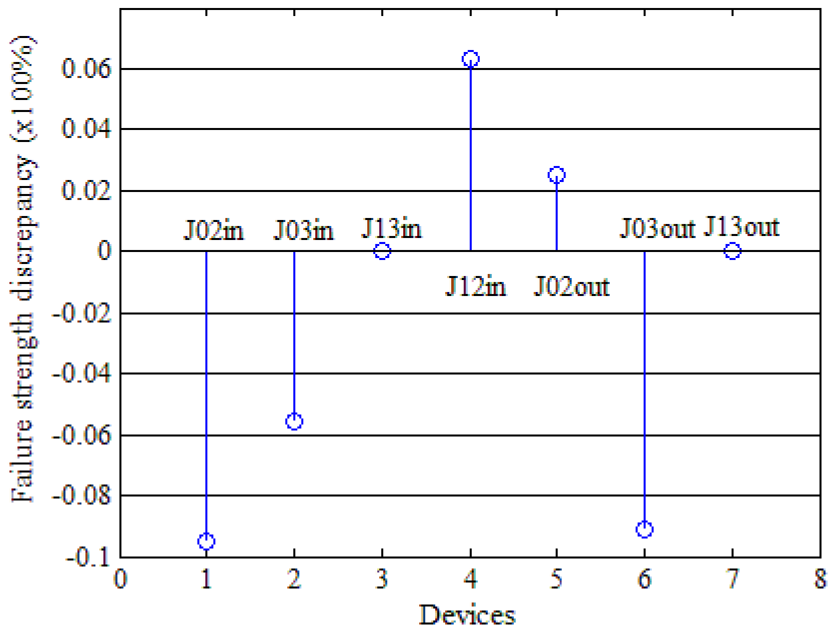

Figure 7—4: Discrepancies of the predicted devices failure strength and test results.

The discrepancies were non-systematic; there was no particular tendency to be seen. Overestimate prediction in which the test results were about -6% to-10 % lower than

expected was seen for devices number 1, 2 and 6 which stand for group I devices having 20µm width of beam structure. But such a consideration was inapplicable for J02, which comes from the same group, which showed an error about 2% higher than the prediction. Thus the errors can be treated as fully random and ranged from 6% to -10%. The errors level achieved by this work can be considered as a good prediction being compared to the results of other researchers [15].

7.2. Contributing errors

The error level shown by the method is possibly due to other features of the experiments. The effects of these contributing errors were not always recognised or measureable.

7.2.1. Assumptions and mathematical models

It was assumed that the material fracture strength of brittle solid depends critically on the flaw population. This assumption was introduced by Griffith [22] to justify that the real materials showed rupture strengths two orders of magnitude lower compared to an ideal solid of such a material. It is impossible to quantify the flaw population over a sample thus the material fracture strength were determined statistically rather than deterministically. As the nature of a statistical determination, characterisation of a population is usually done by tests over a series of samples. A contributing error can arise from this procedure as the samples are not always 100% representative of the population characteristic. Thus, a discrepancy of test results taken from the same population is common. To reduce the effect, sampling should be done over a larger number. The number of samples taken in this experiment vary between 27 and 38 samples for every type of ruptured device with all the rupture data in use without any outliers censoring.

It was also assumed that the failure occurred under a steady state condition of the structure during the dynamic load which excludes consideration of other effects on changing the condition of the structure characteristics such as fatigue, creep, strain rate dependence or stress gradient dependence. Thus by taking this assumption, the strength weakening of sample devices during a test was still treated as a valid representation of the population and will be included to the data. This inclusion (if the value is weaker than the true data) will directly weaken the failure strength characteristic σ_θ and extend the spread of the distribution, thus reducing the value of the shape modulus m.

7.2.2. Measurement methods and equipment

All of the failure strength characterisations were directly measured using dynamic Raman spectroscopy during the dynamic loading. Calibration of this measurement method, discussed in sub-chapter 4.5.4 and seen on Figure 4—7, shows errors of up to ±50 MPa, which is about 2.5%, when utilised to measure a level stress around 2 GPa in this experiment. Thus, a 50MPa resolution of measurement is acceptable. The Raman system equipment also showed a shifting behaviour of the peak position of the silicon crystalline during measurement, but these errors were overcome by continuously compensating the shift using a reference spectrum from a Ne bulb.

The Raman characterisation used the [001] Raman geometry (discussed in sub-chapter 4.2.1) which is preferable for [100] silicon wafer utilisation. In this geometry, both incident and collected backscattered light are polarised along [100], thus only the longitudinal LO_z peak is observed. This Raman geometry means that only parts of the strain/stress components can be characterised.

Chapter 8. Conclusion

8.1. Conclusion of the work

The aim of this work was to develop a prediction method exploiting the advantages and taking account limitations of dynamic Raman spectroscopy. The work is predominantly focused on reliability prediction of MEMS devices.

The method was developed and implemented to predict the performance of a series of devices by predicting its failure and comparing with the fracture test of such samples. Discrepancies were found at a tolerable level from which is can be concluded that the method is reliable to be used in the field of reliability prediction of MEMS devices.

The cause of such discrepancy was discussed and techniques to improve the reliability of the method are proposed for a future work discussed in sub-chapter 8.2 below.

The development of the method and its experimental validation was highly affected by the reliability of the data which was directly taken from the measurements, estimated from other available data or analytically calculated. In general, evaluation to assure the reliability of the data was made by comparing the data from a different procedure. As measurement results of a standardise and certified measurement equipment, the data can be considered as reliable. However, care has to be taken as the equipment usually has conditions that have to be met to assure that it delivers a reliable measurement result. The Zygo profiler, the Polytec laser vibrometer and the Horiba Jobin-Yvon Raman spectroscopy are certified measurement equipment, yet specific handling is necessary to have a reliable measurement result. An additional calibration technique has been added to the Raman setup, the utilisation of a Neon bulb to overcome its measurement shifting.

8.2. Future Work

An implementation of off-axis Raman spectroscopy was reported by Loechelt [75] that enables the characterisation of the complete tensor nature of stress fields under static loading of a 4 inches [100] silicon wafer. The technique utilises a combination of a tilted incident light from the normal axis (tilted from [001] direction) with polarisation of the incident light and collected backscattered light. Using such a technique, any Raman-active optical phonon mode can be selectively observed.

The technique can be implemented to the dynamic Raman spectroscopy to improve the capability of both techniques. Yet, as far as the author knows, there was no publication reporting the utilisation of the off-axis technique combined with the dynamic Raman spectroscopy to characterise all components of the stress tensor during a dynamic load.

A direct characterisation of all components of the stress tensor during a dynamic load condition will help to understand the failure mechanism and eventually help to improve the design of reliable MEMS components.

The reference sample H13/J13 is an almost identical structure geometry compared with the structure of the samples being predicted with a variation of the size and size ratio only which was considered as a good experimental design for limiting the variable. Yet in terms of statistical data reliability related to the surface characterisation, an issue of a possibility of competing failure due to different surface types in a single sample exists. Hence the characterisation of a single type of surface by rupturing such a sample in its in-plane or out of plane resonance may be mixed or swapped with the other surface. Thus additional samples having a single type of surface obtained from the same microfabrication process may help to isolate the possibility of outlier data. Another method to isolate the competing failure is to make use of SEM imaging and perform a fractography evaluation to identify the initiating rupture surface for every sample.

Statistical fracture data in this work were taken by rupturing between 27 and 38 devices for every type of device that if there were no competing failure included to the data, unbiasing factors for the maximum likelihood estimate of the Weibull modulus span between 0.951 to 0.964. Improvement to this unbiasing factor to 0.987, which will give a very confident interpretation of data tendency, needs a number of samples of 100. The unbiasing factors for such an estimator was taken from table 1 ASTM C1239[82].

There were four groups I, II, III and IV of devices having four different length of beam and two different width of 20μm for groups I and II and of 10μm for group III and IV, used to characterise the effect of different size of device structure. When H13/J13 was used as a reference, there was one group has a lower size and two groups have greater sizes, so it was difficult to introduce a tendency by comparing due to the number of comparable data. A variation of 7 different lengths and 3 different widths of cantilever beam should give a better representation of the physical aspects and its failure tendencies.

References

1. Spinner, S., et al. *A system for electro-mechanical reliability testing of MEMS devices*. 2006.

2. Neels, A., et al., *Reliability and failure in single crystal silicon MEMS devices.* Microelectronics Reliability, 2008. **48**(8-9): p. 1245-1247.

3. Yoo, B.W., et al. *Reliability-based characterization of single crystalline silicon micromirrors for space applications*. 2009.

4. Hsu, W.T. *Reliability of silicon resonator oscillators*. 2007.

5. Jayatilaka, A.D.S. and K. Trustrum, *Statistical approach to brittle fracture.* Journal of Materials Science, 1977. **12**(7): p. 1426-1430.

6. Jones, P.T., G.C. Johnson, and R.T. Howe. *Statistical characterization of fracture of brittle MEMS materials*. 1999.

7. Jadaan, O.M., et al., *Probabilistic Weibull behavior and mechanical properties of MEMS brittle materials.* Journal of Materials Science, 2003. **38**(20): p. 4087-4113.

8. Weibull, W., *A statistical theory of the strength of materials*. Vol. Rept. 151. 1939: Royal Swedish Academy of Engineering Sociences. 45.

9. Chasiotis, I. and W.G. Knauss, *The mechanical strength of polysilicon films: Part 2. Size effects associated with elliptical and circular perforations.* Journal of the Mechanics and Physics of Solids, 2003. **51**(8): p. 1551-1572.

10. Bosseboeuf, A. and S. Petitgrand, *Characterization of the static and dynamic behaviour of M(O)EMs by optical techniques: Status and trends.* Journal of Micromechanics and Microengineering, 2003. **13**(4): p. S23-S33.

11. Hedley, J., et al. *Mode shape and failure analysis of high frequency MEMS/NEMS using Raman spectroscopy*. in *3rd IEEE International Conference on Nano/Micro Engineered and Molecular Systems, NEMS 2008, January 6, 2008 - January 9, 2008*. 2008. Sanya, China: Inst. of Elec. and Elec. Eng. Computer Society.

12. Anastassakis, E. and E. Liarokapis, *Polycrystalline Si under strain: Elastic and lattice-dynamical considerations.* Journal of Applied Physics, 1987. **62**(8): p. 3346-3352.

13. Xue, C., et al., *A dynamic stress analyzer for microelectromechanical systems (MEMS) based on Raman spectroscopy.* Journal of Raman Spectroscopy, 2007. **38**(4): p. 467-471.

14. Hu, Z.X., et al., *Dynamic characterization of MEMS using Raman spectroscopy.* Journal of Micromechanics and Microengineering, 2008. **18**(9).

15. Fitzgerald, A.M., et al., *A general methodology to predict the reliability of single-crystal silicon MEMS devices.* Journal of Microelectromechanical Systems, 2009. **18**(4): p. 962-970.

16. Man, K.F. *MEMS reliability for space applications by elimination of potential failure modes through testing and analysis*. 1999.

17. Diemar, *Determination of local characteristics for the application of the Weakest-Link Model.* 2005.

18. Rinne, H., *The Weibull Distribution: A Handbook*. 2010: Taylor & Francis.

19. Murthy, D.N.P., M. Xie, and R. Jiang, *Weibull Models*. 2004: Wiley.

20. Weibull, W., *A statistical distribution function of wide applicability.* Journal of Applied Mechanics, 1951. **18**(3): p. 5.

21. Chen, K.-S., A. Ayón, and S.M. Spearing, *Controlling and Testing the Fracture Strength of Silicon on the Mesoscale.* Journal of the American Ceramic Society, 2000. **83**(6): p. 1476-1484.

22. Griffith, A.A., *The phenomena of rupture and flow in solids.* Philos. Trans. R. Soc. London, 1920. **221**: p. 163-198.

23. Petersen, K.E., *Silicon as a Mechanical Material.* Proceedings of the IEEE, 1982. **70**(5): p. 420-457.

24. Rice, R.W., *Fracture Topography of Ceramics.* 1974: p. 439-472.

25. Wilson, C.J., A. Ormeggi, and M. Narbutovskih, *Fracture testing of silicon microcantilever beams.* Journal of Applied Physics, 1996. **79**(5): p. 2386-2393.

26. Namazu, T., Y. Isono, and T. Tanaka, *Evaluation of size effect on mechanical properties of single crystal silicon by nanoscale bending test using AFM.* Journal of Microelectromechanical Systems, 2000. **9**(4): p. 450-459.

27. Tsuchiya, T., et al., *Specimen size effect on tensile strength of surface-micromachined polycrystalline silicon thin films.* Journal of Microelectromechanical Systems, 1998. **7**(1): p. 106-113.

28. Nemeth, N.N., et al., *Fabrication and probabilistic fracture strength prediction of high-aspect-ratio single crystal silicon carbide microspecimens with stress concentration.* Thin Solid Films, 2007. **515**(6): p. 3283-3290.

29. Boyce, B.L., et al., *Strength distributions in polycrystalline silicon MEMS.* Journal of Microelectromechanical Systems, 2007. **16**(2): p. 179-190.

30. Ericson, F., S. Johansson, and J.Å. Schweitz, *Hardness and fracture toughness of semiconducting materials studied by indentation and erosion techniques.* Materials Science and Engineering, 1988. **105-106**(PART 1): p. 131-141.

31. Wilson, C.J. and P.A. Beck, *Fracture testing of bulk silicon microcantilever beams subjected to a side load.* Journal of Microelectromechanical Systems, 1996. **5**(3): p. 142-150.

32. Loudon, R., *The Raman effect in crystals.* Advances in Physics, 1964. **13**(52): p. 423-482.

33. Maradudin, A.A., S. Ganesan, and E. Burstein, *Use of morphic effects for the study of vibrational and optical properties of impurity atoms in crystals.* Physical Review, 1967. **163**(3): p. 882-895.

34. Smith, E. and G. Dent, *Modern Raman Spectroscopy: A Practical Approach*. 2013: Wiley.

35. Narayanan, S., S.R. Kalidindi, and L.S. Schadler, *Determination of unknown stress states in silicon wafers using microlaser Raman spectroscopy.* Journal of Applied Physics, 1997. **82**(5): p. 2595-2602.

36. Anastassakis, E., et al., *Effect of static uniaxial stress on the Raman spectrum of silicon.* Solid State Communications, 1970. **8**(2): p. 133-138.

37. Anastassakis, E., *Strains and optical phonons in material systems.* Acta Physica Hungarica, 1994. **74**(1-2): p. 83-105.

38. Ganesan, S., A.A. Maradudin, and J. Oitmaa, *A lattice theory of morphic effects in crystals of the diamond structure.* Annals of Physics, 1970. **56**(2): p. 556-594.

39. Loechelt, G.H., N.G. Cave, and J. MenÈndez, *Measuring the tensor nature of stress in silicon using polarized off?axis Raman spectroscopy*. Vol. 66. 1995: AIP. 3639-3641.

40. Bonera, E., M. Fanciulli, and D.N. Batchelder, *Raman spectroscopy for a micrometric and tensorial analysis of stress in silicon.* Applied Physics Letters, 2002. **81**(18): p. 3377-3379.

41. Wermelinger, T. and R. Spolenak, *Stress analysis by means of Raman microscopy*, 2010. p. 259-278.

42. Srikar, V.T., et al., *Micro-Raman measurements of bending stresses in micromachined silicon flexures.* Journal of Microelectromechanical Systems, 2003. **12**(Compendex): p. 779-787.

43. Härtelt, M., H. Riesch-Oppermann, and O. Kraft, *Statistical analysis and predictions of fracture and fatigue of micro-components.* Microsystem Technologies, 2011: p. 1-11.

44. Inglis, C.E., *Stresses in a Plate due to the Presence of Cracks and Sharp Corners".* Transactions of the Royal Institution of Naval Architects, 1913. **55**: p. 219.

45. Irwin, G.R., *Fracture.* Handbuch der Physik, 1958. **6**: p. 551-590.

46. Bagdahn, J. and W.N. Sharpe Jr, *Fatigue of polycrystalline silicon under long-term cyclic loading.* Sensors and Actuators, A: Physical, 2003. **103**(1-2): p. 9-15.

47. Suwito, W., M.L. Dunn, and S.J. Cunningham, *Fracture initiation at sharp notches in single crystal silicon.* Journal of Applied Physics, 1998. **83**(7): p. 3574-3582.

48. Suwito, W., et al., *Elastic moduli, strength, and fracture initiation at sharp notches in etched single crystal silicon microstructures.* Journal of Applied Physics, 1999. **85**(7): p. 3519-3534.

49. Sharpe Jr, W.N., et al., *Fracture strength of silicon carbide microspecimens.* Journal of Microelectromechanical Systems, 2005. **14**(5): p. 903-913.

50. Espinosa, H.D., *Elasticity, strength, and toughness of single crystal silicon carbide, ultrananocrystalline diamond, and hydrogen-free tetrahedral amorphous carbon.* Appl. Phys. Lett., 2006. **89**(7): p. 073111.

51. Bagdahn, J., W.N. Sharpe Jr, and O. Jadaan, *Fracture strength of polysilicon at stress concentrations.* Journal of Microelectromechanical Systems, 2003. **12**(3): p. 302-312.

52. Boroch, R., et al., *Characterization of strength properties of thin polycrystalline silicon films for MEMS applications.* Fatigue and Fracture of Engineering Materials and Structures, 2007. **30**(1): p. 2-12.

53. McCarty, A. and I. Chasiotis, *Description of brittle failure of non-uniform MEMS geometries.* Thin Solid Films, 2007. **515**(6): p. 3267-3276.

54. Elata, D. and A. Hirshberg, *A novel method for measuring the strength of microbeams.* Journal of Microelectromechanical Systems, 2006. **15**(2): p. 396-405.

55. Nemeth, N.N., *CARES/LIFE Ceramics Analysis and Reliability Evaluation of Structures Life Prediction Program*. 2003, Cleveland, Ohio : Hanover, MD: National Aeronautics and Space Administration, Glenn Research Center.

56. Pierce, D.M., et al., *Predicting the Failure Probability of Device Features in MEMS.* Device and Materials Reliability, IEEE Transactions on, 2011. **11**(3): p. 433-441.

57. Kittl, P. and G. Diaz, *Weibull's Fracture Statistics, or Probabilistic Strength of Materials: State of the Art.* Res mechanica, 1988. **24**(2): p. 99-207.

58. Cassenti, B.N., *Probabilistic static failure of composite material.* AIAA journal, 1984. **22**(1): p. 103-110.

59. Burdess, J.S., et al., *A system for the dynamic characterization of microstructures.* Microelectromechanical Systems, Journal of, 1997. **6**(4): p. 322-328.

60. Burns, D.J. and H.F. Helbig, *A system for automatic electrical and optical characterization of microelectromechanical devices.* Microelectromechanical Systems, Journal of, 1999. **8**(4): p. 473-482.

61. Aswendt, P., et al., *ESPI solution for non-contacting MEMS-on-wafer testing.* Optics and Lasers in Engineering, 2003. **40**(5-6): p. 501 - 515.

62. Hart, M.R., et al., *Stroboscopic interferometer system for dynamic MEMS characterization.* Microelectromechanical Systems, Journal of, 2000. **9**(4): p. 409-418.

63. Merlijn van Spengen, W., et al., *Characterization and failure analysis of MEMS: high resolution optical investigation of small out-of-plane movements and fast vibrations.* Microsystem Technologies, 2004. **10**(2): p. 89--96.

64. Hedley, J., et al. *Mode shape and failure analysis of high frequency MEMS/NEMS using Raman spectroscopy*. in *3rd IEEE International Conference on Nano/Micro Engineered and Molecular Systems, NEMS*. 2008.

65. Anastassakis, E., et al., *Effect of static uniaxial stress on the Raman spectrum of silicon.* Solid State Communications, 1993. **88**(11-12): p. 1053-1058.

66. Bowden, M. and D.J. Gardiner, *Stress and structural images of microindented silicon by Raman microscopy.* Applied Spectroscopy, 1997. **51**(9): p. 1405--1409.

67. Bowden, M., et al., *Raman and finite-element analysis of a mechanically strained silicon microstructure.* Journal of Micromechanics and Microengineering, 2001. **11**(1): p. 7-12.

68. Lourenço, M.A., et al., *Stress analysis of B doped silicon bridges and cantilever structures by Raman spectroscopy.* Journal of Materials Science Letters, 2000. **19**(9): p. 767-769.

69. Srikar, V.T., et al., *Micro-Raman measurement of bending stresses in micromachined silicon flexures.* Microelectromechanical Systems, Journal of, 2003. **12**(6): p. 779-787.

70. Wolf, I.D., *Micro-Raman spectroscopy to study local mechanical stress in silicon integrated circuits.* Semiconductor Science and Technology, 1996. **11**(2): p. 139-154.

71. Webster, S., D.N. Batchelder, and D.A. Smith, *Submicron resolution measurement of stress in silicon by near-field Raman spectroscopy.* Applied Physics Letters, 1998. **72**(12): p. 1478-1480.

72. Hu, Z.X., et al., *Dynamic characterization of MEMS using Raman spectroscopy.* Journal of Micromechanics and Microengineering, 2008. **18**(9): p. 095019-+.

73. Miyatake, T. and G. Pezzotti, *Tensor-resolved stress analysis in silicon MEMS device by polarized Raman spectroscopy.* Physica Status Solidi (A) Applications and Materials, 2011. **208**(5): p. 1151-1158.

74. Bonera, E., M. Fanciulli, and D.N. Batchelder, *Combining high resolution and tensorial analysis in Raman stress measurements of silicon.* Journal of Applied Physics, 2003. **94**(4): p. 2729-2740.

75. Loechelt, G.H., N.G. Cave, and J. Men√©ndez, *Polarized off-axis Raman spectroscopy: A technique for measuring stress tensors in semiconductors.* Journal of Applied Physics, 1999. **86**(11): p. 6164-6180.

76. Ferraro, J.R., *Introductory Raman Spectroscopy*. 2003: Elsevier Science.

77. Ewen, S., *Modern Raman spectroscopy : a practical approach*. 2005, Chichester: John Wiley,. x, 210 p. : ill. ; 24 cm.

78. Ikehara, T. and T. Tsuchiya, *High-cycle fatigue of micromachined single-crystal silicon measured using high-resolution patterned specimens.* Journal of Micromechanics and Microengineering, 2008. **18**(7).

79. Muhlstein, C.L., E.A. Stach, and R.O. Ritchie, *A reaction-layer mechanism for the delayed failure of micron-scale polycrystalline silicon structural films subjected to high-cycle fatigue loading.* Acta Materialia, 2002. **50**(14): p. 3579-3595.

80. Hopcroft, M.A., W.D. Nix, and T.W. Kenny, *What is the Young's modulus of silicon?* Journal of Microelectromechanical Systems, 2010. **19**(2): p. 229-238.

81. Duffy, S.F. and J.M. Manderscheid, *Noninteractive macroscopic reliability model for ceramic matrix composites with orthotropic material symmetry.* 1989.

82. ASTM-C1239-07, *Standard Practice for Reporting Uniaxial Strength Data and Estimating Weibull Distribution Parameters for Advanced Ceramics*, 2007, ASTM Int.: West Conshohocken, PA.

83. Boresi, A.P. and R.J. Schmidt, *Advanced Mechanics of Materials (6th Edition)*, John Wiley & Sons.

84. Weisstein and E. W., *Principal Radius of Curvature.* MathWorld.

85. Rao, S.S., *Mechanical Vibrations*. 2011: Englewood Cliffs, NJ:Prentice Hall PTR.

86. Pilkey, W.D., *Formulas for Stress, Strain, and Structural Matrices (2nd Edition)*, John Wiley & Sons.

87. Senturia, S.D., *Microsystem Design*. 2013: Springer US.

88. Anastassakis, E., *Selection rules of Raman scattering by optical phonons in strained cubic crystals.* Journal of Applied Physics, 1997. **82**(4): p. 1582-1591.

89. De Wolf, I., H.E. Maes, and S.K. Jones, *Stress measurements in silicon devices through Raman spectroscopy: Bridging the gap between theory and experiment.* Journal of Applied Physics, 1996. **79**(9): p. 7148-7156.

90. Miyatake, T., A.A. Porporati, and G. Pezzotti, *Spatially and tensor-resolved Raman analysis for the determination of phonon deformation potentials on the microscopic scale in Si single-crystal.* Journal of Applied Physics, 2009. **105**(11): p. 113514-8.

91. Chandrasekhar, M., J.B. Renucci, and M. Cardona, *Effects of interband excitations on Raman phonons in heavily doped n-Si.* Physical Review B, 1978. **17**(4): p. 1623-1633.

92. Anastassakis, E., A. Cantarero, and M. Cardona, *Piezo-Raman measurements and anharmonic parameters in silicon and diamond.* Physical Review B, 1990. **41**(11): p. 7529-7535.

93. Nye, J.F., *Physical Properties of Crystals*. 1985, Oxford, UK: Clarendon.

94. De Wolf, I., *Raman spectroscopy: About chips and stress.* Spectroscopy Europe, 2003. **15**(2).

Appendix A – Miller indices

Miller indices are commonly use to describe the faces and direction of crystalline materials.

- A plane intersects x, y and z-coordinates at a, b and c.
- A point on the plane located at $P(x, y, z)$
- The equation defines the $P(x, y, z)$ is:

$$\frac{x}{a} + \frac{y}{b} + \frac{z}{c} = 1$$

or in different form:

$$hx + ky + mz = 1$$

in which: $h = {}^{1}/_{a}$, $k = {}^{1}/_{b}$, and $m = {}^{1}/_{c}$

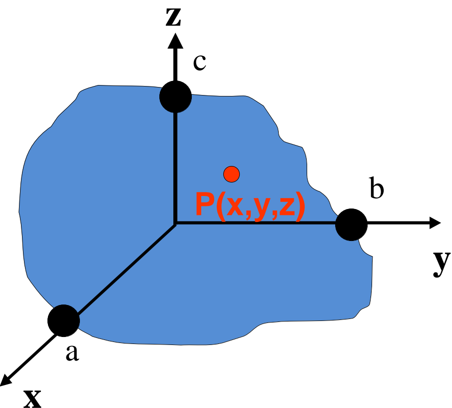

- Miller indices involve:
  - (hkm) = designation of a face or a plane
  - $< hkm >$ = designation of a direction that is perpendicular to the (hkm) plane
- Note: in cubic crystal, such as silicon, $a = b = c = 1$.

Appendix B – adjusted Anderson-Darling statistic

In Minitab® the adjusted Anderson-Darling statistic named as Anderson-Darling (adj) or AD*. The following information is taken from Minitab knowledge base ID 998: http://www.minitab.com/support/answers/answer.aspx?ID=998.

Minitab calculates an adjusted Anderson-Darling statistic for the Distribution ID Plot and for Reliability/Survival analyses. These adjusted Anderson-Darling statistics are equivalent and are represented in the output as Anderson-Darling (adj) or AD*, respectively.

Minitab uses the adjusted statistic because p-values for the Anderson-Darling statistic could not be calculated for multiply censored or arbitrarily censored data. Unlike the standard Anderson-Darling statistic, the adjusted statistic is generalized to account for different plot-point methods the user can choose for constructing the probability plot.

For right-censored or uncensored data, Minitab calculates the plot points using:

- Median rank method (default)
- Modified Kaplan-Meier method
- Herd-Johnson method
- Kaplan-Meier method

If tied failure times (identical failure times) appear in the data, Minitab plots either all points (default), the average (median), or the maximum of the tied points. If the tie involves failures and suspensions, the failures are considered to occur before the suspensions.

Calculating Anderson-Darling adjusted

Using the plot points and the probability integral transformation described in D'Agostino and Stephens (1986), Minitab calculates the adjusted Anderson-Darling as:

$$AD^* = n \cdot \sum_{i=1}^{n+1} A_i + B_i + C_1$$

and:

$$A_i = -Z_i - \ln(1 - Z_i) + Z_{i-1} + \ln(1 - Z_{i-1})$$

$$B_i = 2\ln(1 - Z_i)F_n(Z_{i-1}) - 2\ln(1 - Z_{i-1})F_n(Z_{i-1})$$

$$C_i = \ln(Z_i)F_n(Z_{i-1})^2 - \ln(1 - Z_i)F_n(Z_{i-1})^2 - \ln(Z_{i-1})F_n(Z_{i-1})^2 - \ln(1 - Z_i)F_n(Z_{i-1})^2$$

where:

Z_i is the fitted estimate of the cumulative distribution function (CDF) for the ith plot point

$F_n(Z_i)$ is the nonparametric estimate of the CDF for the ith plot point

$Z_0 = 0$

$F_n(Z_0) = 0$

$Z_{n+1} = 1 - (1E - 12)$

Interpreting Anderson-Darling adjusted

The adjusted Anderson-Darling statistic provides a relative measure of goodness-of-fit. When comparing the goodness-of-fit of multiple distributions for a given data set, the distribution with the smallest adjusted Anderson-Darling statistic offers the best fit. This comparative technique is valid only when comparing the fit of multiple distributions for a single data set, however.

Note: The Anderson Darling statistic generated from **Graph** > **Probability Plot or Stat** > **Quality Tools** > **Individual Distribution Identification** does not have "(adj)" or "*" after it and is not adjusted.

References

R.B. D'Agostino and M.A. Stephens (1986). Goodness-of-Fit Techniques. Marcel Dekker, Inc.

B.W. Turnbull (1976). "The Empirical Distribution Function with Arbitrarily Grouped, Censored and Truncated Data," Journal of the Royal Statistical Society, 38, 290-295.